

Alma Mater Studiorum – Università di Bologna

DOTTORATO DI RICERCA IN

CHIMICA

Ciclo XXIX

Settore Concorsuale di afferenza: CHIM/02

Settore Scientifico disciplinare: CHIMICA FISICA - 03/A2

**NUMERICAL MODELING OF NOVEL CO-REACTANT
ELECTROGENERATED CHEMILUMINESCENCE
SYSTEMS FOR ANALYTICAL APPLICATIONS**

Presentata da: Kenta Imai

Coordinatore Dottorato

Prof. Aldo Roda

Relatore

Prof. Francesco Paolucci

Esame finale anno 2017

Abstract

This thesis focuses on the numerical modeling of co-reactant electrogenerated chemiluminescence (ECL) systems that have been recently proposed for analytical applications.

Co-reactant ECL is light emission triggered by an electrochemical reaction of a luminophore with a co-reactant. Many researchers are trying to expand its application in the analytical field with carrying out various experiments. However, recent reports on the co-reactant ECL have revealed several phenomena that are not yet fully understood from theoretical viewpoint. Better understanding of the reaction mechanism for ECL generation is necessary for further improvement of the co-reactant ECL.

In this context, three kinds of recently-proposed co-reactant ECL systems were numerically modeled in this study to analyze the reaction mechanism. The numerical modeling in this study mainly deals with dynamic ECL behavior while the potential of a working electrode changes with time. The modeling of this kind of dynamic ECL behavior provides us more information than that of static ECL behavior because very precise analysis can be carried out by the consideration of dynamic changes in the modeling parameters.

In Part A of this thesis, a homogeneous ECL system based on solution containing Ir(ppy)₃ and tripropylamine (TPA), which shows interesting ECL quenching at high potential, was firstly analyzed. The numerical modeling in this study verified a mechanism that the excited state of Ir(ppy)₃ is quenched by its reaction with TPA radical cation, which

is generated by the electrochemical oxidation of TPA. Moreover, a multicolor ECL system with the addition of another metal chelate was also modeled in this part, and then a 3D emission map on ECL intensity versus emission wavelength and applied potential was successfully reproduced.

In Part B, heterogeneous ECL from a $\text{Ru}(\text{bpy})_3^{2+}$ -doped silica nanoparticle under solution containing TPA, which was reported as a very efficient ECL system, was analyzed. The numerical modeling in this study proposed that the surface state of the used working electrode changes during potential application, and then that causes the significant reduction of ECL intensity at high potential. Also, the numerical modeling verified a mechanism that the electron hopping inside the nanoparticle contributes to the efficient ECL observed in this system.

In Part C, a new ECL system based on bipolar electrochemistry was modeled. The numerical modeling in this study successfully simulated the ECL behavior for this new ECL system, and then verified a mechanism that ECL quenches in specific area due to the change in local pH during potential application. Moreover, a spatially-resolved bipolar ECL system, which was reported very recently, was also modeled in this part. The experimental results were well reproduced utilizing the findings from other parts of this thesis.

In conclusion, the numerical modeling in this study contributed to the better understanding of the reaction mechanism for ECL generation, which can support further improvement of co-reactant ECL systems. Analysis for the reaction mechanism from theoretical viewpoint should be adequately considered in future experimental studies.

Contents

1. Introduction.....	6
1.1. Electrogenated Chemiluminescence (ECL).....	6
a) Annihilation and co-reactant ECL	6
b) Co-reactant ECL based on Ru(bpy) ₃ ²⁺ and TPA	8
c) Variation of luminophores and co-reactants	11
1.2. Analytical Applications of Co-Reactant ECL.....	15
a) Immunoassays.....	15
b) Nucleic acid analysis.....	17
1.3. Numerical Modeling of Co-Reactant ECL	19
1.4. Aim of This Thesis.....	20
2. Materials and Methods.....	21
2.1. Numerical Modeling	21
2.2. Electrochemical and ECL Measurements	24
3. Part A: Numerical Modeling of Homogeneous and Multicolor ECL.....	25
3.1. Background	25
3.2. Modeling Conditions	30
3.3. Results and Discussion	34
a) Modeling of ECL from Ir(ppy) ₃ /TPA homogeneous system	34
b) Modeling of multicolor ECL from solution containing Ir(ppy) ₃ , Ir(df-ppy) ₃ and TPA	38
4. Part B: Numerical Modeling of Heterogeneous ECL from a Luminophore-Doped Nanoparticle	43
4.1. Background	43
4.2. Modeling and Measuring Conditions.....	44
a) Modeling conditions	44
b) Experimental conditions	48
4.3. Results and Discussion	49

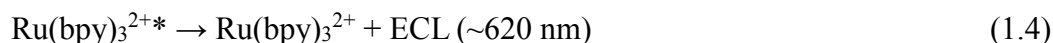
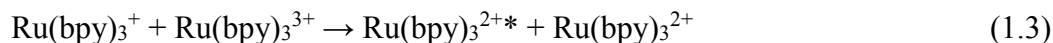
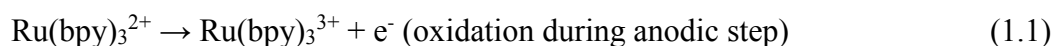
a)	Experimental results.....	49
b)	Step 1: Modeling of reactions triggered by TPA oxidation for the first ECL wave	52
c)	Step 2: Modeling of reactions triggered by TPA and Ru (bpy) ₃ ²⁺ oxidation for the second ECL wave.....	61
d)	Consideration of electrical current derived from oxygen evolving reaction during potential application	66
5.	Part C: Numerical Modeling of ECL Induced by Bipolar Electrochemistry	68
5.1.	Background.....	68
5.2.	Modeling Conditions	73
5.3.	Results and Discussion	75
5.4.	Modeling of Spatially-Resolved Multicolor Bipolar ECL.....	81
6.	Conclusions.....	92
7.	List of Publication.....	94
8.	Supplemental Information: Models and Parameters	95
8.1.	Part A	95
8.2.	Part B	101
8.3.	Part C (1D).....	109
8.4.	Part C (2D).....	115
8.5.	Part C (Spatially-resolved bipolar ECL, 2D).....	122
9.	References.....	129
10.	Acknowledgment.....	142

1. Introduction

1.1. Electrogenenerated Chemiluminescence (ECL)

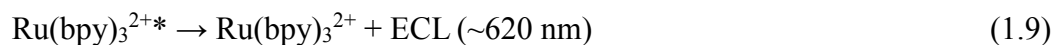
a) Annihilation and co-reactant ECL

Electrogenenerated chemiluminescence (ECL) is defined as the light emission occurring at electrodes caused by energetic electron transfer reactions of electrogenerated species in solution [1]. The first experiments on ECL in the world were carried out in 1964-1965 [2]–[4]. For example, Hercules reported light emission from non-aqueous solution containing a number of hydrocarbons under potential application to a platinum electrode [2]. In the 2nd half of 1960s, analytical and theoretical studies to clarify the reaction mechanism for ECL generation were also started [5]–[10]. In 1972, Tokel and Bard reported annihilation ECL from a metal chelate, tris(2,2'-bipyridine)ruthenium(II) ($\text{Ru}(\text{bpy})_3^{2+}$, bpy = 2,2'-bipyridine), whose photoluminescence and chemiluminescence were already known in aprotic solvents [11]. The reaction sequence of this annihilation ECL was suggested as follows:



Scheme 1.1 - Reaction sequence of annihilation ECL from $\text{Ru}(\text{bpy})_3^{2+}$. The symbol “*” means excited state in this thesis.

The report of the ECL from water-soluble $\text{Ru}(\text{bpy})_3^{2+}$ suggested there is possibility of ECL emission in aqueous solution, which gives advantages for the application of ECL into analytical methods. However, it was difficult to reduce $\text{Ru}(\text{bpy})_3^{2+}$ in aqueous solution ($\text{Ru}(\text{bpy})_3^{2+} + \text{e}^- \rightarrow \text{Ru}(\text{bpy})_3^+$, $E^0 \approx -1.5 \text{ V vs. Ag|AgCl}$) because the potential window of water is smaller than that of an aprotic solvent. And so, species that could generate a reducing agent for reaction with $\text{Ru}(\text{bpy})_3^{3+}$ during the oxidation process, what are called co-reactants, were searched for. Chang and Saji in Bard's group reported oxalate anion as a co-reactant for $\text{Ru}(\text{bpy})_3^{2+}$ in 1977 [12], and then, Noffsinger and Danielson discovered tripropylamine (TPA), which exhibits much higher ECL efficiency, in 1987 [13]. The reaction sequence of the co-reactant ECL based on the oxalate anion and $\text{Ru}(\text{bpy})_3^{2+}$ is shown in Scheme 1.2. The highly reducing agent ($\text{CO}_2^{\bullet-}$, $E^0 \approx -2.3 \text{ V vs. Ag|AgCl}$ [14]) is generated by the electrochemical oxidation and subsequent chemical decomposition, and then it reacts with $\text{Ru}(\text{bpy})_3^{3+}$ to generate the excited state of $\text{Ru}(\text{bpy})_3^{2+}$. This kind of reaction is called "oxidative-reduction".



Scheme 1.2 - Reaction sequence of co-reactant ECL based on $\text{Ru}(\text{bpy})_3^{2+}$ and $\text{C}_2\text{O}_4^{2-}$.

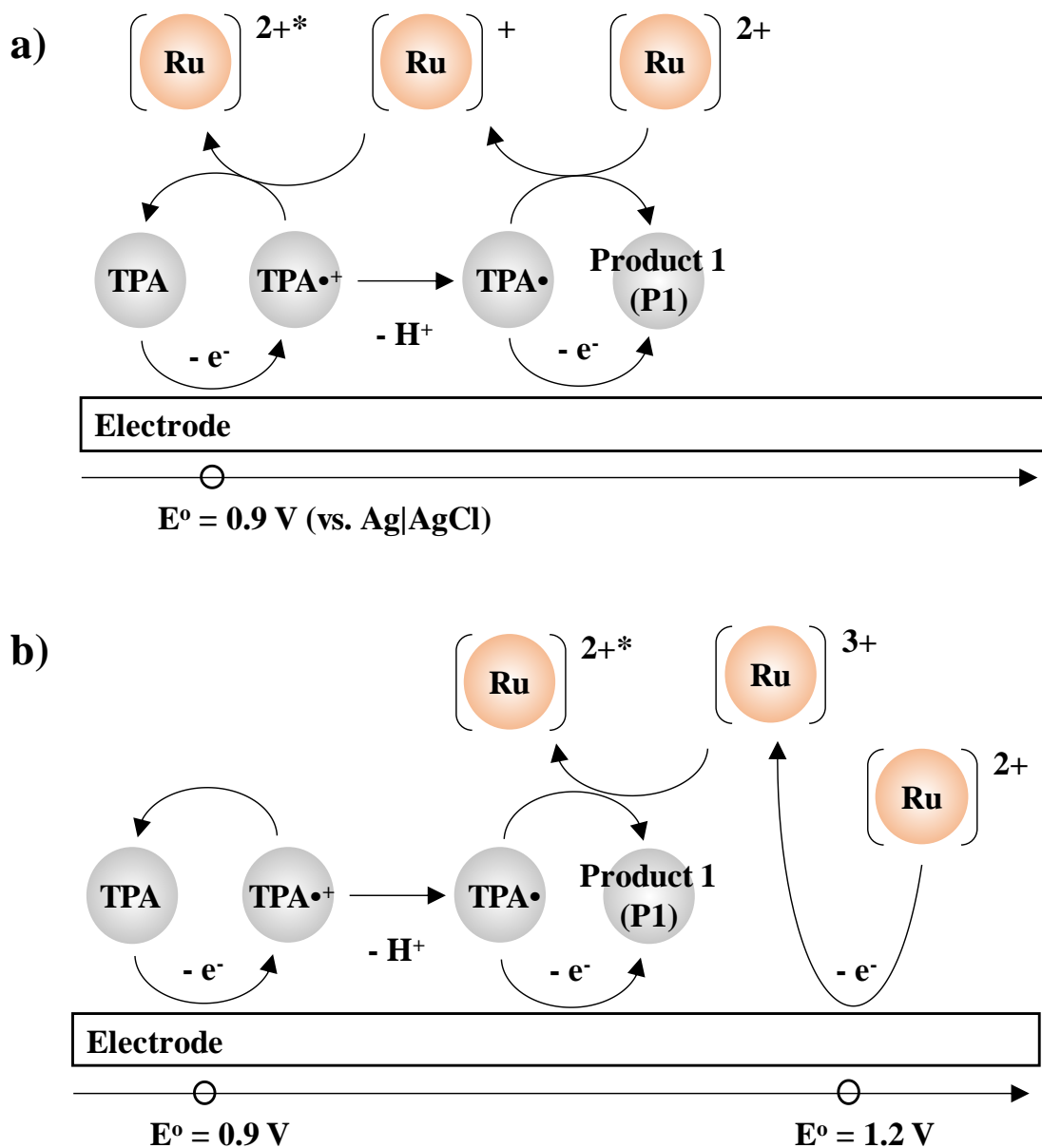
b) Co-reactant ECL based on $\text{Ru}(\text{bpy})_3^{2+}$ and TPA

Since the discovery of TPA as a very efficient co-reactant [13], Many studies based on the $\text{Ru}(\text{bpy})_3^{2+}/\text{TPA}$ ECL system have been reported [15]–[23]. In parallel with studies aiming for more efficient ECL, analysis for the reaction mechanism for ECL generation has been also investigated by several researchers because the ECL mechanism for the $\text{Ru}(\text{bpy})_3^{2+}/\text{TPA}$ system was found to be very complicated [24]–[31].

In 2002, Miao and Choi in Bard's group proposed a new ECL mechanism involving TPA radical cation ($\text{TPA}^{\bullet+}$) and TPA radical (TPA^\bullet) [32]. It was well known that ECL intensity from the $\text{Ru}(\text{bpy})_3^{2+}/\text{TPA}$ system shows two waves when potential is scanned in positive direction. The first ECL wave appears at ~ 0.9 V (vs. $\text{Ag}|\text{AgCl}$), where $\text{Ru}(\text{bpy})_3^{2+}$ is not yet oxidized ($E^\circ \approx 1.2$ V). This kind of ECL wave was not observed in the $\text{Ru}(\text{bpy})_3^{2+}/\text{C}_2\text{O}_4$ system stated above. They suggested a reaction pathway that both of $\text{TPA}^{\bullet+}$ and TPA^\bullet play important roles as shown in Scheme 1.3 a). First, TPA starts to be oxidized at ~ 0.9 V at the working electrode to produce $\text{TPA}^{\bullet+}$, and then $\text{TPA}^{\bullet+}$ loses a proton to generate TPA^\bullet . Here, $\text{TPA}^{\bullet+}$ is a relatively-stable radical having a half-life of ~ 0.2 ms [32] and it can act as an oxidizing agent ($E^\circ \approx 0.9$ V) during its lifetime. On the other hand, TPA^\bullet generated by $\text{TPA}^{\bullet+}$ decomposition is a strong reducing agent ($E^\circ \approx -1.7$ V) and it can react with $\text{Ru}(\text{bpy})_3^{2+}$ to form $\text{Ru}(\text{bpy})_3^+$. Finally, $\text{TPA}^{\bullet+}$ reacts with $\text{Ru}(\text{bpy})_3^+$ to generate the excited state $\text{Ru}(\text{bpy})_3^{2+}$ ($\text{Ru}(\text{bpy})_3^{2+*}$). The existence of $\text{TPA}^{\bullet+}$ was evidenced in ESR experiments in their report. In this reaction pathway, the lifetime of $\text{TPA}^{\bullet+}$ is critical for the intensity of ECL because $\text{TPA}^{\bullet+}$ and TPA^\bullet are both necessary to generate the excited state. In other words, the ECL intensity is governed by the

deprotonation equilibrium of $\text{TPA}\cdot^+$. The difference of this equilibrium at different distance from the electrode surface results in non-homogenous intensity of ECL.

The second ECL wave appears at ~ 1.2 V, which corresponds to the oxidation potential of $\text{Ru}(\text{bpy})_3^{2+}$. The second ECL wave follows the “classical” co-reactant ECL mechanism as shown for the $\text{Ru}(\text{bpy})_3^{2+}/\text{C}_2\text{O}_4$ system. The ECL mechanism for the second ECL wave is illustrated in Scheme 1.3 b). In this pathway, both of TPA and $\text{Ru}(\text{bpy})_3^{2+}$ are oxidized simultaneously on the working electrode. And then, the generated $\text{TPA}\cdot$ and $\text{Ru}(\text{bpy})_3^{3+}$ react to form $\text{Ru}(\text{bpy})_3^{2+*}$. $\text{Ru}(\text{bpy})_3^{3+}$ can also react with $\text{Ru}(\text{bpy})_3^+$, which is formed by the reaction of $\text{TPA}\cdot$ and $\text{Ru}(\text{bpy})_3^{2+}$, to generate the excited state as shown for the annihilation ECL (not described in the scheme).



Scheme 1.3 - Reaction sequence of co-reactant ECL based on $\text{Ru}(\text{bpy})_3^{2+}$ and TPA ($\text{TPA}\cdot^+$ = $(\text{CH}_3\text{CH}_2\text{CH}_2)_3\text{N}\cdot^+$; $\text{TPA}\cdot$ = $(\text{CH}_3\text{CH}_2\text{CH}_2)_2\text{NC}\cdot\text{HCH}_2\text{CH}_3$; product 1 (P1) = $(\text{CH}_3\text{CH}_2\text{CH}_2)_2\text{N}^+\text{CHCH}_2\text{CH}_3$).

c) Variation of luminophores and co-reactants

Various kinds of luminophores and co-reactants for ECL generation have been investigated until today, for the discovery of more efficient ECL systems and new applications.

i. Luminophores

There has been a great interest in metal chelate luminophores because numerous metal chelates are also known as photoluminescent and chemiluminescent materials, and the tuning of the wavelength of the emission, which could expand the application of ECL, is comparatively easy by the selection of metal and chelate materials. Numerous studies on metal chelates based on transition metals, main group metals and rare earth metals have been carried out until today. Since the first metal chelate ECL was reported based on $\text{Ru}(\text{bpy})_3^{2+}$, many researches on $\text{Ru}(\text{bpy})_3^{2+}$ -related complexes can be easily found. Table 1.1 summarizes the ECL properties of Ru-polypyridine complexes obtained with TPA as the co-reactant [20], [33]–[39].

Table 1.1 - ECL properties of Ru-polypyridine complexes obtained with TPA. ECL efficiencies were calculated by comparing the ECL intensities with $\text{Ru}(\text{bpy})_3^{2+}/\text{TPA}$.

Metal chelates/Co-reactant	Solvent	λ [nm]	ECL efficiency
$\text{Ru}(\text{bpy})_3^{2+}/\text{TPA}$	H_2O (0.2 M KH_2PO_4)	610	1 (ref.)
$(\text{bpy})_2\text{Ru}(\text{AZA-bpy})^{2+}/\text{TPA}$	H_2O (0.2 M KH_2PO_4)	613	0.51
$(\text{bpy})_2\text{Ru}(\text{CE-bpy})^{2+}/\text{TPA}$	H_2O (0.1 M Tris)	650	1.0

$(\text{bpy})_2\text{Ru}(\text{bphb})^{2+}/\text{TPA}$	MeCN (0.1 M TBAPF ₆)	624	1.5
$[(\text{bpy})_2\text{Ru}]_2(\text{bphb})^{4+}/\text{TPA}$	MeCN	624	2.6

On the other hand, ECL based on iridium (III) complexes has been also widely investigated by many researchers [40]–[53]. The reaction sequence of co-reactant ECL based on Ir(ppy)₃ (ppy = 2-phenylpyridinato) and TPA is shown in Scheme 1.4. Since TPA• cannot easily reduce Ir(ppy)₃ ($E^\circ \approx -2.4$ V vs. Ag|AgCl), ECL from the Ir(ppy)₃/TPA system is generated basically via the classical reaction pathway. In the Ir(ppy)₃/TPA system, the reaction of Ir(ppy)₃* with TPA•⁺ that quenches ECL needs to be considered [54], [55]. The influence of this reaction is discussed in a later section of this thesis.



Scheme 1.4 - Reaction sequence of co-reactant ECL based on Ir(ppy)₃ and TPA. (P1 and P2: TPA derivatives).

Ir-based ECL in aqueous solution was also investigated using TPA from the viewpoints of fundamental study and applications, similarly to the Ru-based ECL. ECL

from Ir(ppy)₃ is usually observed at ~0.8 V vs. Ag|AgCl, which corresponds to the oxidation potential of Ir(ppy)₃, although the observed ECL efficiency is usually much lower than the Ru(bpy)₃²⁺/TPA system [56]. The wavelength of emitted ECL from Ir(ppy)₃ is lower than that from Ru(bpy)₃²⁺ [56]. The lower potential required for the Ir(ppy)₃ excitation has an advantage in DNA analysis because DNA can be damaged with a potential application of >1.0 V vs. Ag|AgCl. Table 1.2 summarizes the ECL properties of Ir-complexes obtained with TPA as the co-reactant [56]–[59].

Table 1.2 - ECL properties of Ir-complexes obtained with TPA (ECL efficiency values are compared with the Ru(bpy)₃²⁺/TPA aqueous system).

Metal chelates/Co-reactant	Solvent	λ [nm]	ECL efficiency
Ir(ppy) ₃ /TPA	MeCN (0.1 M TBAPF ₆)	517	0.33
Ir(ppy) ₃ /TPA	MeCN:H ₂ O (50:50 v/v)	517	0.0044
Ir(ppy) ₃ /TPA	H ₂ O (0.2 M KH ₂ PO ₄)	517	0.00092

ii. Co-reactants

Since the discovery of oxalate anion as a co-reactant for ECL emission, various kinds of co-reactants have been also reported. Bolletta and co-researchers [60] and White and Bard [61] reported ECL using persulfate as a co-reactant in 1982, and then a lot of studies were carried out based on this system [39], [57], [62]–[67]. However, since the discovery of very efficient ECL using amine-related substances such as TPA, major researches on ECL has been performed using TPA or other amine-related substances. Table 1.3 summarizes the ECL properties of Ru(bpy)₃²⁺ obtained with different co-reactants [15],

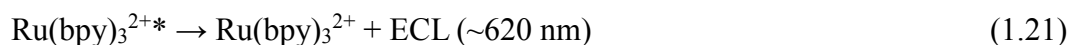
[61], [68]. There are also studies for other amines as co-reactants, and it was recently reported that some amines such as DBEA show better performance than TPA under some specific conditions [69].

Table 1.3 - ECL properties of Ru(bpy)₃²⁺ obtained with different co-reactants.

Metal chelates/Co-reactant	Solvent	λ [nm]	ECL efficiency
Ru(bpy) ₃ ²⁺ /TPA	H ₂ O (0.2 M KH ₂ PO ₄)	610	1 (ref.)
Ru(bpy) ₃ ²⁺ /C ₂ O ₄ ²⁻	H ₂ O (0.1 M H ₂ SO ₄)	610	0.02
Ru(bpy) ₃ ²⁺ /S ₂ O ₈ ²⁻	MeCN:H ₂ O (50:50 v/v)	625	0.025

Since amines are related to a lot of biological substances, there is another approach that a biological substance is used as a co-reactant. An example for this approach is nicotinamide adenine dinucleotide (NADH) [70]–[74]. NADH is generated inside living animals by the reaction of glucose with NAD⁺ under the presence of glucose dehydrogenase. NADH can act as a co-reactant with Ru(bpy)₃²⁺ to generate ECL. Since NAD⁺ cannot act as a co-reactant, this ECL system can be also applied to a bioanalytical system to estimate glucose concentration in an unknown liquid. The reaction sequence of the co-reactant ECL based on Ru(bpy)₃²⁺ and NADH is shown in Scheme 1.5.





Scheme 1.5 - Reaction sequence of co-reactant ECL based on $\text{Ru}(\text{bpy})_3^{2+}$ and NADH.

1.2. Analytical Applications of Co-Reactant ECL

Various luminescence-based techniques have been investigated for analytical applications due to their high signal-to-background ratio. And also, ECL has an advantage in analytical applications compared with photoluminescence and chemiluminescence in that it does not require an external light source [1]. After the aqueous co-reactant ECL systems were discovered in the late 1970s, interest for the application of ECL into analytical systems increased remarkably [15], [75]. Bard and Whitesides first applied for a patent on $\text{Ru}(\text{bpy})_3^{2+}$ - and $\text{Os}(\text{bpy})_3^{2+}$ -based ECL luminophores for bioanalytical systems in 1984 [76]. Since various organic compounds can be chemically connected to these ECL luminophores via their n-hydroxysuccinimide (NHS) ester parts, high-sensitive immunoassays and nucleic acid analysis systems based on ECL became promising. ECL-based immunoassays and DNA analysis, whose concepts are shown in this section, have been reported and used in analytical applications since 1990s [76]–[84].

a) Immunoassays

Clinical immunoassays require very high sensitivity and reliability to realize the accurate and precise determination of the concentrations of antigens or antibodies in unknown liquid-based samples from living animals. For example, immunoassays are used

for the analysis of cancer markers, infectious diseases and hormones, whose concentration ranges are under the order of nanomolar. In typical immunoassays aimed at determining the concentration of an antigen in unknown sample solution, an antibody modified with a luminophore and another antibody chemically connected to a micro/nanoparticle are firstly reacted with the antigen in a reaction container to produce an immune complex of the antigen and two antibodies (see Figure 1.1a). Since the immune complex looks like the antigen is sandwiched by the two antibodies, this immunoassay format is often called “sandwich immunoassay”. And then, the reaction liquid including the immune complex is transferred to the inside of a detection cell. In the case of ECL-based immunoassays, the detection cell comprises working, counter and reference electrodes, and a part to detect light emitted at the working electrode. During the transfer of the reaction liquid, the immune complex is captured on the working electrode surface by chemical bonding (e.g., reaction of thiol on the particle and gold working electrode) or magnetic force (e.g., use of a magnetic particle and a permanent magnet positioned on the backside of the working electrode). After that, solution containing a co-reactant is transferred to the detection cell to replace the reaction liquid while keeping the immune complex on the working electrode. In this period, unreacted antibodies are removed from the detection cell by the liquid flow. After the detection cell is filled with solution containing the co-reactant, an appropriate potential is applied to the working electrode to generate ECL from the luminophore in the immune complex. Finally, the concentration of the antigen in the unknown sample is calculated using the relationship between the concentration of the antigen and the intensity of the generated ECL, which was obtained in advance.

Since this protocol uses a luminophore in the solid phase (microparticle) and a co-reactant in the liquid phase (solution), this kind of protocol is called “heterogeneous ECL”. On the other hand, ECL protocol using solution containing a soluble luminophore and co-reactants is called “homogeneous ECL”. In the heterogeneous ECL as stated here, most of the luminophores in the solid phase are not in an electron-transferrable distance to the working electrode surface, which direct electron transfer can happen between the luminophores and the electrode (the order of 1 nm). And so, the luminophore cannot be directly oxidized at the electrode. Therefore, ECL from the heterogeneous system is mostly governed by the newly proposed reaction pathway triggered only by the oxidation of the co-reactant, which was explained in previous section in this thesis.

b) Nucleic acid analysis

Nucleic acid analysis is another field requiring very high sensitivity and reliability. For example, clinical analysis of HIV virus and confirmation testing for Hepatitis-B virus (HBV) infection are carried out by nucleic acid analysis. Typical protocol used for nucleic acid analysis such as DNA is similar to that for immunoassays. A target single-strand DNA is used instead of an antigen, and two kinds of single-strand DNA probes chemically connected with luminophores and a micro/nanoparticle are used instead of antibodies (see Figure 1.1b).

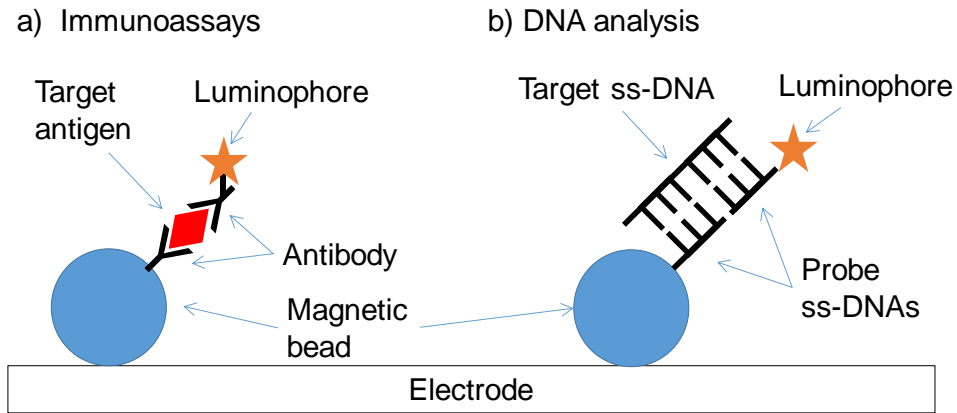


Figure 1.1 – Schematic figure for typical immunoassay and DNA analysis formats. Note that this figure is prepared for the explanation of analytical concept, and so the scale of materials is different from that actually used in analytical applications (e.g., a bead is usually much larger than an antibody/DNA).

1.3. Numerical Modeling of Co-Reactant ECL

As stated above, the reaction mechanism for ECL generation is very complicated to be analyzed in either homogeneous or heterogeneous systems. Numerical modeling has been a powerful tool to analyze the correctness of hypotheses for an unclear mechanism and single out the relevant kinetic and thermodynamic parameters associated to the mechanism. For example, the numerical modeling of an annihilation ECL gave important information on the kinetics of the homogeneous electron transfer [85], [86]. Klymenko and co-researchers investigated ECL from homogeneous solution containing $\text{Ru}(\text{bpy})_3^{2+}$ and TPA using KISSA-1D software [87]. They established a model to analyze ECL behavior during potential scan considering various reactions occurred in the solution. They also studied the effects of diffusion coefficients for a luminophore and a co-reactant on ECL behavior, and showed the diffusion behaviors of the luminophore and the co-reactant significantly affect the ECL behavior [88]. Sentic and co-researchers investigated the mechanism for ECL from a microparticle modified with $\text{Ru}(\text{bpy})_3^{2+}$ using COMSOL Multiphysics® software [89]. Their results indicated that ECL is mainly generated from the bottom part of the bead, and also that the lifetime of $\text{TPrA}\bullet^+$ significantly affects the intensity of ECL.

1.4. Aim of This Thesis

This thesis focuses on the numerical modeling of three kinds of recently-proposed co-reactant ECL systems for analytical applications. Numerical modeling is a powerful tool in analysis for complicated reaction mechanisms. In particular, the numerical modeling in this study mainly deals with dynamic ECL behavior while the potential of a working electrode changes with time. The modeling of this kind of dynamic ECL behavior provides us more information than that for static ECL behavior because very precise analysis can be carried out by the consideration of dynamic changes in the modeling parameters.

In this context, three kinds of newly-proposed co-reactant ECL systems were numerically modeled in this study. In Part A, a homogeneous ECL system based on solution containing Ir(ppy)₃ and tripropylamine (TPA), which shows interesting ECL quenching at high potential, was firstly analyzed. Moreover, a multicolor ECL system with the addition of another metal chelate was also modeled in this part. In Part B, heterogeneous ECL from a Ru(bpy)₃²⁺-doped silica nanoparticle under solution containing TPA, which was reported as a very efficient ECL system, was analyzed. In Part C, a new ECL system based on bipolar electrochemistry was analyzed. Moreover, a spatially-resolved bipolar ECL system, which was reported very recently, was also modeled. Throughout this study, better clarification of the reaction mechanism of ECL generation was aimed for further improvement of the co-reactant ECL systems.

2. Materials and Methods

2.1. Numerical Modeling

COMSOL Multiphysics® software (version 3.5a) was used for the numerical modeling in this study. Chemical Engineering Module with 1D- or 2D-geometry of the software was used to model electrochemical reactions, reactions in bulk solution and the diffusion of the species [90]–[92]. Electrochemical oxidation/reduction reactions were modeled considering electron transfer at boundary between electrode surface and solution as the result of the inflow of the pristine substances to the electrode and the outflow of the reaction products to the solution. The Butler-Volmer equation shown below was used to describe the kinetics of an electron transfer reaction, where i is electrical current, F is the Faraday constant, A is electrode active surface area, k°_h (or k°) is the standard rate constant for heterogeneous electron transfer, α is charge transfer coefficient, c_i is the concentration of oxidized and reduced species, E° is formal potential and E is applied potential. Decomposed equations were also shown below to make the forward and backward reactions clear, where k_f is forward rate constant, k_b is backward rate constant. The influence of reactions occurring at a counter electrode surface was not considered in this study.

$$i = F A k^{\circ} \left\{ \exp^{-\alpha \frac{F}{RT} (E - E^{\circ})} c_O - \exp^{(1-\alpha) \frac{F}{RT} (E - E^{\circ})} c_R \right\} \quad (2.1)$$

$$k_f = k^{\circ} \exp \{-\alpha F (E - E^{\circ})\} \quad (2.2)$$

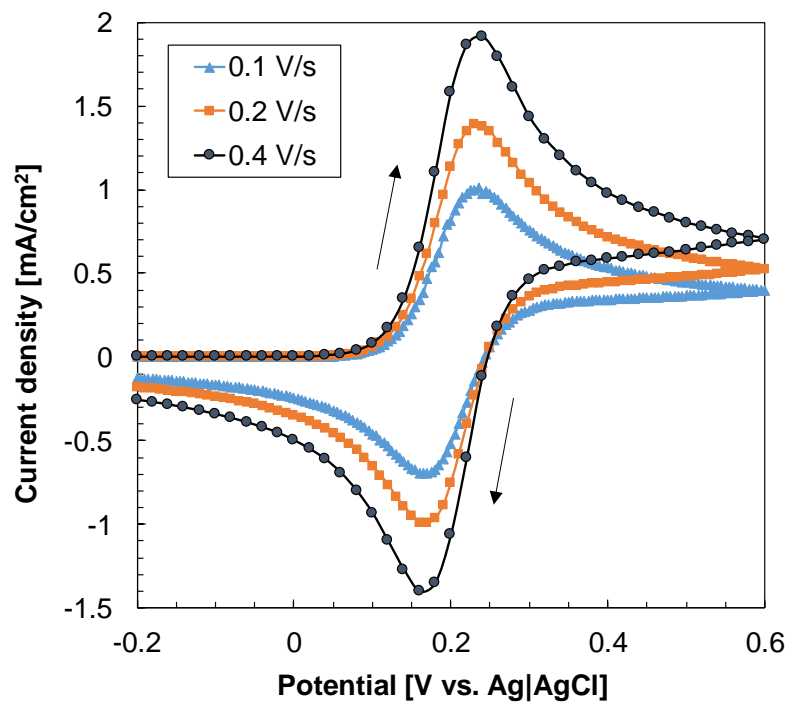
$$k_b = k^{\circ} \exp \{(1 - \alpha) F (E - E^{\circ})\} \quad (2.3)$$

The diffusion of species in the electrochemical cell was modeled using Fick's law of diffusion shown below, where c is concentration and D is diffusion coefficient.

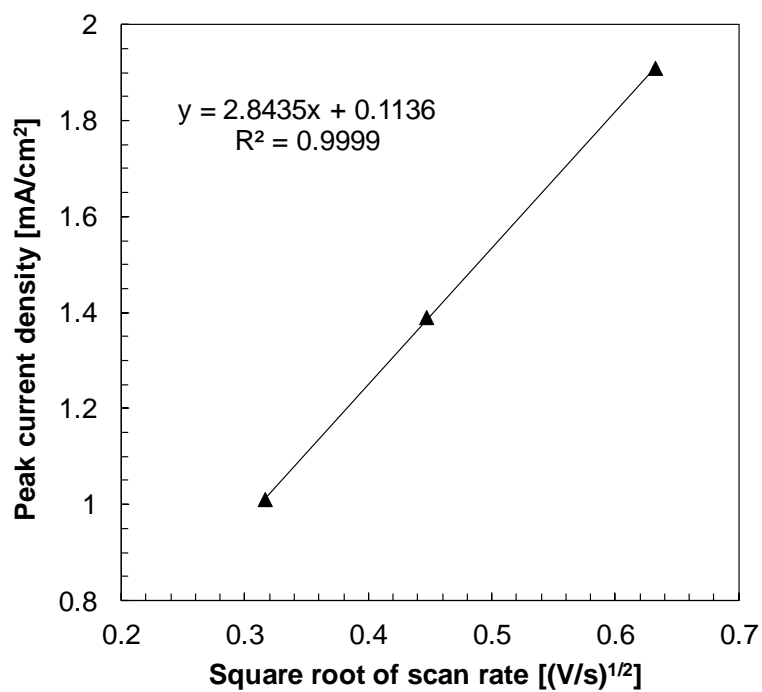
$$\frac{\partial c}{\partial t} = D\nabla^2 c \quad (2.4)$$

A calculation was carried out using UMFPACK linear system solver using appropriate tolerances for each calculation, with allowing the use of complex numbers. The other parameters for the calculation were not modified from the original settings of the software.

Figure 2.1 shows the results for the numerical modeling of cyclic voltammetry of 5 mM $\text{Fe}(\text{CN})_6^{4-}$ with different potential scan rates, which was carried out prior to the numerical modeling of ECL for the verification of the modeling concept. Major parameters used in the numerical modeling are as follows: the dimensions of the electrochemical cell: 1 mm \varnothing x 0.5 mm height; the diameter of the working electrode: 0.5 mm; k^0 : $5.2 \times 10^{-2} \text{ cm s}^{-1}$; D : $5.0 \times 10^{-6} \text{ cm}^2 \text{ s}^{-1}$. As shown in Figure 2.1, expected cyclic voltammograms, which have current peaks at potentials of $\sim 0.17 \text{ V}$ and $\sim 0.23 \text{ V}$ vs. $\text{Ag}|\text{AgCl}$, were obtained in the calculated cyclic voltammograms. Also, the relationship between the peak current value and the square root of scan rate was found to be linear, which is also in line with the experimental results [93].



a) Calculated cyclic voltammograms for $\text{Fe}(\text{CN})_6^{4-}$ with different scan rates.



b) Peak current density as a function of the square root of scan rate.

Figure 2.1 – Calculated cyclic voltammetry of 5 mM $\text{Fe}(\text{CN})_6^{4-}$ with different scan rates.

2.2. Electrochemical and ECL Measurements

Cyclic voltammetry and ECL measurements are carried out using a commercial potentiostat (Bio-Logic SP-300). Gold sputtered on Si substrate was used as a working electrode, and platinum wire was used as a counter electrode. Saturated Ag|AgCl was used as a reference electrode. ECL signal was measured with a photomultiplier tube (PMT, Hamamatsu R4220p) placed a few millimetres from the cell, and in front of the working electrode, inside a dark box. A voltage in the range 250-750 V was supplied to the PMT.

3. Part A: Numerical Modeling of Homogeneous and Multicolor ECL

3.1. Background

ECL from Ir(III) complexes in aprotic solvents have been studied by a number of researchers in parallel with that from Ru(II) complexes, as explained in the introduction part of this thesis [40]–[53]. Some research groups have reported that ECL behavior for the Ir(III) complexes as a function of applied potential, showing that ECL rapidly quenches after having its peak. Zanarini and co-researchers in Paolucci's group previously pointed out the possible effect of the electrode surface fouling at high potential in the case of using Pt electrodes because the potential for the ECL peak is close to the oxygen evolution potential at Pt electrodes [44]. Recently, Doeven and co-researchers in Hogan's group reported similar ECL quenching in Ir(ppy)₃/TPA homogeneous ECL system, but within the potential window of the used glassy carbon electrode [54], [55], [94], [95]. They proposed a new quenching mechanism that TPA^{•+} reacts with Ir(ppy)₃* to produce Ir(ppy)⁺, competing with ECL emission from Ir(ppy)₃*. They pointed out that Ir(ppy)* is a strong reducing agent ($E^0 \approx -2.1$ V vs. Fc, Fc: the redox potential of ferrocene) compared with Ru(bpy)₃^{2+*} ($E^0 \approx -0.9$ V), and so Ir(ppy)* can be significantly quenched by the reaction with TPA^{•+} ($E^0 \approx 0.5$ V) if the concentration of TPA^{•+} is high enough at high potential. They changed TPA concentration in their experiments and showed that the ECL quenching is significant in the case of higher TPA concentration (see Figure 3.1). Someone might notice that they used Ru(bpy)₂(L)²⁺ instead of Ru(bpy)₃²⁺ (L = *N*⁴,*N*^{4'}-bis((2*S*)-1-methoxy-1-oxopropan-2-yl)-2,2'-bipyridyl-4,4'-dicaboxamide);

however, the electrochemical behavior of $\text{Ru}(\text{bpy})_2(\text{L})^{2+}$ is almost the same as that of $\text{Ru}(\text{bpy})_3^{2+}$. $\text{Ru}(\text{bpy})_2(\text{L})^{2+}$ has high emission wavelength (~ 670 nm) compared to $\text{Ru}(\text{bpy})_3^{2+}$. In this part, the $\text{Ir}(\text{ppy})_3/\text{TPA}$ homogeneous-ECL system was numerically modeled to clarify the quenching mechanism from theoretical viewpoint.

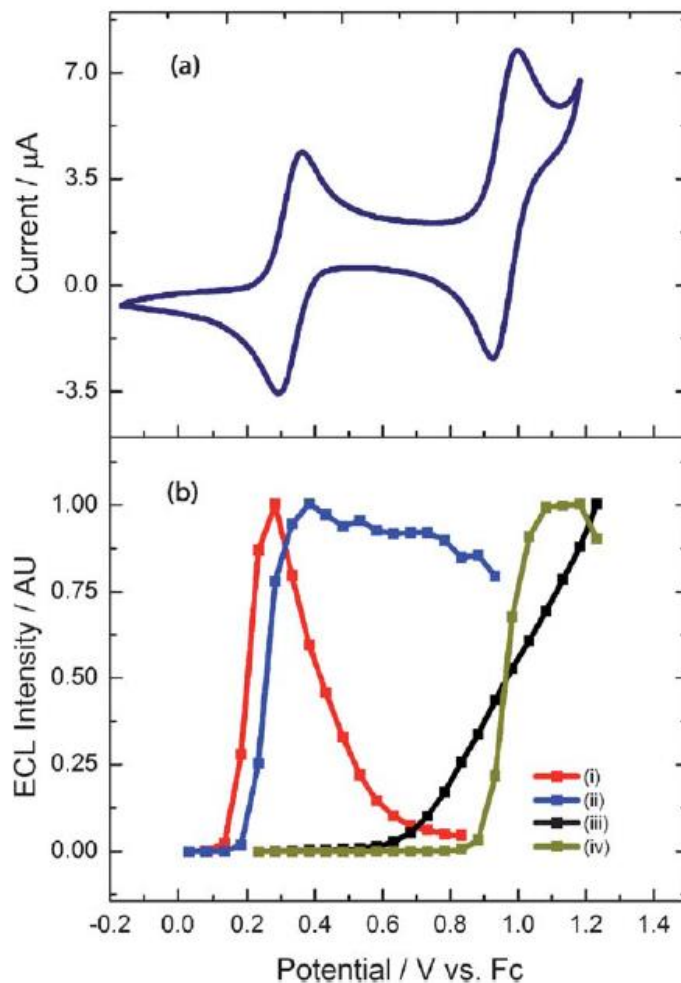


Figure 3.1 - (a) Experimentally-obtained cyclic voltammogram for a mixture of 0.25 mM $\text{Ir}(\text{ppy})_3$ and 0.25 mM $[\text{Ru}(\text{bpy})_2(\text{L})]^{2+}$. (b) Integrated ECL intensity (normalized) from separate solutions of $\text{Ir}(\text{ppy})_3$ and $[\text{Ru}(\text{bpy})_2(\text{L})]^{2+}$ at two TPA concentrations: (i) 0.25 mM $\text{Ir}(\text{ppy})_3$ with 20 mM TPA; (ii) 0.25 mM $\text{Ir}(\text{ppy})_3$ with 0.25 mM TPA; (iii) 0.025 mM

[Ru(bpy)₂(L)]²⁺ and 20 mM TPA; (iv) 0.025 mM [Ru(bpy)₂(L)]²⁺ and 0.25 mM TPA (L = *N*⁴,*N*^{4'}-bis((2*S*)-1-methoxy-1-oxopropan-2-yl)-2,2'-bipyridyl-4,4'-dicaboxamide). All measurements were carried out using a glassy carbon electrode. Reprinted from [54] with permission from The Royal Society of Chemistry.

Moreover, the numerical modeling of “multicolor” ECL with the combination of Ir(ppy)₃ and Ir(df-ppy)₃ (df-ppy = 2-(2,4-difluorophenyl)pyridinato) was also carried out in this part. A multicolor ECL system whose color can be tunable in principle allows multiplex ECL analysis, which is advantageous in bioanalytical applications such as immunoassays and DNA analysis [54]. In the case of the Ir(ppy)₃/TPA system, since ECL quenches at high potentials, the combination of Ir(ppy)₃ and another luminophore having a higher oxidation potential and different emission wavelength profile can realize a multicolor ECL system whose emission wavelength profile can be tunable by the applied potential. For example, the combination of Ir(ppy)₃ and Ir(df-ppy)₃ can realize a multicolor ECL system whose emission can be selectable from green and blue (see Table 3.1).

Table 3.1 – Relationship between applied potential and ECL wavelength (and color) in the multicolor ECL system containing Ir(ppy)₃, Ir(df-ppy)₃ and TPA [54].

Applied potential	Peak ECL wavelength	Observed color
0.2 – 0.7 V vs. Fc	~520 nm	Green
>0.7 V vs. Fc	~495 nm	Blue

Figure 3.2 shows a 3D ECL map that shows ECL intensity versus emission wavelength and applied potential, which was experimentally analyzed. This map shows that the color of ECL depends on the applied potential, which means the ECL color is tunable. Scheme 3.1 shows the chemical structures of Ir(ppy)_3 and Ir(df-ppy)_3 with Ru(bpy)_3^{2+} for reference.

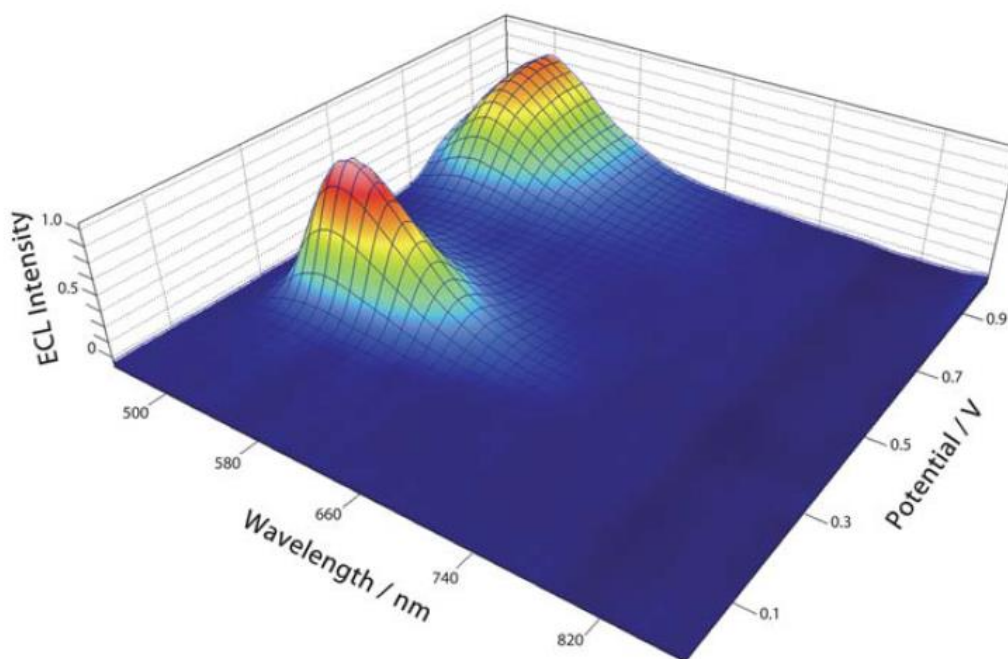
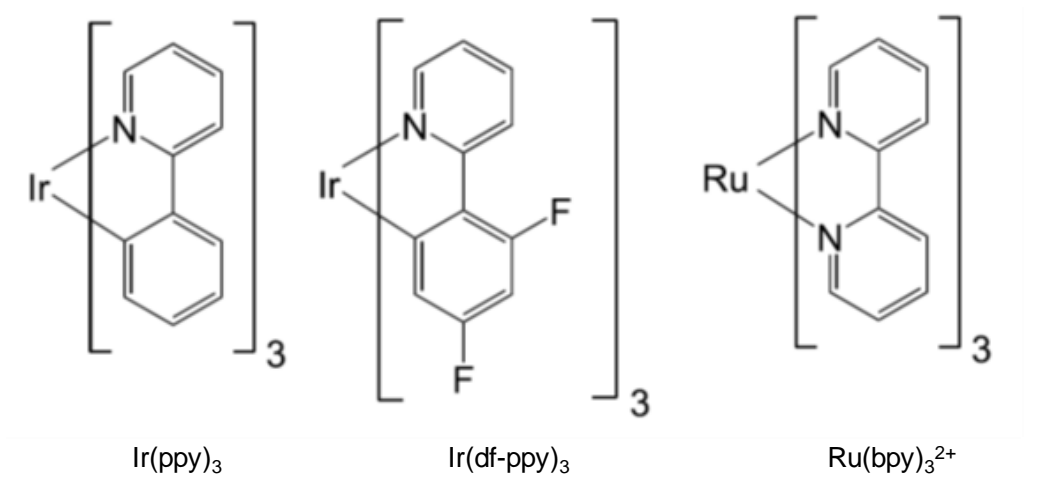


Figure 3.2 – Experimentally-obtained 3D-ECL emission matrix for system containing a mixture of 0.11 mM Ir(ppy)_3 and 0.14 mM Ir(df-ppy)_3 in the presence of 20 mM TPA. Working electrode: glassy carbon. Scan-rate: 25 mV/s. Reprinted from [54] with permission from The Royal Society of Chemistry.



Scheme 3.1 – Chemical structures of Ir(ppy)_3 and Ir(df-ppy)_3 . Chemical structure of Ru(bpy)_3^{2+} is shown as reference.

3.2. Modeling Conditions

Since homogeneous ECL systems were modeled in this part, 1D geometry shown in Figure 3.3 was used in the modeling. In the modeling of homogeneous ECL, calculations easily become very complicated and that then resulted in calculation failures because all the various reactions including the luminophore and co-reactant have to be calculated in all the calculation points in the model. And so, it is mandatory to decrease the calculation volume as much as possible. In the used model, solution area was divided into two domains to decrease the calculation volume. Since the maximum diffusion distance of $\text{TPA}\bullet^+$ was estimated to be ~ 5 μm or less [32], the reactions including $\text{TPA}\bullet^+$ can be considered only in the limited domain. Therefore, Solution Domain 1 having a height of 25 μm (~ 5 times than the estimated distance) was created in the solution area (the remaining domain was named as Solution Domain 2) to consider $\text{TPA}\bullet^+$ -related reactions only in this domain. Most calculations in this part were successfully completed with this effort.

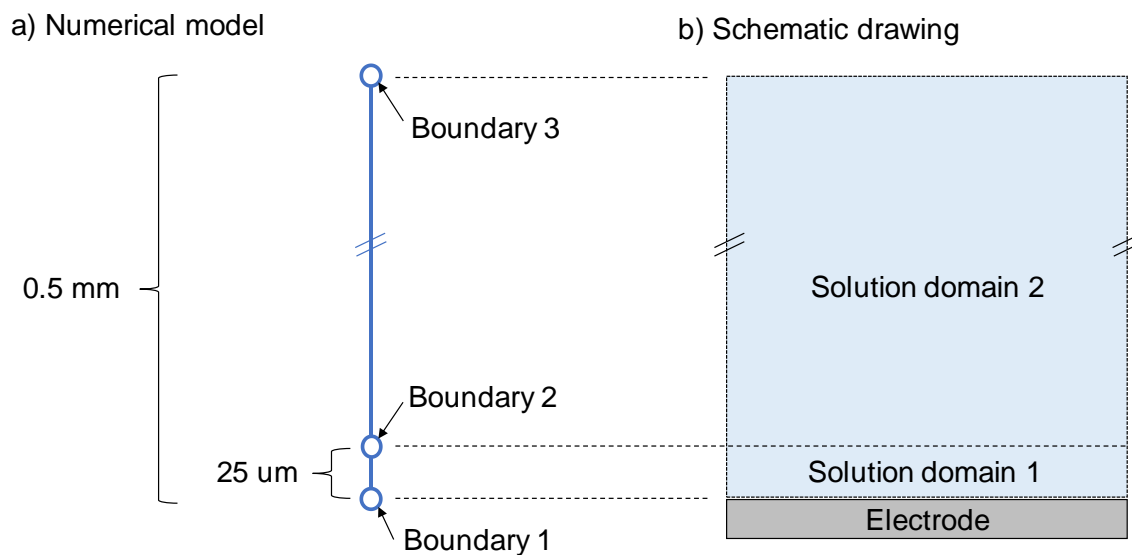


Figure 3.3 – Geometry used for numerical modeling of ECL for the Ir(ppy)₃/TPA system: a) the structure of the numerical model; b) schematic drawing corresponding to the numerical model.

Original parameters for calculations were determined based on the experimental studies on the Ir(ppy)₃/TPA system and studies on the Ru(bpy)₃²⁺/TPA system as shown in the previous part of this thesis. Table 3.2 summarizes the relevant general and reaction parameters used in the calculations. Some parameter values were adjusted in the middle of the study based on the obtained results. In this case, the solution is aprotic MeCN, and so the equilibrium of TPAH⁺ and TPA, which has to be considered in aqueous Ru(bpy)₃²⁺/TPA systems, was not considered. The rate constant for the ECL emission reaction (Ir(ppy)₃^{*} → Ir(ppy)₃ + ECL) was lower than that in the case of Ru(bpy)₃²⁺ based on the experimental studies [96]. For the quenching reaction (TPA^{•+} + Ir(ppy)₃^{*} → Ir(ppy)₃⁺ + P2), the rate

constant was optimized comparing the calculated ECL behavior and the experimental results.

For the numerical modeling of the multicolor ECL, another Ir-based luminophore with higher oxidation potential and shorter emission wavelength, Ir(df-ppy)₃, was added into the model for the Ir(ppy)₃/TPA system, as experimentally reported [54].

Table 3.2 - General and reaction parameters used in the modeling of ECL behavior for the Ir(ppy)₃/TPA system and multicolor-ECL behavior with the addition of Ir(df-ppy)₃.

a) General parameters (*1: used only in the multicolor-ECL modeling)

Parameter/item	Values/material
pH of solution	0 (MeCN)
Initial TPA concentration	20 mM (high) or 0.25 mM (low)
Initial Ir(ppy) ₃ concentration	0.25 mM for Ir(ppy) ₃ /TPA system 0.11 mM for multicolor-ECL system
Initial Ir(df-ppy) ₃ concentration *1	0.14 mM
Diffusion coefficient for species	$5 \times 10^{-6} \text{ cm}^2 \text{ s}^{-1}$
Potential scan rate	0.5 V s^{-1}
Temperature	25 °C
Working electrode	Glassy carbon
Reference electrode	Redox potential of ferrocene (~ 0.44 V vs. Ag AgCl)

b) Reactions considered for the Ir(ppy)₃/TPA system (P1 and P2: TPA derivatives)

#	Reaction	Constants	E° (vs. Fc)
1	TPA ↔ TPA• + e ⁻	k _f ^{TPA} = 0.1 cm s ⁻¹	E° _{TPA} = 0.50 V
2	TPA• ⁺ → TPA• + H ⁺	k _f ^{rTPA} = 3500 s ⁻¹	-
3	TPA• ↔ P1 + e ⁻	k _f ^d = 0.1 cm s ⁻¹	E° _d = -2.1 V
4	Ir(ppy) ₃ ↔ Ir(ppy) ₃ ⁺ + e ⁻	k _f ^o _{Ir} = 0.1 cm s ⁻¹	E° _{Ir} = 0.35 V
5	TPA• + Ir(ppy) ₃ ⁺ → Ir(ppy) ₃ * + P1	k _f ¹ = 10 ⁸ M ⁻¹ s ⁻¹	-
6	Ir(ppy) ₃ * → Ir(ppy) ₃ + ECL (~520 nm)	k _f ^{ECL} = 10 ⁵ s ⁻¹	-
7	TPA• ⁺ + Ir(ppy) ₃ * → Ir(ppy) ₃ ⁺ + P2	k _f ² = 10 ⁹ - 10 ¹³ M ⁻¹ s ⁻¹	-

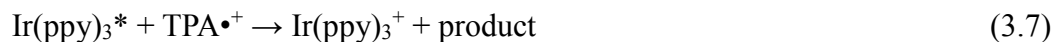
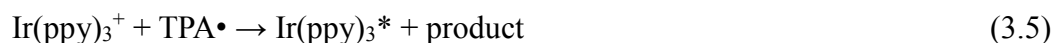
c) Reactions additionally considered for the multicolor ECL with Ir(df-ppy)₃

#	Reaction	Constants	E° (vs. Fc)
8	Ir(df-ppy) ₃ ↔ Ir(df-ppy) ₃ ⁺ + e ⁻	k _f ^o _{Ir2} = 0.1 cm s ⁻¹	E° _{Ir2} = 0.70 V
9	TPA• + Ir(df-ppy) ₃ ⁺ → Ir(df-ppy) ₃ * + P1	k _f ³ = 10 ⁷ M ⁻¹ s ⁻¹	-
10	Ir(df-ppy) ₃ * → Ir(df-ppy) ₃ + ECL (~495 nm)	k _f ^{ECL2} = 10 ⁵ s ⁻¹	-

3.3. Results and Discussion

a) Modeling of ECL from Ir(ppy)₃/TPA homogeneous system

Scheme 3.2 shows reactions considered in the numerical modeling of the Ir(ppy)₃/TPA system. As stated above, the proposed mechanism is that ECL significantly quenches due to the reaction of Ir(ppy)₃* and TPA•⁺ at high TPA concentrations, competing with the ECL emitting reaction (Ir(ppy)₃* → Ir(ppy)₃ + ECL). In this study, forward rate constant for the quenching reaction was parameterized and then the calculated ECL behavior was compared with the experimental results.



Scheme 3.2 - Reaction sequence of co-reactant ECL based on Ir(ppy)₃ and TPA.

Figure 3.4 shows calculated ECL behavior as a function of applied potential with different rate constants for the quenching reaction (Ir(ppy)₃* + TPA•⁺ → Ir(ppy)₃⁺ + product) in the case of a high TPA concentration of 20 mM. At a low rate constant of 10⁹ M⁻¹ s⁻¹, the ECL decay at high potentials after the ECL peak was similar to the decay

usually observed in other ECL systems, which means no significant ECL quenching was observed. However, increase in the rate constant significantly changed the ECL behavior. At a rate constant of $10^{12.2} \text{ M}^{-1} \text{ s}^{-1}$, rapid ECL decay that is very similar to the experimental results was obtained.

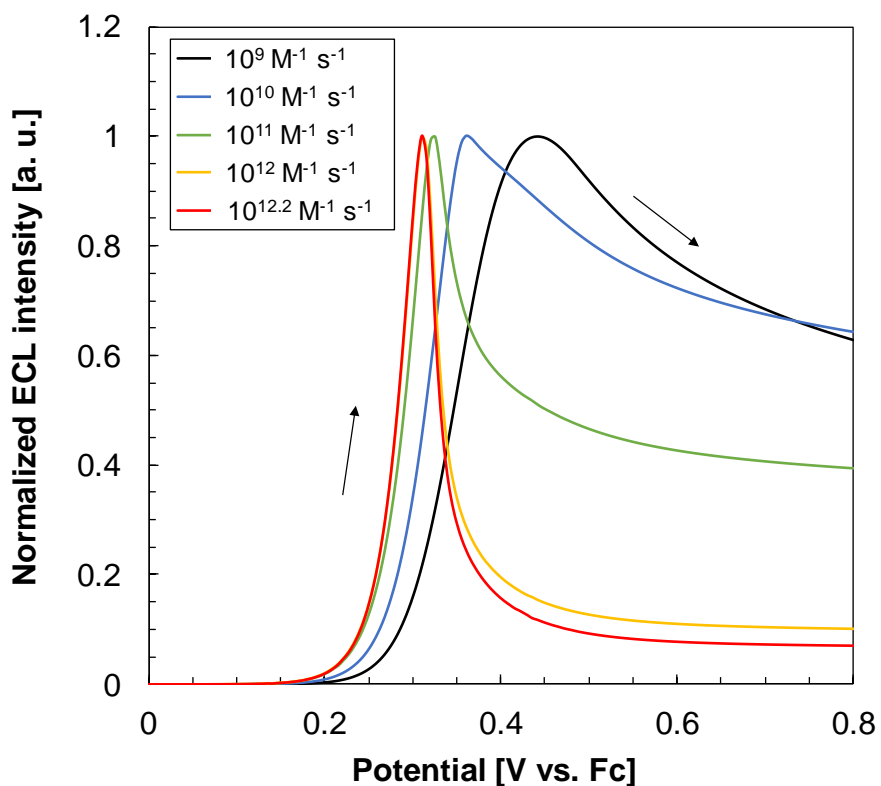


Figure 3.4 – Calculated influence of the rate constant for the quenching reaction on the ECL behavior for the Ir(ppy)₃/TPA system with high TPA concentration (20 mM). ECL intensity becomes smaller with higher rate constant; however, ECL intensities were normalized in this figure to compare the ECL behavior.

Next, ECL behavior with the high rate constant for the quenching reaction (= $10^{12.2} \text{ M}^{-1} \text{ s}^{-1}$) and low TPA concentration (0.25 mM) was investigated to clarify that the

influence of the rate constant for the quenching reaction is significant only at high TPA concentrations. Figure 3.5 shows the obtained ECL behaviors as a function of applied potential. At the low concentration, ECL did not significantly quench after the ECL peak as expected, and ECL behavior which is very similar to the experimental result was observed (see Figure 3.1). The results stated above clearly indicated that the reaction of $\text{Ir}(\text{ppy})_3^*$ with $\text{TPA}^{\bullet+}$ at high TPA concentration significantly quench ECL at high potential in the $\text{Ir}(\text{ppy})_3/\text{TPA}$ system, and this indication verifies the proposed mechanism from the theoretical point of view.

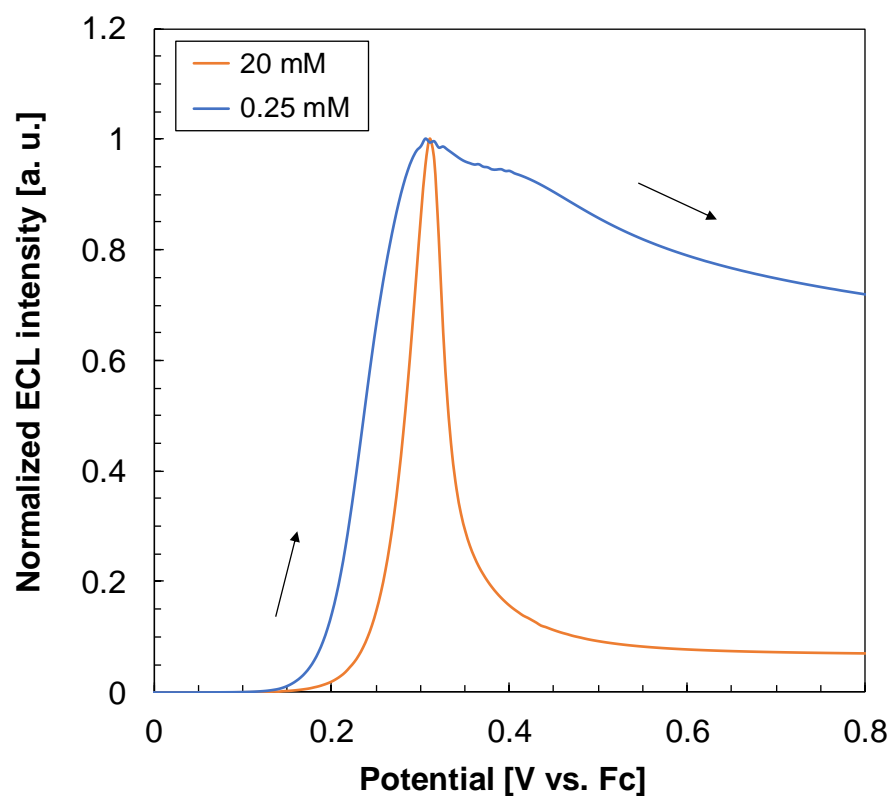


Figure 3.5 – Calculated ECL behaviors as a function of applied potential with a rate constant for the quenching reaction of $10^{12.2} \text{ M}^{-1} \text{ s}^{-1}$ and different TPA concentrations

(high: 20 mM; low: 0.25 mM). ECL intensity becomes smaller with higher rate constant; however, ECL intensities were normalized in this figure to compare the ECL behavior.

On the other hand, the behavior of the electrical current for the Ir(ppy)₃/TPA system was also investigated. One of the advantages of the numerical modeling is that the current behavior can be easily decomposed to the current behavior for each electrochemically-active specie to analyze the individual contribution to the entire system, although that is impossible in experimental studies. Figure 3.6 shows calculated current behaviors for for TPA and Ir(ppy)₃ as a function of applied potential with a rate constant for the quenching reaction of $10^{12.2} \text{ M}^{-1} \text{ s}^{-1}$ and a TPA concentration of 20 mM. Both current behaviors were as expected and very similar to the experimental results which were obtained in separate experiments for TPA and Ir(ppy)₃, respectively [54], [95]. This results further supports the validity of the proposed mechanism.

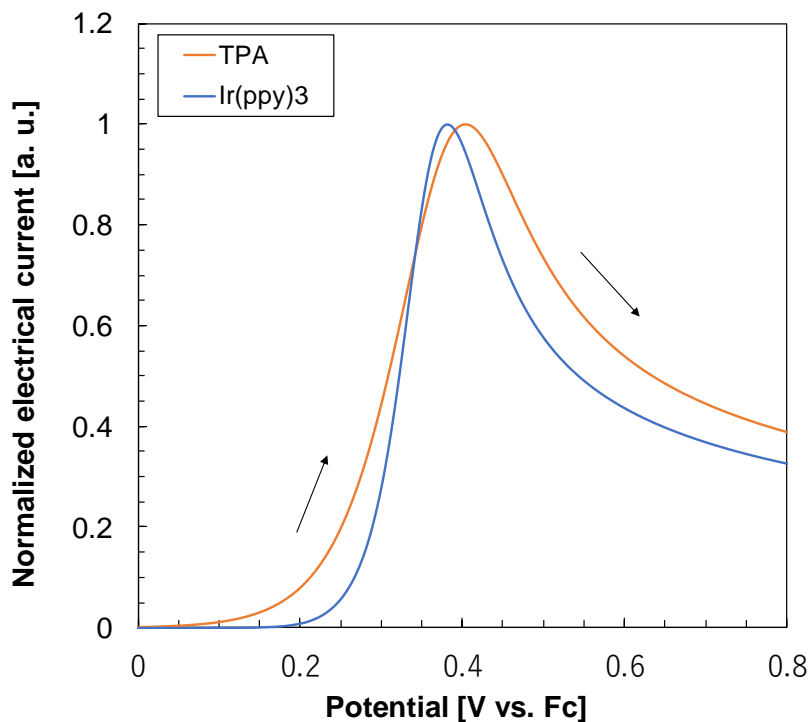
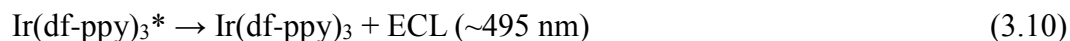
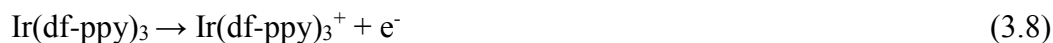


Figure 3.6 – Calculated electrical current behaviors for TPA and Ir(ppy)₃ as a function of applied potential with a rate constant for the quenching reaction of $10^{12.2} \text{ M}^{-1} \text{ s}^{-1}$ and a TPA concentration of 20 mM. Electrical current for TPA was higher than that for Ir(ppy)₃ due to the difference in the concentrations; however, electrical currents were normalized in this figure to compare the current behavior.

b) Modeling of multicolor ECL from solution containing Ir(ppy)₃, Ir(df-ppy)₃ and TPA

Since the quenching of ECL from Ir(ppy)₃ at high potential was successfully modeled in the previous section, the multicolor ECL system containing Ir(ppy)₃ and Ir(df-ppy)₃ was then modeled with the addition of reactions related to Ir(df-ppy)₃ into the model of the Ir(ppy)₃/TPA system (see Scheme 3.3). The quenching reaction was not

considered for Ir(df-ppy)₃* because the oxidation potential of Ir(df-ppy)₃* is more positive ($E^{\circ} \approx -1.8$ V vs. Fc) than Ir(ppy)₃* by ~ 0.3 V.



Scheme 3.3 - Reaction sequence added to the Ir(ppy)₃/TPA system to model the multicolor ECL system containing Ir(ppy)₃, Ir(df-ppy)₃ and TPA.

Figure 3.7 shows calculated ECL behavior as a function of applied potential for the multicolor ECL system in a solution containing Ir(bpy)₃ and Ir(df-bpy)₃, and TPA under conditions similar to those of Figure 3.1 and Figure 3.2. A wavelength of 510 nm for the ECL intensity was chosen because ECL emission efficiency for the two luminophores are nearly the same (ECL intensity was adjusted considering ECL spectrum obtained in the experiments) [95]. As shown in the figure, the two ECL waves corresponding to the oxidation potentials of Ir(bpy)₃ and Ir(df-bpy)₃ were observed separately, as expected from the experimental results (see Figure 3.2). This results indicated that the quenching reaction analyzed for the Ir(ppy)₃/TPA system also contributes ECL systems comprising multiple luminophores.

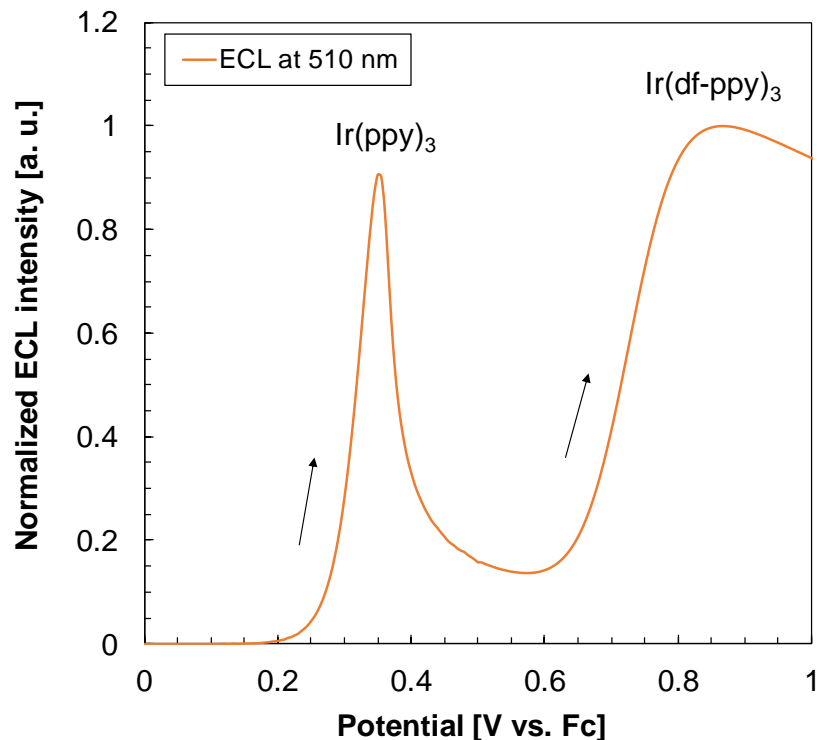
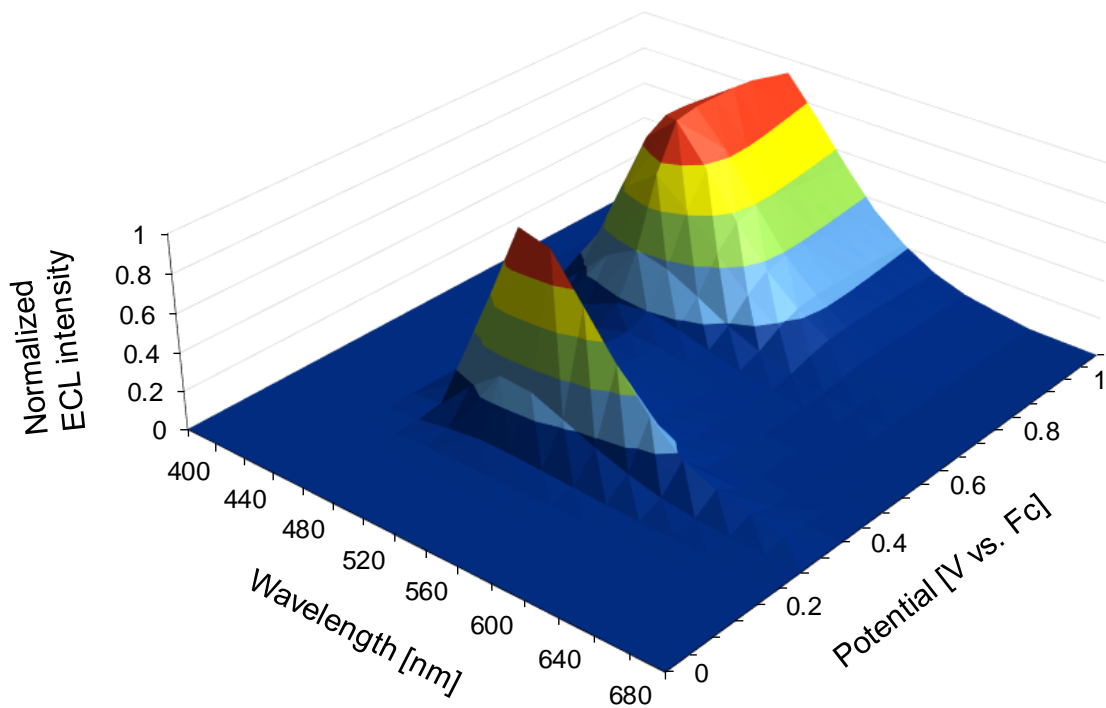


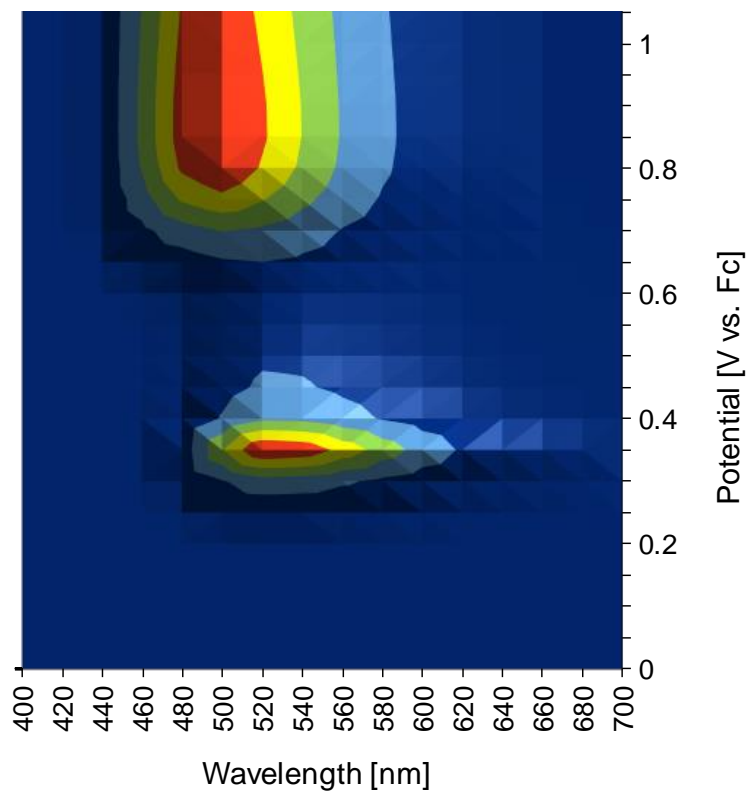
Figure 3.7 – Calculated normalized ECL intensity at a wavelength of 510 nm as a function of applied potential for the multicolor ECL system with solution containing Ir(bpy)₃ and Ir(df-bpy)₃, and TPA.

Finally, a 3D emission map of wavelength versus applied potential and ECL intensity was generated. The ECL intensity behavior for each luminophore was calculated and then integrated with the emission spectrum for the corresponding luminophore to draw the 3D graph (the emission spectra were not calculated but obtained by fitting the experimental results) [95]. Figure 3.8 shows a calculated 3D graph of emission wavelength versus applied potential and ECL intensity. As shown in the figure, the obtained 3D graph was very similar to that drawn from the experimental results (see Figure 3.2).

These results stated above indicated for ECL from Ir(ppy)₃ and TPA that, ECL is quenched by the reaction of Ir(ppy)₃* and TPA•⁺ at high TPA concentrations due to the lower oxidation potential of Ir(ppy)₃* than that of Ru(ppy)₃^{2+*}, but this quenching phenomenon can realize a multicolor ECL system whose emission wavelength is selectable by the applied potential with the combination of another luminophore which has a different oxidation potential and different emission wavelength. These results are in line with the mechanism proposed by Hogan's group and support it from theoretical viewpoint.



a) Bird-view



b) Top-view

Figure 3.8 – Calculated 3D graph for calculated normalized ECL intensity for the multicolor ECL system with solution containing Ir(bpy)₃ and Ir(df-bpy)₃, and TPA.

4. Part B: Numerical Modeling of Heterogeneous ECL from a Luminophore-Doped Nanoparticle

Reprinted with permission from [97]. Copyright 2015 American Chemical Society.

4.1. Background

In the 2000s, some researchers reported on the doping of a number of luminophores into a silica nanoparticle to obtain brighter light emission from one target material in the photoluminescence field [98], [99]. Since their reports, ECL from $\text{Ru}(\text{bpy})_3^{2+}$ -doped silica nanoparticles (Ru-DSNPs, see Figure 4.1) in the combination of TPA as a co-reactant has been reported by many researchers [100]–[105]. Zanarini and co-researchers in Paolucci's group reported 1000-fold increase in ECL efficiency compared to the conventional single-luminophore system [106]. They suggested a mechanism from their experimental results, that $\text{TPA}^{\bullet+}$ and TPA^{\bullet} can penetrate inside the Ru-DSNP to make $\text{Ru}(\text{bpy})_3^{2+}$ molecules excited at a lot of sites in the Ru-DSNP, and that electron hopping between $\text{Ru}(\text{bpy})_3^{3+}$ and $\text{Ru}(\text{bpy})_3^{2+}$ molecules can happen inside the Ru-DSNP. In this part of thesis, the numerical modeling of ECL from a Ru-DSNP under solution containing TPA as the co-reactant was carried out to clarify the reaction mechanism for ECL generation in detail.

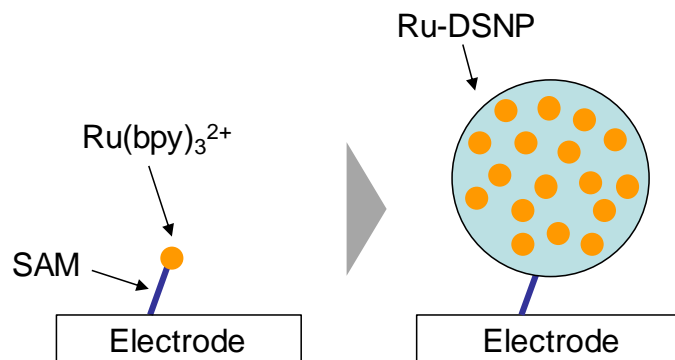


Figure 4.1 – Concept for a Ru-DSNP to obtain higher ECL efficiency (SAM: self-assembled monolayer). Note that the Ru-DSNP is attached on the electrode via SAM (not via a magnetic force) in this case.

4.2. Modeling and Measuring Conditions

a) Modeling conditions

Generally, numerical modeling was carried out based on the previous experimental conditions [106]. However, the diameter of the working electrode was modified to 0.5 mm, which is smaller by one eighth than the setup in the experimental study (2.0 mm), to keep the computational time low even with decreased mesh size. Figure 4.2 shows the 2D geometry used in this study. The diameter and height of the electrochemical cell used in the modeling were 2 mm and 1 mm. A nanoparticle was put at the center of the working electrode surface. The mesh size inside and on the particle surface was set to $<1.5 \text{ nm}^2$ to obtain reliable calculation results. The mesh size on the electrode was set to be $<1 \text{ }\mu\text{m}^2$ in smooth connection with the mesh geometry on the particle.

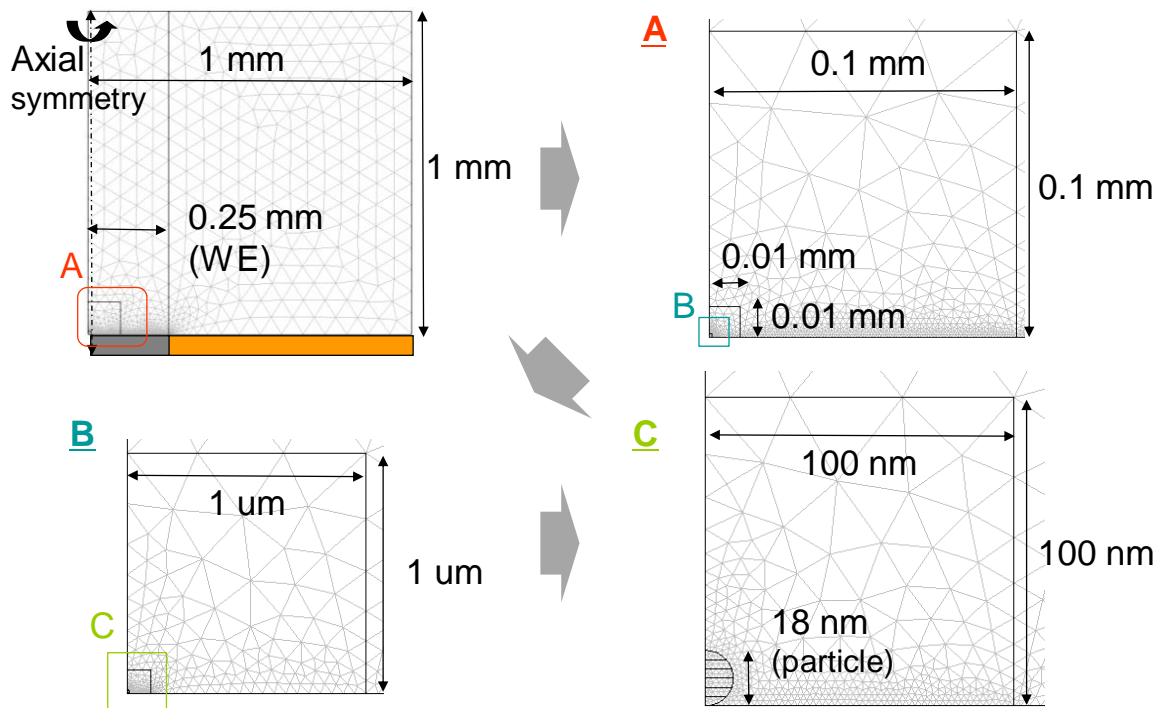


Figure 4.2 – Geometry used in the numerical modeling of ECL from a Ru-DSNP.

Original parameters for calculations were determined based on the experimental study and on a number of existing studies on the $\text{Ru}(\text{bpy})_3^{2+}/\text{TPA}$ system [24], [87], [89], [106]. Table 4.1 summarizes the relevant general and reaction parameters used in the calculations. Some parameter values were adjusted in the middle of the study based on the obtained results. The model comprises two sources for ECL generation in order to efficiently model the two ECL waves observed in the experimental curves: reactions derived from TPA oxidation were firstly modeled to analyze the first ECL wave at ~ 0.9 V vs. $\text{Ag}|\text{AgCl}$ (Step 1) while, in order to analyze the second ECL wave, the direct $\text{Ru}(\text{bpy})_3^{2+}$ oxidation at ~ 1.2 V was also taken into account (Step 2). Details are explained in the next section. Diffusion coefficient for all species inside the particle was estimated to

be ten times lower than that in the bulk solution. Finally, and importantly, the rate of the $\text{TPA}\cdot^+$ deprotonation (Reaction 3) was assumed to be potential dependent in the region of TPA oxidation for reasons that are explained below. For Reactions 2 and 5, we used a high electron transfer constant of 10 cm s^{-1} because the electrode surface is modified with Ru-DSNPs and then should be more hydrophobic than a bare gold electrode as suggested by the experimental study. For Reaction 10, electron hopping between $\text{Ru}(\text{bpy})_3^{2+}$ and $\text{Ru}(\text{bpy})_3^{3+}$ inside the Ru-DSNP was modeled using the diffusion of the luminophores (details are explained later in this part).

Table 4.1 - General and reaction parameters used in the modeling of ECL behavior for the Ru-DSNP/TPA system (P1: iminium product of TPA).

a) General parameters

Parameter/item	Value/material
pH of solution	7.5 (0.1 M phosphate buffer)
Initial TPA concentration ($[\text{TPAH}^+] + [\text{TPA}]$)	30 mM
Diameter of a particle	18 nm
$\text{Ru}(\text{bpy})_3^{2+}$ concentration in the particle	0.35 M (650 molecules in the particle)
Diffusion coefficient	$5 \times 10^{-6} \text{ cm}^2 \text{ s}^{-1}$ (in solution) $5 \times 10^{-7} \text{ cm}^2 \text{ s}^{-1}$ (inside the particle) $5 \times 10^{-5} \text{ cm}^2 \text{ s}^{-1}$ (only for H^+)
Potential scan rate	0.5 V s^{-1}
Temperature	25 °C
Working electrode	Gold modified with Ru-DSNP
Reference electrode	Ag AgCl

b) Reaction parameters for Step 1 (at ~0.9 V)

#	Reaction	Constants	E° (vs. Ag AgCl)
1	$\text{TPAH}^+ \leftrightarrow \text{TPA} + \text{H}^+$	$K_a = 10^{-10.4} \text{ M}$ $K_f^a = 10^{6.6} \text{ s}^{-1}$	-
2	$\text{TPA} \leftrightarrow \text{TPA}\cdot + \text{e}^-$	$k_f^{\text{TPA}} = 10 \text{ cm s}^{-1}$	$E_{\text{TPA}}^{\circ} = 0.88 \text{ V}$
3	$\text{TPA}\cdot^+ \leftrightarrow \text{TPA}\cdot + \text{H}^+$	$k_f^{r\text{TPA}} = \text{variable}$ $k_b^{r\text{TPA}} = 1.08 \times 10^6 \text{ M}^{-1} \text{ s}^{-1}$	-
4	$\text{TPA}\cdot \rightarrow \text{P1} + \text{e}^-$	$k_f^d = 10 \text{ cm s}^{-1}$	$E_d^{\circ} = -1.7 \text{ V}$
5	$\text{TPA}\cdot + \text{Ru}(\text{bpy})_3^{2+} \rightarrow \text{Ru}(\text{bpy})_3^+ + \text{P1}$	$k_f^1 = 10^{10} \text{ M}^{-1} \text{ s}^{-1}$	-
6	$\text{TPA}\cdot^+ + \text{Ru}(\text{bpy})_3^+ \rightarrow \text{Ru}(\text{bpy})_3^{2+*} + \text{TPA}$	$k_f^2 = 10^6 \text{ M}^{-1} \text{ s}^{-1}$	-
7	$\text{Ru}(\text{bpy})_3^{2+*} \rightarrow \text{Ru}(\text{bpy})_3^{2+} + \text{ECL}$	$k_f^{\text{ECL}} = 10^{7.2} \text{ s}^{-1}$	-

c) Reaction parameters for Step 2 (at ~1.2 V)

#	Reaction	Constant	E° (vs. Ag AgCl)
8	$\text{Ru}(\text{bpy})_3^+ \leftrightarrow \text{Ru}(\text{bpy})_3^{2+} + \text{e}^-$	$k_{\text{Ru}^+}^{\circ} = 1 \text{ cm s}^{-1}$	$E_{\text{Ru}^+}^{\circ} = -1.48 \text{ V}$
9	$\text{Ru}(\text{bpy})_3^{2+} \leftrightarrow \text{Ru}(\text{bpy})_3^{3+} + \text{e}^-$	$k_{\text{Ru}^{2+}}^{\circ} = 1 \text{ cm s}^{-1}$	$E_{\text{Ru}^{2+}}^{\circ} = 1.16 \text{ V}$
10	$\text{Ru}(\text{bpy})_3^{2+} + \text{Ru}(\text{bpy})_3^{3+} \rightarrow \text{Ru}(\text{bpy})_3^{3+} + \text{Ru}(\text{bpy})_3^{2+}$	$D_{\text{eh}} = 5 \times 10^7 \text{ cm}^2 \text{ s}^{-1}$	-
11	$\text{TPA}\cdot + \text{Ru}(\text{bpy})_3^{3+} \rightarrow \text{Ru}(\text{bpy})_3^{2+*} + \text{P1}$	$k_f^3 = 10^7 \text{ M}^{-1} \text{ s}^{-1}$	-
12	$\text{TPA} + \text{Ru}(\text{bpy})_3^{3+} \rightarrow \text{TPA}\cdot^+ + \text{Ru}(\text{bpy})_3^{2+}$	$k_f^4 = 1 \text{ M}^{-1} \text{ s}^{-1}$	-

b) Experimental conditions

Cyclic voltammetry to analyze the behavior of a Ru-DSNP on a gold electrode was carried out with a commercial potentiostat (Bio-Logic SP-300). The ECL measurements were carried out in water with 0.1 M phosphate buffer (pH = 7.5) as supporting electrolyte with 30 mM of TPA as the co-reactant. Gold sputtered on Si substrate with a diameter of 2 mm was used as the working electrode, and platinum wire was used as the counter electrode. The reference electrode was saturated Ag|AgCl. The working electrode was kept under 3-mercaptopropylsilane solution for 1 night to form a self-assembled monolayer (SAM) on the electrode.

4.3. Results and Discussion

a) Experimental results

This research focused on the report by Zanarini and co-researchers [106], whose aim was to show the proof-of-principle signal amplification in ECL-based bioassays by replacing the single $\text{Ru}(\text{bpy})_3^{2+}$ with DSNPs in which a number of the $\text{Ru}(\text{bpy})_3^{2+}$ molecules were doped. To prove the effectiveness of this strategy under conditions that are as close as possible to the real analytical case (where the Ru-based luminophore is confined at the electrode surface via the immune complex), DSNPs were modified by 3-mercaptopropyltriethoxysilane so as to form a self-assembled monolayer onto the gold electrode surface, via metal-thiol binding. ECL can then be generated from the monolayer via the co-reactant mechanism by oxidizing TPA at the modified electrode surface. Given the high porosity of the nanoparticle, $\text{TPA}^{\bullet+}$ and TPA^{\bullet} can diffuse inside the particle and ECL will be generated from both the $\text{Ru}(\text{bpy})_3^{2+}$ molecules located on the surface of the particle and from those inside the particle. Figure 4.3 shows electrical current and ECL intensity behaviors as a function of applied potential, which were measured during a cyclic voltammetric experiment with a gold working electrode functionalized with the Ru-DSNP under 30 mM TPA and 0.1 M phosphate buffer (pH 7.5), as previously reported.

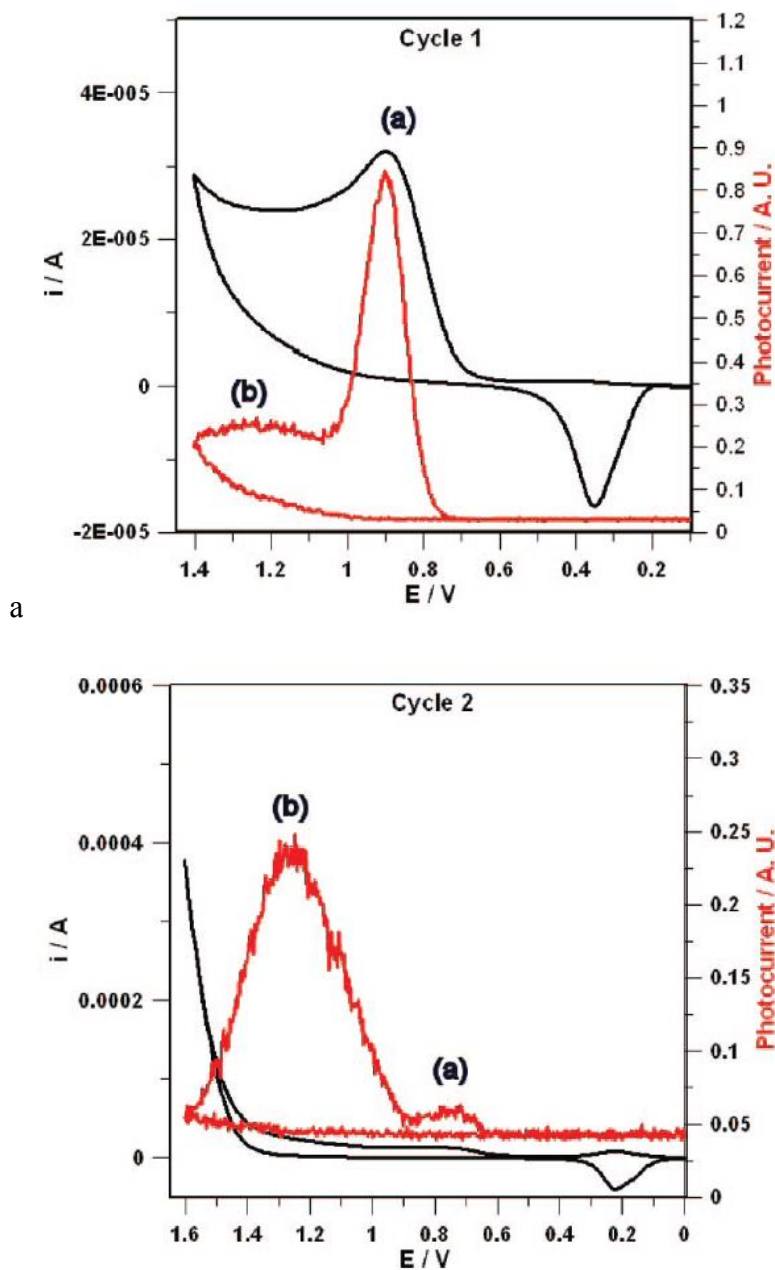
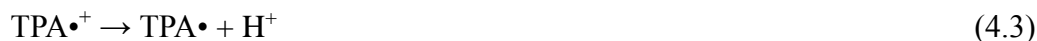
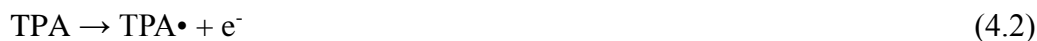


Figure 4.3 – Experimentally-obtained first and second cycle light/current/potential curve of a gold substrate functionalized with DSNP-SH self-assembled layer under 0.1 M phosphate buffer (pH 7.4) containing 30 mM TPA. Switching method: cyclic voltammetry; scan rate, 0.5 V/s. Potentials are versus saturated Ag|AgCl. Reprinted with permission from [106]. Copyright 2009 American Chemical Society.

In this experiment, ECL behavior exhibited two separate waves in the first positive potential scan (Cycle 1). The first ECL wave, which is shown as a) in the figure, had its peak at ~ 0.9 V (vs. Ag|AgCl) which corresponds to the oxidation potential of TPA oxidation. The second ECL wave, which is labeled as b) in the figure, had its peak at ~ 1.2 V which corresponds to the oxidation potential of $\text{Ru}(\text{bpy})_3^{2+}$. The peak height of the first ECL wave was ~ 3.5 times higher than that of the second peak in the first cycle, and the first ECL wave rapidly decreased after the peak in a range of 0.9 - 1.1 V. On the other hand, the current exhibited a peak at ~ 0.9 V corresponding to the peak of the first ECL wave. However, no current peak was observed at ~ 1.2 V. In the second potential sweep (cycle 2), current and ECL intensity for the first ECL wave decreased drastically; however, the intensity of the second ECL wave almost remained. In this context, the numerical modeling of the ECL for the Ru-DSNP/TPA system was carried out in two steps: Step 1 for the first ECL wave triggered by TPA oxidation at ~ 0.9 V and Step 2 for the second ECL wave generated by both TPA and $\text{Ru}(\text{bpy})_3^{2+}$ oxidation at ~ 1.2 V.

b) Step 1: Modeling of reactions triggered by TPA oxidation for the first ECL wave

As stated above, the first ECL wave corresponding the oxidation of TPA at ~ 0.9 V was firstly modeled with the consideration of reactions shown in Scheme 4.1. This reaction pathway that does not require direct $\text{Ru}(\text{bpy})_3^{2+}$ oxidation at the electrode was proposed to be dominant in the heterogeneous ECL employing luminophore-connected microbeads because the luminophores are physically prevented to be directly oxidized at the electrode surface due to the large distance across which tunneling electron transfer should take place [32]. TPA oxidation at the working electrode ($\text{TPA} \rightarrow \text{TPA}\cdot + \text{e}^-$) was considered as an irreversible electrochemical reaction as the other researches in this field. $\text{TPA}\cdot$ consumption by its oxidation at the electrode was also considered in this numerical modeling.



Scheme 4.1 – Reactions considered in Step 1 to model the first ECL wave triggered by TPA oxidation at the working electrode.

Figure 4.4 shows ECL intensity as a function of applied potential calculated in Step 1. As stated above, the lifetime of $\text{TPA}\cdot^+$ is critical for the behavior of the first ECL wave because $\text{TPA}\cdot^+$ and $\text{TPA}\cdot$ are both necessary to generate the excited state of $\text{Ru}(\text{bpy})_3^{2+}$ in this potential range. ECL intensity can be governed by the deprotonation equilibrium of $\text{TPA}\cdot^+$ ($\text{TPA}\cdot^+ \leftrightarrow \text{TPA}\cdot + \text{H}^+$). At first in this study, two different forward rate constants for the deprotonation equilibrium were used (540 and 3500 s^{-1}) as suggested in previous studies [24], [32]. However, these values could not adequately calculate the first ECL wave. In particular, what it was not possible to reproduce was the very rapid decay of ECL intensity that was observed starting at $\sim 0.9 \text{ V}$ in the experiment (see also Figure 4.3).

In a recent paper, Chen and Zu investigated the influence of the surface oxidation of a glassy carbon electrode on ECL intensity and showed a significant decrease in ECL intensity on the glassy carbon electrode that was previously and purposely oxidized [26]. They proposed from their various experiments that the oxidative consumption of $\text{TPA}\cdot$ ($\text{TPA}\cdot \rightarrow \text{P1} + \text{e}^-$) should be accelerated by the presence of oxygen-containing species on the electrode surface, which can cause a significant reduction of ECL intensity due to the shorter lifetime of $\text{TPA}\cdot^+$.

With the consideration of the results for this study, this acceleration of $\text{TPA}\cdot$ consumption on the oxidized surface was introduced into the numerical modeling of ECL from a Ru-DSNP. In other words, a “variable” deprotonation rate constant for $\text{TPA}\cdot^+$, whose value depends on the applied potential to consider the oxidization of the electrode surface. Figure 4.5 shows the deprotonation rate constant for $\text{TPA}\cdot^+$ as a function of the applied potential used in this study. In this case, since the gold working electrode was

pretreated by the thiol product, the gold electrode surface was covered by a self-assembled monolayer (SAM). The SAM can prevent the formation of the oxide layer until its electrochemical removal from the electrode surface. This removal would start occurring at ~ 0.9 V, and after that the electrode surface would be immediately oxidized (experimental data clarifying this hypothesis will be shown later in this part). Based on this context, the variable forward rate constant for the deprotonation of $\text{TPrA}^{\bullet+}$, that gradually changes from 540 s^{-1} to 3500 s^{-1} in a range of 0.9 V to 1.1 V based on the piecewise cubic interpolation method was introduced. As a consequence of that, as clearly shown in Figure 4.4, the rapid decay in ECL intensity starting at ~ 0.9 V was very well calculated.

Another effect that can be associated to the electrode surface oxidation is the decrease in TPA oxidation rate at the electrode. This effect was also considered in the model as a decreasing electron transfer rate constant for TPA oxidation, which was decreased by up to three orders of magnitude at potentials ≥ 0.9 V in the same manner as the decreasing rate constant for the $\text{TPrA}^{\bullet+}$ deprotonation. However, the introduction of this variable parameter did not well calculate the ECL behavior, and therefore this hypothesis was discarded.

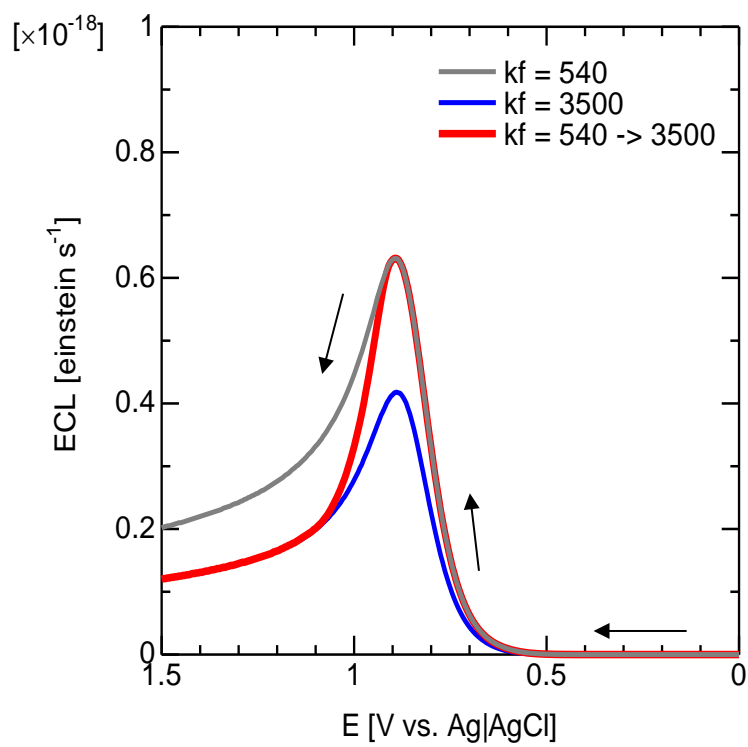


Figure 4.4 - Calculated ECL intensity as a function of applied potential for reactions derived from TPA oxidation for the first ECL wave (Step 1).

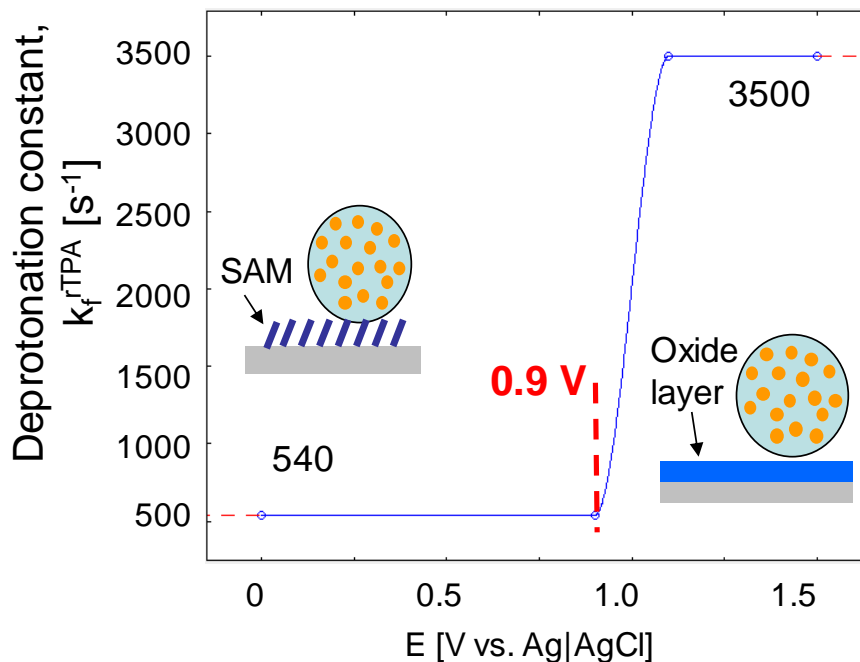


Figure 4.5 - Deprotonation rate constant for $TPA^{\bullet+}$ as a function of applied potential with the consideration of the SAM removal from the electrode surface and subsequent electrode surface oxidation.

In order to verify the hypothesis that the self-assembled monolayer containing the Ru-DSNP detaches from the electrode surface at ~ 0.9 V, cyclic voltammetric experiments (not calculations) were carried out on a gold electrode before and after modification with 3-mercaptopropylsilane (Figure 4.6). Before the modification, the anodic current indicating gold electrode surface oxidation was observed already from ~ 0.6 V as expected. On the other hand, no anodic current was observed until ~ 0.9 V after the modification. These results indicated that the DSNPs film is able to protect the electrode surface

hindering significantly the gold oxidation process, while, after its anodic stripping, it would take place very rapidly.

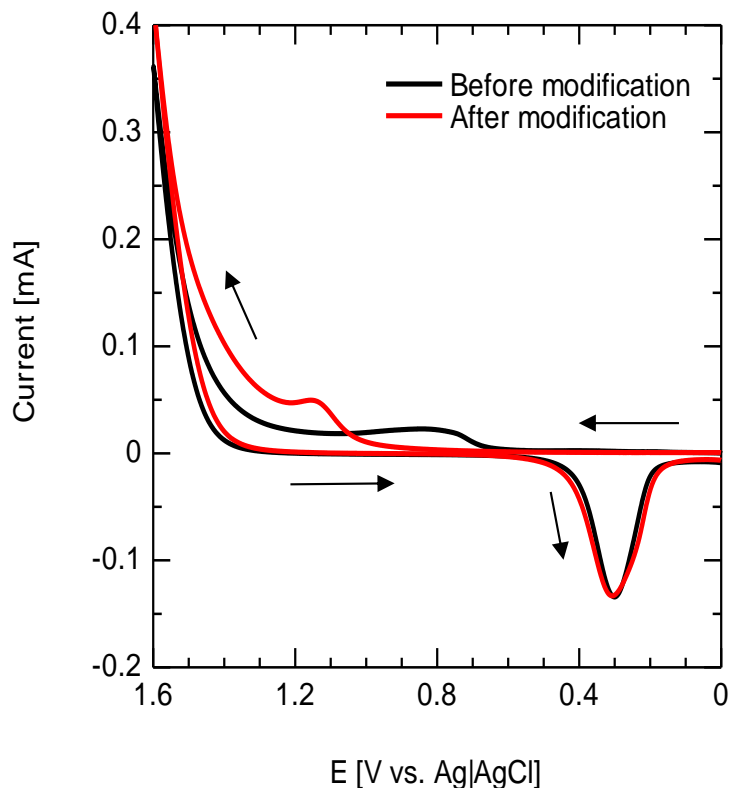


Figure 4.6 - Cyclic voltammograms of gold electrode under phosphate buffer with a pH of 7.5 before and after modification by a 3-mercaptopropylsilane self-assembled monolayer.

The effect of the surface modification of the electrode on ECL behavior has been experimentally pointed out in previous reports [17]–[20], [31], [107]–[110]. A key factor affecting the efficiency of ECL generation is the chemical state of the electrode surface. The electrode may undergo surface modifications during the potential scan used for the ECL generation such as the formation of oxide layers and adsorption/desorption of

surfactants, which can significantly affect the emission intensity. Various strategies were adopted to bind the recognition site onto the electrode surface and to protect the latter from undesired modifications. Self-assembled monolayers having long chain thiols on gold electrode have been proposed for this purpose because they form compact and effective surface coverage. However, the gold-thiol bond is unstable under the conditions typically used in co-reactant ECL (high potentials) and the detachment of the thiols takes place upon the potential application. The effects of surfactants on ECL emission were also widely investigated as the oxidation of hydrophobic TPA molecule under aqueous solution is strongly affected by the presence of surfactants. The effect of the electrode surface modification on ECL behavior indicated in this study was generally in line with the hypothesis from the experimental reports, and this study clarifies the role of the electrode surface modification in the ECL mechanism in more detail.

Figure 4.7 shows a voltammetric curve calculated under the conditions used to calculate the ECL signal in Figure 4.4. The calculated electrical current from the model also accurately fit the experimental electrical current up to ~ 1.1 V. Difference between the calculated and measured current values is attributed to the different active electrode surface area. Only one particle was used in the numerical model but it was estimated a concentration of 3×10^{-8} M in the experimental set up; however, the behavior of the calculated current fit that obtained from the experiment well. At higher potentials of >1.1 V, there was a small discrepancy between the calculated current behavior and the experimental result. A better calculated current would be obtained with the

superimposition of the oxygen evolving reaction from the water electrolysis (this approach is discussed later in this part).

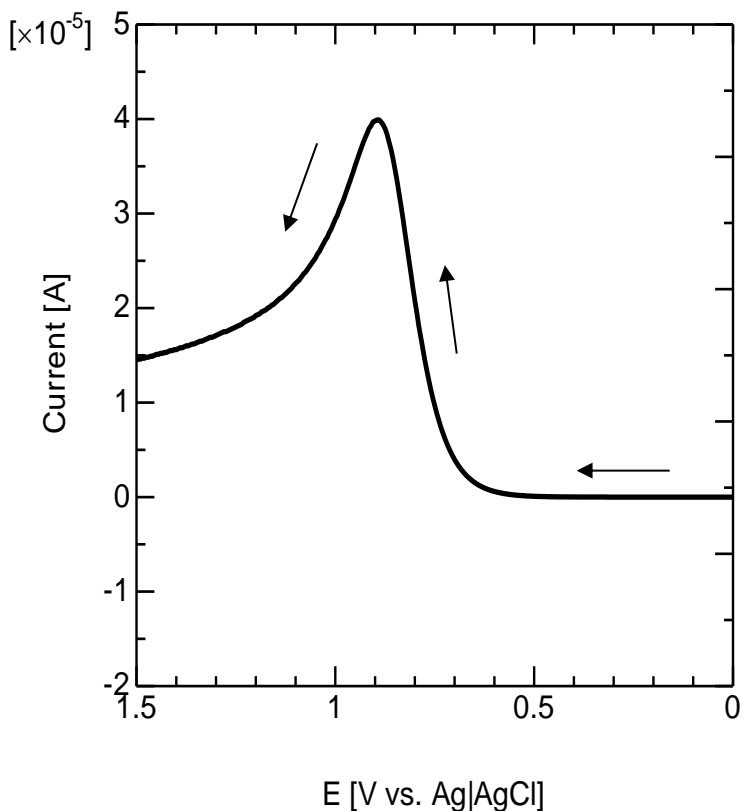


Figure 4.7 - Calculated electrical current as a function of applied potential for reactions derived from TPA oxidation for the first ECL wave (Step 1).

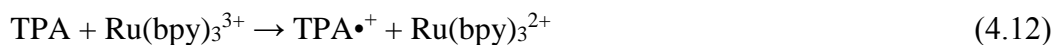
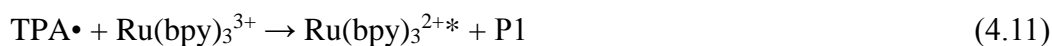
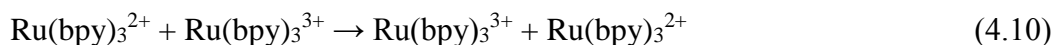
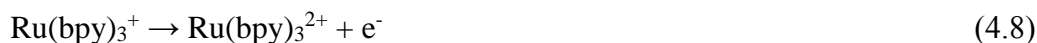
Changes in the concentration of the reaction species during potential sweep was also analyzed to clarify the ECL mechanism in more detail. As shown in Equation 3.6, both $\text{TPA}^{\bullet+}$ and $\text{Ru}(\text{bpy})_3^+$ are necessary to generate the excited state of $\text{Ru}(\text{bpy})_3^{2+}$. $\text{Ru}(\text{bpy})_3^+$ is generated by the reaction of TPA^{\bullet} and $\text{Ru}(\text{bpy})_3^{2+}$ as shown in Equation 3.5. Here, Equation 3.4 shows that TPA^{\bullet} is also directly consumed at the electrode surface to generate

the iminium product (P1). Therefore, TPA[•] is rapidly depleted in the following ways: 1) at the electrode surface to generate P1; 2) after diffusion within the DSNPs to generate Ru(bpy)₃⁺ by the reaction with Ru(bpy)₃²⁺. It is well known that the concentration of TPA^{•+} having short lifetime is critical for ECL generation; however, the concentration of TPA[•] can be also critical. The analysis for this model actually found that the concentration of TPA[•] was nearly zero inside and around the DSNP during the potential sweep (e.g., 0.01 mM or less at E = 0.9 V). The reason for this low TPA[•] concentration around the Ru(bpy)₃²⁺ molecules is the small diameter of the DSNP (small distance to the electrode). This result indicated that the influence of the TPA^{•+} deprotonation equilibrium, not only the TPA^{•+} concentration but also the TPA[•] concentration, on ECL behavior would be more significant in the Ru-DSNP/TPA system with respect to the other ECL systems.

In conclusion of this section, the results stated above indicated that changes in the electrode surface functionality during potential scan affects the TPrA^{•+} deprotonation equilibrium and this in turn plays an important role in the ECL behavior of the Ru-DSNP/TPA system at gold electrodes.

c) Step 2: Modeling of reactions triggered by TPA and Ru(bpy)₃²⁺ oxidation for the second ECL wave

As a further step towards a full numerical modeling of the various features observed in the experimental curve shown in Figure 4.3, another reaction pathway for the generation of ECL, involving the direct oxidation of Ru(bpy)₃²⁺ at the electrode, was additionally included in the model as Step 2 (Scheme 4.2).



Scheme 4.2 - Reactions considered additionally in Step 2 to model the second ECL wave triggered by TPA and Ru(bpy)₃²⁺ oxidation at the working electrode. Equation 10 is considered for the self-exchange reaction taking place within the DSNPs (electron hopping).

The direct oxidation of the Ru(bpy)₃²⁺ molecules immobilized inside the DSNPs takes place by tunnelling and cannot extend beyond a small distance from the electrode surface (typically ≤ 3 nm). Since the diameter of the DSNP is about 18 nm and the total number of doping molecules per nanoparticle is 650 as estimated from the value of DSNP

doping ratio, the mean distance between two luminophores inside the DSNP is about 2 nm. This makes electron hopping a viable mechanism for the oxidation of $\text{Ru}(\text{bpy})_3^{2+}$ molecules that are more distant than the tunnelling length from the electrode surface. The self-exchange process was modeled as a diffusion process involving the $\text{Ru}(\text{bpy})_3^{3+}$ species (generated at the electrode surface) with a diffusion coefficient D_{eh} (modeling parameter) [111]. The maximum height for the electron hopping (h_{eh}), i.e., the distance from the electrode surface over which the hopping may take place, was then parameterized.

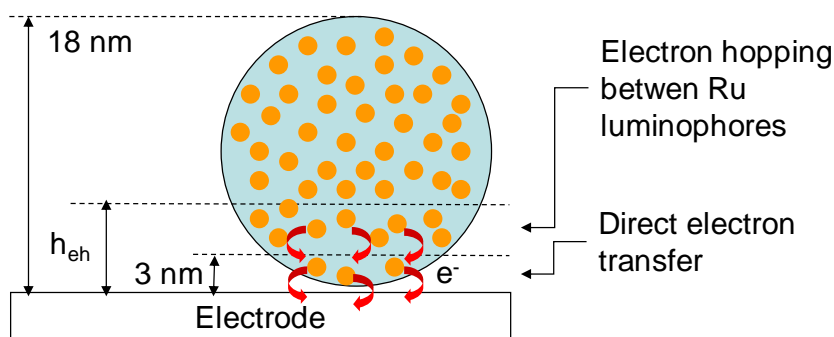


Figure 4.8 - Model for direct electron transfer and electron hopping on $\text{Ru}(\text{bpy})_3^{2+}$ considered in Step 2.

Figure 4.9 shows calculated ECL intensity as a function of applied potential with different maximum electron hopping heights for the luminophores inside the DSNP. Note that the optimal value was obtained by the comparison of the calculated ECL intensities with the experimental values (the peak ratio of the first and second ECL waves). When $h_{\text{eh}} = 3 \text{ nm}$, the second ECL wave was not clearly observed. Increasing the maximum height, the second ECL wave appeared with increasing intensity. Electric current was not affected

by the maximum height because the concentration of $\text{Ru}(\text{bpy})_3^{2+}$ is extremely low in the model. These results indicated that electron hopping between luminophores also plays an important role in ECL behavior for the Ru-DSNP/TPA system. We found out that the optimal hopping height was 6 nm that gives the best agreement with the experimental results.

In this study, the influence of the diffusion of DSNPs to the solution after the detachment of the SAM from the electrode surface was not considered. As shown in the actual ECL behavior shown in the experimental work (Figure 4.3), the height of the second ECL peak did not change in the second potential sweep. This result indicates that the DSNPs do not diffuse significantly towards the solution after the detachment of the SAM from the electrode surface. The density of the DSNPs should be much higher than water and that makes the DSNP difficult to diffuse to the solution.

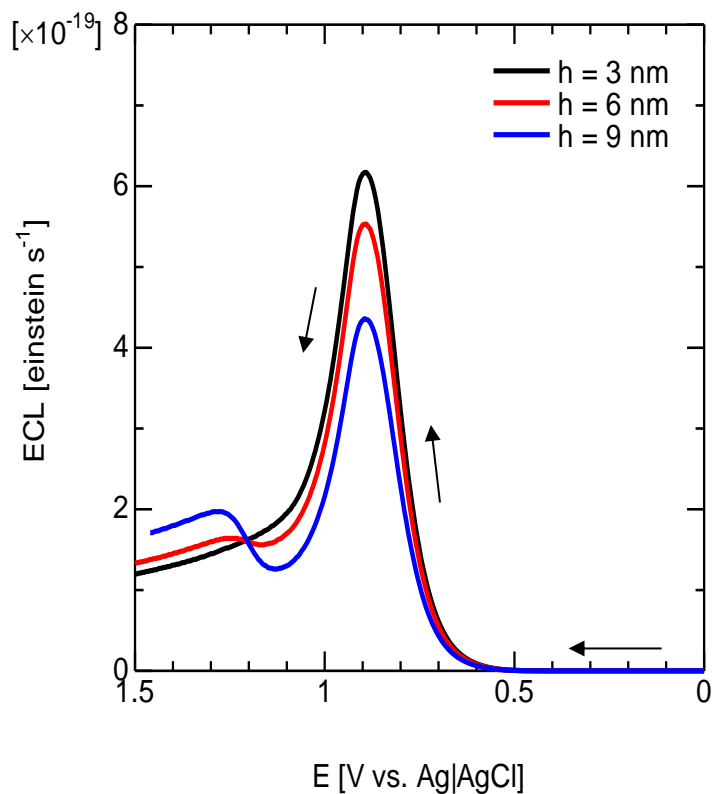


Figure 4.9 - Calculated ECL intensity as a function of applied potential for reactions for Step 2 with different maximum electron hopping heights for the luminophores inside the DSNP.

Finally, Figure 4.10 shows the overall calculated ECL intensity and current as a function of applied potential. The results obtained in this study indicate that electrode surface functionality change during potential scan and electron hopping between the luminophores play important roles in the ECL behavior for the Ru-DSNP/TPA system.

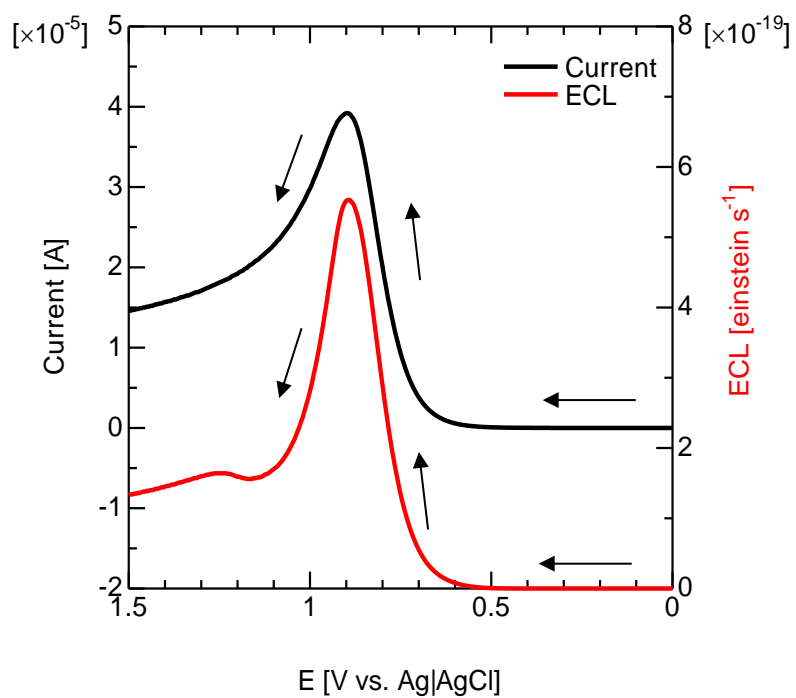


Figure 4.10 - Calculated current and ECL intensity as a function of applied potential for reactions for the Ru-DSNP/TPA system.

d) Consideration of electrical current derived from oxygen evolving reaction during potential application

As stated in Step 1, there was a small discrepancy between the calculated current behavior and the experimental result at high potentials of $>1.1\text{V}$, and a better calculated current would be obtained with the superimposition of the oxygen evolving reaction from water electrolysis. Here, as an additional study, the consideration of current derived from the oxygen evolution by the integration of current data obtained in experiments was carried out. The current data that was measured for the analysis of the electrode surface modification was utilized. In particular, the cyclic voltammogram for the gold electrode before the modification, which means bare gold electrode, was used to estimate the electrical current for oxygen evolution (see Figure 4.6).

Figure 4.11 shows calculated current behavior (with ECL behavior) as a function of applied potential. As shown in the figure, the behavior of electric current for the numerical modeling became very similar to that for the experiment. This results indicated that the numerical model established in this study very well explains the reactions in ECL emission from a Ru-DSNP under solution containing TPA.

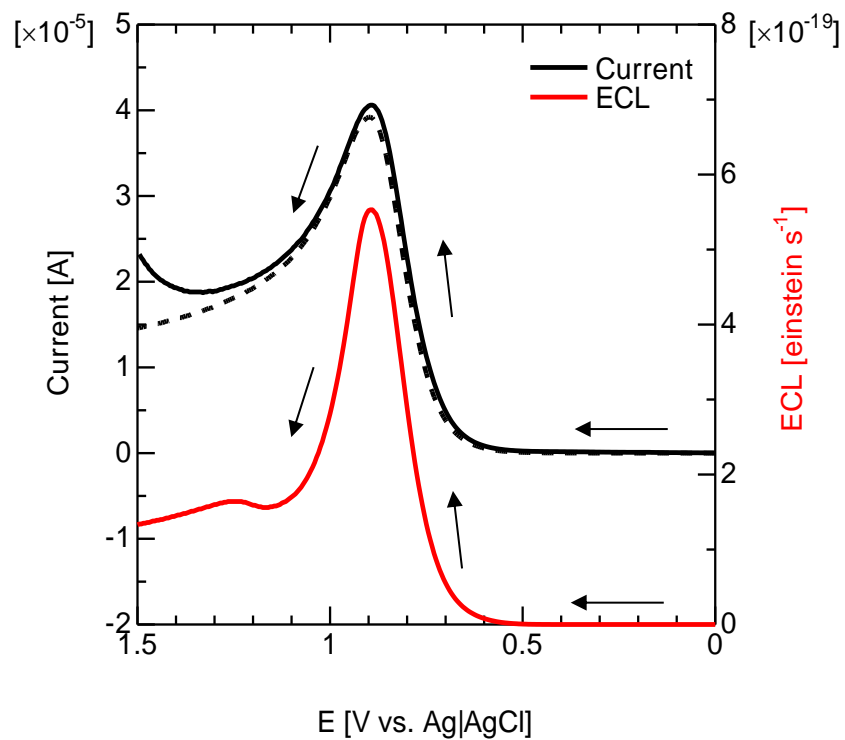


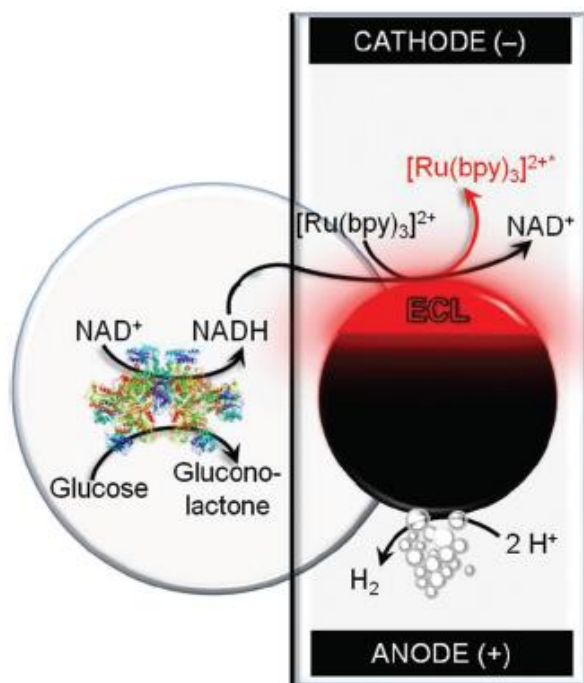
Figure 4.11 - Calculated electric current and ECL with the consideration of the current derived from oxygen evolution by the integration of current data obtained in experiment (broken line: current without considering oxygen evolution).

A bipolar electrochemistry system has an advantage for analytical applications that a number of electrodes can be set in the electrolyte solution and can be controlled simultaneously with a single external power supply. This interesting feature of the bipolar electrochemistry system can realize an ECL sensing-array system that has multiple BPEs. If each BPE is differently modified with species that are related to ECL reactions, a lot of different analytes could be detected or quantified simultaneously within a system. Crooks and co-researchers have reported a bipolar electrochemistry system that has ~1000 BPEs by means of microfabrication technology [112].

In 2012, Sentic and co-researchers reported a novel co-reactant ECL systems based on the bipolar electrochemistry [121]. They put a glassy carbon bead into a glass capillary filled with solution that contains $\text{Ru}(\text{bpy})_3^{2+}$ and TPA, and then applied a strong electrical field to generate ECL on the surface of the glass carbon bead. They succeeded in observing ECL from this bipolar electrochemistry system, and also observed an interesting phenomenon, i.e., that the bead moves up inside the capillary after the potential application. They suggested the generation of hydrogen bubbles due to water electrolysis on the lower side of the bead, where negative potential is applied, gives buoyancy to the bead.

Sentic and co-researchers then applied their system into the analysis of glucose concentration in an unknown sample [122]. They used nicotinamide adenine dinucleotide (NADH) as the co-reactant, instead of TPA to detect glucose. It is known that NAD^+ , which is ECL-inactive, reacts with glucose to produce NADH in the presence of glucose

dehydrogenase (GDH). Then, the concentration of glucose can be determined with the ECL intensity by using solution containing NAD^+ and $\text{Ru}(\text{bpy})_3^{2+}$. Scheme 5.2 shows the concept for this bipolar ECL system for glucose analysis reported in the study.



Scheme 5.2 – Concept for bipolar ECL system for glucose analysis using $\text{Ru}(\text{bpy})_3^{2+}$ and NADH . Reprinted from [122] with permission from The Royal Society of Chemistry.

Figure 5.1 shows electrical current and ECL intensity as a function of applied potential under various glucose concentrations, obtained in the experimental study [122]. They carried out the potential scan after 30 minutes of incubation after mixing GDH, NAD^+ and glucose in 100 mM phosphate buffer (pH = 7.4). The first current wave at ~ 1.2 V (vs. $\text{Ag}|\text{AgCl}$) is due to the oxidation of NADH and the second wave at ~ 1.6 V is due to the oxidation of $\text{Ru}(\text{bpy})_3^{2+}$. ECL is observed at $= 1.6$ V, corresponding to the oxidation of $\text{Ru}(\text{bpy})_3^{2+}$. Increase in glucose concentration results in the increase in ECL intensity,

which indicates this system can be used for the determination of glucose concentration in an unknown sample.

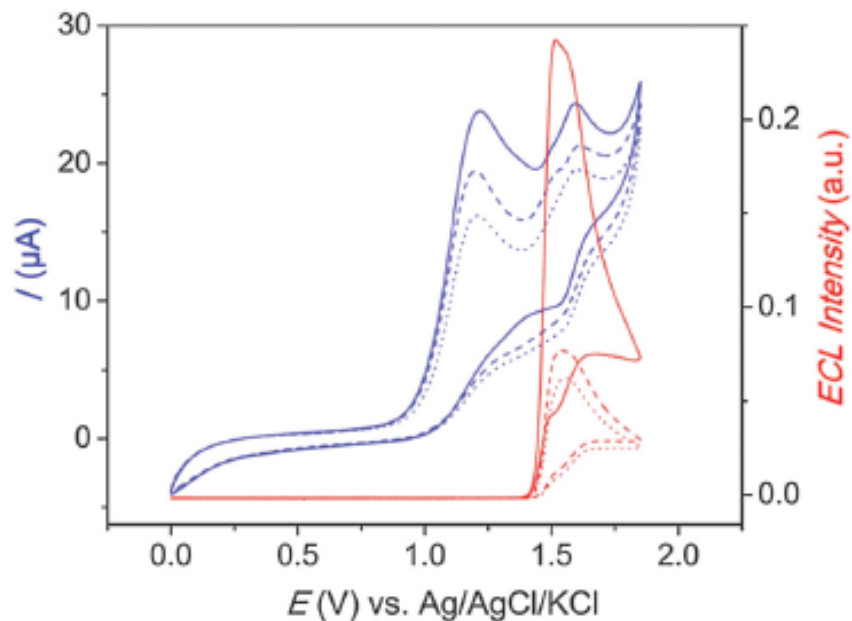


Figure 5.1 – Experimentally-obtained electrical current (blue lines) and ECL intensity (red lines) as a function of applied potential in the bipolar ECL system with phosphate buffer of pH =7.4 containing 1.5 mM $\text{Ru}(\text{bpy})_3^{2+}$, 10 mM NAD^+ and various glucose concentrations (dotted lines for 5 mM; dashed lines for 10 mM; solid lines for 40 mM). Scan rate: 0.05 V/s. Reprinted from [122] with permission from The Royal Society of Chemistry.

They also reported that ECL at the top of the bead quenches in a few seconds after potential application. In their first report on the bipolar ECL based on $\text{Ru}(\text{bpy})_3^{2+}$ and TPA, they suggested that this quenching is due to local pH reduction caused by the oxygen generation during potential application [121]. Figure 5.2 shows the proposed mechanism and experimentally-analyzed ECL intensity profiles on this phenomenon. They observed the pH value at the top of the bead decreased to ~ 4 after the potential

application, which can reduce the concentration of ECL-active TPAH in the solution in this case.

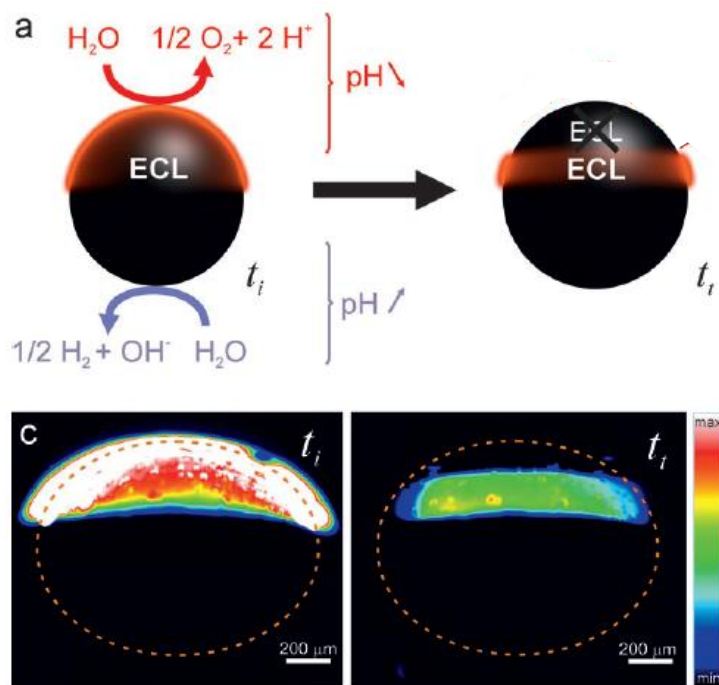


Figure 5.2 – Proposed mechanism and experimentally-analyzed ECL intensity profiles (t_i : initial state, t_t : state after transient time) for ECL quenching at the top of the bead in the bipolar ECL system based on $\text{Ru}(\text{bpy})_3^{2+}$ and TPA. Reprinted from [121] Copyright 2012 John Wiley & Sons.

In this part of the thesis, the bipolar ECL system based on $\text{Ru}(\text{bpy})_3^{2+}$ and NADH for the analysis of glucose was modeled to verify the proposed reaction mechanism with focus on the ECL quenching. Note that the movement of the bead due to the hydrogen generation is not considered in this study.

5.2. Modeling Conditions

In this part, both 1D and 2D modelings were carried out for the numerical modeling. In this system, since the polarization of the beads by external electrical field induces potential inside the bead, the applied potential is not uniform inside the bead. And so, the 1D modeling based on a usual planar working electrode with uniform potential was first carried out to determine reaction parameters, and then the 2D modeling was performed to model the bipolar system using the parameters determined in the 1D modeling.

1) Conditions for 1D modeling

The geometry used in this part was the same as that for the Ir(ppy)₃/TPA system, which was shown in this thesis. Table 5.1 summarizes the general and reaction parameters used in the 1D modeling. Several parameters were determined based on the past experimental studies [121], [122]. Some parameter values were adjusted in the middle of the study based on the obtained results.

Table 5.1 – General and reaction parameters used in the modeling of ECL behavior for the bipolar ECL system.

a) General parameters

Parameter/item	Value/material
pH of solution	7.4 (0.1 M phosphate buffer)
Initial NADH concentration (estimated glucose concentration)	0.2 mM (5 mM glucose), 0.4 mM (10 mM glucose) or 1.6 mM (40 mM glucose)
Initial Ru(bpy) ₃ ²⁺ concentration	1.5 mM

Diffusion coefficient for species	$5 \times 10^{-6} \text{ cm}^2 \text{ s}^{-1}$
Potential scan rate	1 V s^{-1}
Temperature	$25 \text{ }^\circ\text{C}$
Working electrode	Glassy carbon
Reference electrode	Ag AgCl

b) Considered reactions and relevant parameters

#	Reaction	Constants	E° (vs. Ag AgCl)
1	$\text{NADH} \leftrightarrow \text{NADH}^{\bullet+} + \text{e}^-$	$k_f^{\text{NADH}} = 10^{-2} \text{ cm s}^{-1}$	$E^\circ_{\text{NADH}} = 1.15 \text{ V}$
2	$\text{NADH}^{\bullet+} \rightarrow \text{NAD}^\bullet + \text{H}^+$	$k_f^{\text{TPA}} = 10^4 \text{ s}^{-1}$	-
3	$\text{NAD}^\bullet \leftrightarrow \text{NAD}^+ + \text{e}^-$	$k_f^{\text{d}} = 10^{-2} \text{ cm s}^{-1}$	$E^\circ_{\text{d}} = -1.7 \text{ V}$
4	$\text{Ru}(\text{bpy})_3^{2+} \leftrightarrow \text{Ru}(\text{bpy})_3^{3+} + \text{e}^-$	$k_{\text{Ru}2}^\circ = 10^{-2} \text{ cm s}^{-1}$	$E^\circ_{\text{Ru}2} = 1.5 \text{ V}$
5	$\text{NAD}^\bullet + \text{Ru}(\text{bpy})_3^{3+}$ $\rightarrow \text{Ru}(\text{bpy})_3^{2+*} + \text{NAD}^+$	$k_f^1 = 10^{10} \text{ M}^{-1} \text{ s}^{-1}$	-
6	$\text{Ru}(\text{bpy})_3^{2+*} \rightarrow \text{Ru}(\text{bpy})_3^{2+} + \text{ECL}$	$k_f^{\text{ECL}} = 10^{7.2} \text{ s}^{-1}$	-
7	$\text{H}_2\text{O} \leftrightarrow 1/2 \text{ O}_2 + 2\text{H}^+ + \text{e}^-$	$k_{\text{H}_2\text{O}}^\circ = 10^{-2} \text{ cm s}^{-1}$	$E^\circ_{\text{H}_2\text{O}} = 2.38 \text{ V}$

2) Conditions for 2D modeling

In the 2D modeling, a bead with a diameter of 1.0 mm was placed in the center of a cylinder with an inner diameter of 1.1 mm. Similar to the 1D modeling, the area with a distance of 25 μm or less from the bead surface was considered the area for ECL reaction to decrease the calculation complexity. The potential inside the bead depends on the strength of the external electric field and comparative position to the direction of the electric field (the potential is simply proportional to the position). Figure 5.3 shows the potential inside the bead induced by the external electric field. ECL reaction occurs on

the upper side of the bead because the reaction is triggered by the positive potential application. In the modeling, the potential on the bead was gradually applied (linearly saturated in one second) for the reduction of the calculation load, and then the potential was kept for 4 seconds for analysis.

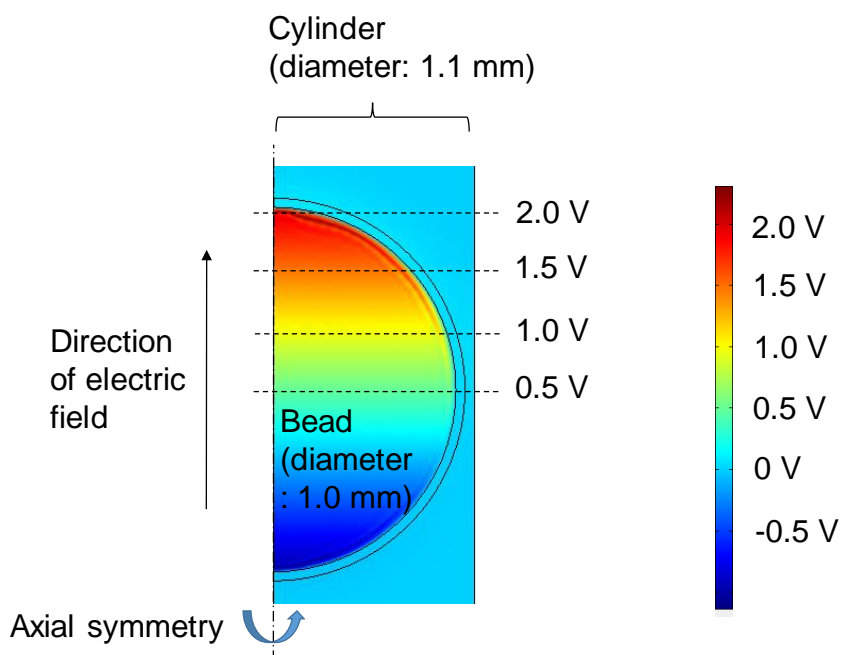
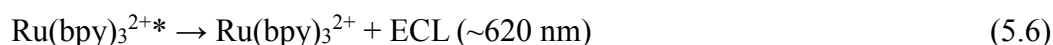


Figure 5.3 – Gradient potential inside the bead in the 2D modeling for the bipolar ECL system. Potential values are versus Ag|AgCl.

5.3. Results and Discussion

Scheme 5.3 shows reactions considered in the modeling of the bipolar ECL system. The excited state of $\text{Ru}(\text{bpy})_3^{2+}$ is generated by the reaction of NAD^\bullet with $\text{Ru}(\text{bpy})_3^{3+}$, which are produced by the oxidation of NADH and $\text{Ru}(\text{bpy})_3^{2+}$ at the working electrode.

The water electrolysis reaction ($\text{H}_2\text{O} \rightarrow 1/2 \text{O}_2 + 2\text{H}^+ + \text{e}^-$) was considered to analyze the influence of local pH change at the top of the bead during the potential application.



Scheme 5.3 - Reaction sequence of co-reactant ECL based on $\text{Ru}(\text{bpy})_3^{2+}$ and NADH.

Figure 5.4 shows calculated current density and normalized ECL intensity obtained in the 1D modeling. The three electrical current waves at $\sim 1.2 \text{ V}$, 1.6 V and $>1.7 \text{ V}$ (vs. $\text{Ag}|\text{AgCl}$) were observed, corresponding to the oxidation potentials of NADH, $\text{Ru}(\text{bpy})_3^{2+}$ and water (oxygen evolution), respectively. The height of current wave for the NADH oxidation changed according to the NADH concentration when the concentration was adjusted. The ECL wave was observed at $\sim 1.55 \text{ V}$, which corresponds to the onset potential for the oxidation of $\text{Ru}(\text{bpy})_3^{2+}$. Also, the height of the ECL wave showed a good correlation with the NADH concentration. The calculated results stated above were well in line with the experimental results. The calculated current density for NADH oxidation was smaller than the current density obtained in the experiment, probably due to the

background current in the experiment. Closer current behavior could be obtained with the consideration of the background current.

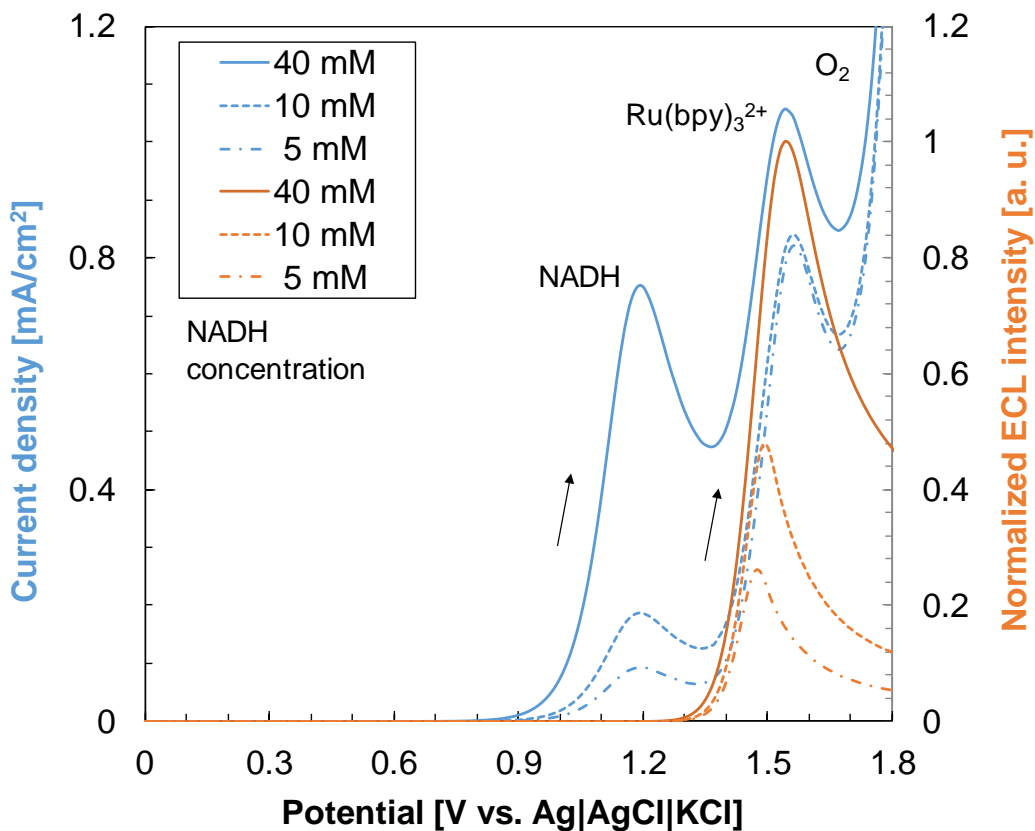


Figure 5.4 – Calculated current density and normalized ECL intensity as a function of applied potential obtained from the 1D modeling for the bipolar ECL system (NADH concentration: 5, 10 or 40 mM).

In the 1D modeling, the change in pH at working electrode during potential application was also analyzed. Figure 5.5 shows calculated pH at the working electrode and current density as a function of applied potential. As shown in the figure, the pH at the

working electrode rapidly decreased at potentials of 1.8 V or higher due to water electrolysis ($\text{H}_2\text{O} \rightarrow 1/2 \text{O}_2 + \text{H}^+ + \text{e}^-$) at the working electrode.

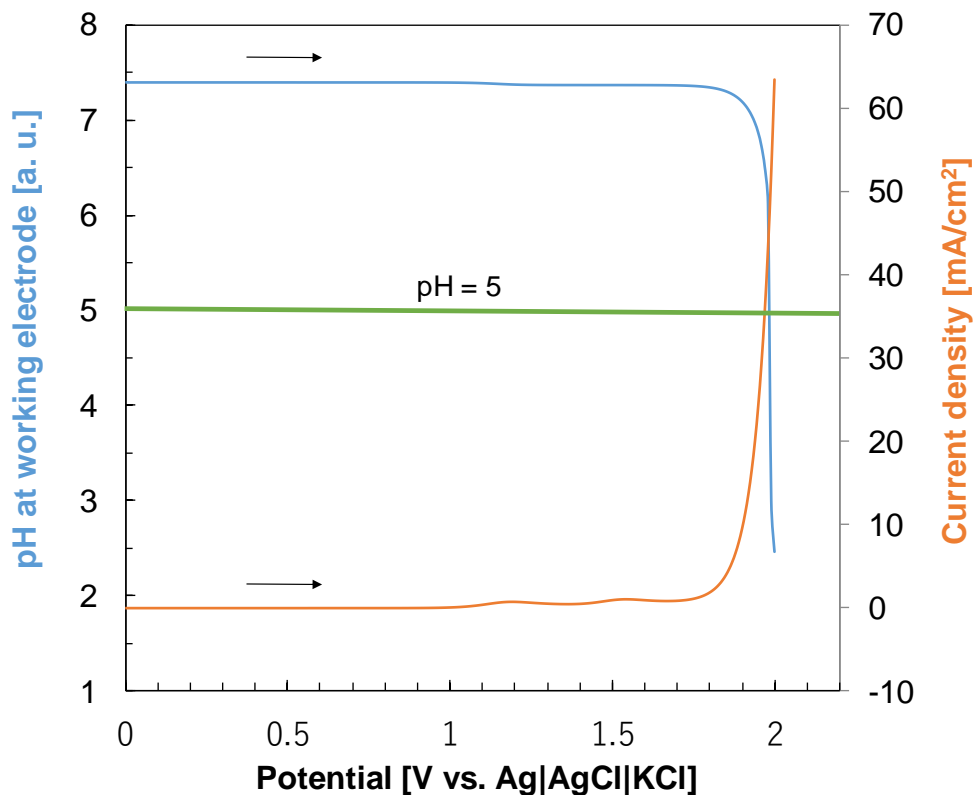
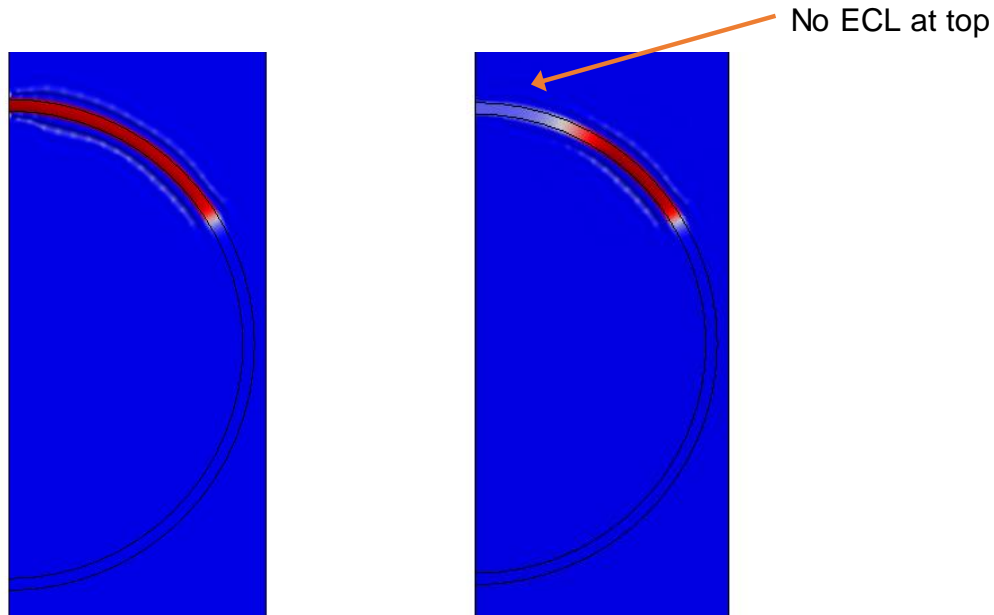


Figure 5.5 – Calculated pH at the working electrode and current density as a function of applied potential in the 1D modeling for the bipolar ECL system.

Finally, 2D modeling was carried out to calculate ECL behavior for the bipolar ECL system. Figure 5.6 shows calculated ECL on the bead surface at three seconds from the potential application with or without the consideration of the local pH change. Without the consideration of the local pH change, ECL was observed on the upper area of the bead (until $\sim 1/3$ from the top). On the other hand, with the consideration of the local pH change, calculation results showed that ECL was not observed at the top of the bead. This

calculation result was very much in line with the experimental results. In the 1D modeling, it was shown that the pH of the solution becomes less than 5 after the potential application. It has been reported that ECL cannot be observed at pH or 5 or less when NADH is used as a co-reactant [70]. And so, this study indicated that ECL quenches within a few seconds from the potential application due to the pH change at the surface of the bead. The results for this study were well in line with the experimental results, and this study supports the validity of the proposed mechanism for the bipolar ECL system.



a) Without local pH change

b) With local pH change

Figure 5.6 – Calculated ECL (red: high emission; blue: no emission) on the bead surface at three seconds after the potential application with or without the consideration of the local pH change in the 2D modeling for the bipolar ECL system. Note: ECL emission in this figure is shown with a width of 25 μm for visualization. Actual emission mainly occurs at the surface of the bead (distance: $<1 \mu\text{m}$).

5.4. Modeling of Spatially-Resolved Multicolor Bipolar ECL

1) Background

This year, Li and co-researchers in Sojic's group have reported with Hogan's group a bipolar ECL system using Ir(ppy)_3 [123], whose ECL quenching at high potential was previously analyzed in detail in this thesis. They focused on the fact that potential at BPE surface is gradient, and then suggested a specially-resolved multicolor ECL system with the combination of Ir(ppy)_3 and Ru(bpy)_3^{2+} . Figure 5.7 shows the side-view of ECL at Pt wire (BPE) in CH_3CN solution containing Ir(ppy)_3 , Ru(bpy)_3^{2+} and TPA under external potential application. When an external potential of 12 V is applied (note that external potential is not the potential at BPE), multicolor ECL from green to orange is observed at the surface of the Pt wire. Ir(ppy)_3 emits green ECL (peak: ~ 520 nm) under potential application of ~ 0.8 V (vs. Ag|AgCl) [54], and Ru(bpy)_3^{2+} emits orange ECL (peak: ~ 620 nm) under potential application of ~ 1.2 V at a Pt working electrode [17] (note that the first ECL wave at ~ 0.9 V via the oxidative-reduction pathway are not clearly observed when a Pt working electrode is used). And so, the ECL image for 12 V indicates that luminophores contributing entire ECL emission depends on the position of the BPE, which reflects the applied potential. This interesting system provides the possibility to carry out a voltammetry-based ECL measurement by "one-shot" analysis with the same environmental conditions.

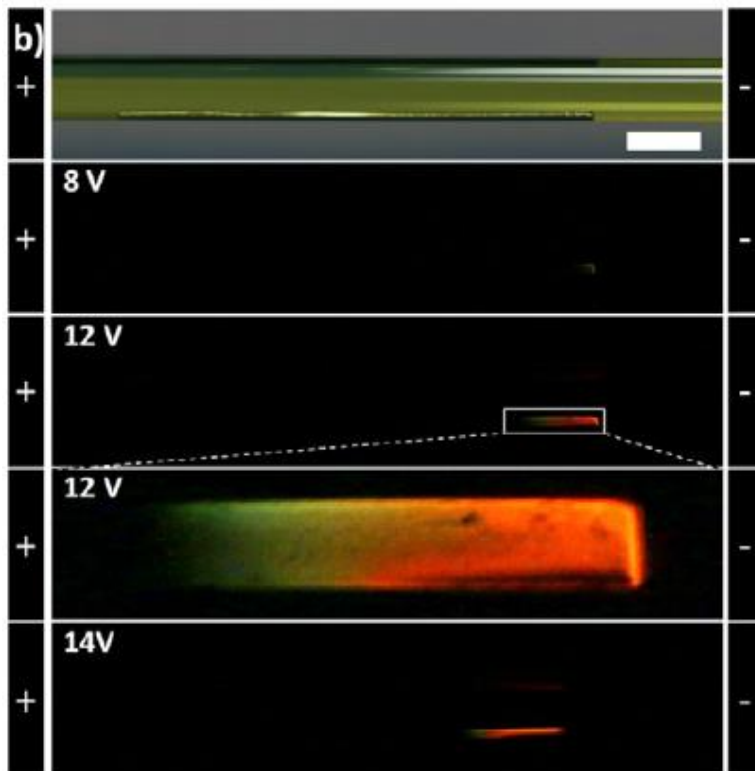


Figure 5.7 – Side-view of ECL emission at Pt wire in CH_3CN solution containing $\text{Ir}(\text{ppy})_3$, $\text{Ru}(\text{bpy})_3^{2+}$ and TPA under external potential application. At 12 V, an image with higher magnification is also shown in the figure. The scale bar in the upmost image (white) is 5 mm. Reprinted from [123] with permission. Copyright 2017 Elsevier B.V.

Figure 5.8 shows experimentally-obtained ECL intensity and electrical current as a function of applied potential for a Pt disk electrode (note: not BPE) under CH_3CN solution containing 10 mM TPA and either $\text{Ir}(\text{ppy})_3$ (green curve) or a mixture of $\text{Ir}(\text{ppy})_3$ and $\text{Ru}(\text{bpy})_3^{2+}$ (red curve). As previously discussed in detail in this thesis, ECL wave from $\text{Ir}(\text{ppy})_3$ shows a peak and then ECL quenches rapidly due to the quenching reaction of excited $\text{Ir}(\text{ppy})_3$ with TPA radical cation. On the other hand, ECL wave from a mixture

of Ir(ppy)₃ and Ru(bpy)₃²⁺ shows a peak at high potential compared to Ir(ppy)₃ due to high emission efficiency of Ru(bpy)₃²⁺ in a TPA-based ECL system.

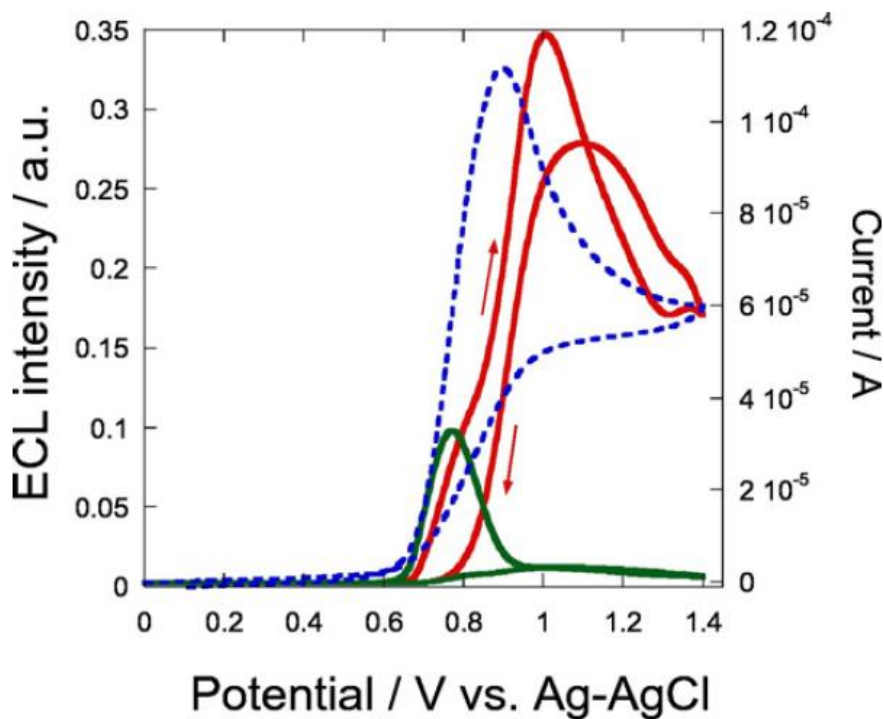


Figure 5.8 – Experimentally-obtained ECL intensity and electrical current as a function of applied potential for a Pt disk electrode under CH₃CN solution containing 10 mM TPA, 0.1 M TBAPF₆ and either 0.5 mM Ir(ppy)₃ (green curve) or a mixture of 0.5 mM Ir(ppy)₃ and 0.05 mM Ru(bpy)₃²⁺ (red curve). Blue dashed line shows electrical current. Scan rate: 0.1 V/s. Reprinted from [123] with permission. Copyright 2017 Elsevier B.V.

In this study, the numerical modeling of this very new system was also carried out by combining the findings from the previous parts of this thesis. In particular, the ECL quenching mechanism for Ir(ppy)₃ (discussed in Part A) and modeling of a bipolar ECL system (discussed in this part) were carefully considered in this modeling.

2) Modeling conditions

Similar to the bipolar ECL system based on a conductive bead, both of 1D and 2D modeling were carried out for this new system. Modeling parameters such as oxidation potentials and rate constants were determined by the 1D modeling, and then the 2D modeling was performed to model the entire bipolar ECL system.

Geometry used for the 1D modeling was the same as that for the Ir(ppy)₃/TPA system, which was shown in this thesis. Table 5.2 summarizes the general and reaction parameters used in this modeling. Most parameters were firstly determined from knowledge and findings in previous parts of this thesis. Some parameter values were adjusted in the middle of the study based on the obtained results.

Table 5.2 – General and reaction parameters used in the modeling of ECL behavior for the spatially-resolved bipolar ECL system.

a) General parameters

Parameter/item	Value/material
pH of solution	0 (mainly CH ₃ CN)
Initial TPA concentration	10 mM
Initial Ir(ppy) ₃ concentration	0.5 mM
Initial Ru(bpy) ₃ ²⁺ concentration	0.05 mM
Diffusion coefficient for species	5 x 10 ⁻⁶ cm ² s ⁻¹
Potential scan profile (for 1D)	0.5 V s ⁻¹
Temperature	25 °C

Working electrode	Platinum
Reference electrode	Ag AgCl

b) Considered reactions and relevant parameters

#	Reaction	Constants	E° (vs. Ag AgCl)
1	$\text{TPA} \leftrightarrow \text{TPA}^\bullet + \text{e}^-$	$k_f^{\text{TPA}} = 0.1 \text{ cm s}^{-1}$	$E_{\text{TPA}}^\circ = 1.1 \text{ V}$
2	$\text{TPA}^{\bullet+} \rightarrow \text{TPA}^\bullet + \text{H}^+$	$k_f^{\text{rTPA}} = 3500 \text{ s}^{-1}$	-
3	$\text{TPA}^\bullet \leftrightarrow \text{P1} + \text{e}^-$	$k_f^{\text{d}} = 0.1 \text{ cm s}^{-1}$	$E_{\text{d}}^\circ = -2.1 \text{ V}$
4	$\text{Ir}(\text{ppy})_3 \leftrightarrow \text{Ir}(\text{ppy})_3^+ + \text{e}^-$	$k_{\text{Ir}}^{\text{o}} = 0.1 \text{ cm s}^{-1}$	$E_{\text{Ir}}^\circ = 0.9 \text{ V}$
5	$\text{TPA}^\bullet + \text{Ir}(\text{ppy})_3^+ \rightarrow \text{Ir}(\text{ppy})_3^* + \text{P1}$	$k_f^1 = 10^8 \text{ M}^{-1} \text{ s}^{-1}$	-
6	$\text{Ir}(\text{ppy})_3^* \rightarrow \text{Ir}(\text{ppy})_3 + \text{ECL} (\sim 520 \text{ nm})$	$k_f^{\text{IECL}} = 10^5 \text{ s}^{-1}$	-
7	$\text{TPA}^{\bullet+} + \text{Ir}(\text{ppy})_3^* \rightarrow \text{Ir}(\text{ppy})_3^+ + \text{P2}$	$k_f^2 = 10^{12} \text{ M}^{-1} \text{ s}^{-1}$	-
8	$\text{Ru}(\text{bpy})_3^{2+} \leftrightarrow \text{Ru}(\text{bpy})_3^{3+} + \text{e}^-$	$k_{\text{Ru}}^{\text{o}} = 0.01 \text{ cm s}^{-1}$	$E_{\text{Ru}}^\circ = 0.85 \text{ V}$
9	$\text{TPA}^\bullet + \text{Ru}(\text{bpy})_3^{3+} \rightarrow \text{Ru}(\text{bpy})_3^{2+*} + \text{P1}$	$k_f^1 = 10^7 \text{ M}^{-1} \text{ s}^{-1}$	-
10	$\text{Ru}(\text{bpy})_3^{2+*} \rightarrow \text{Ru}(\text{bpy})_3^{2+} + \text{ECL} (\sim 620 \text{ nm})$	$k_f^{\text{RECL}} = 10^{7.2} \text{ s}^{-1}$	-

c) Model for 2D calculation

Figure 5.9 shows the geometry and potential gradient used in the modeling of the spatially-resolved bipolar ECL system. Since this calculation is very complicated (10 reactions could happen in parallel all over the meshes), a very small electrode (length: 4 μm) compared to the experimental conditions (length: 3.2 cm) was used to reduce

calculation load as much as possible. Also, the number of the used meshes was also tried to be minimum during the study, and the final mesh geometry is shown in the figure. In calculations, potential was increased to the final value (as shown in the figure) in 0.01 second also to reduce the calculation load (calculation load increases when the final value was applied from the beginning). Calculations were performed only for an external potential of 12 V in this study.

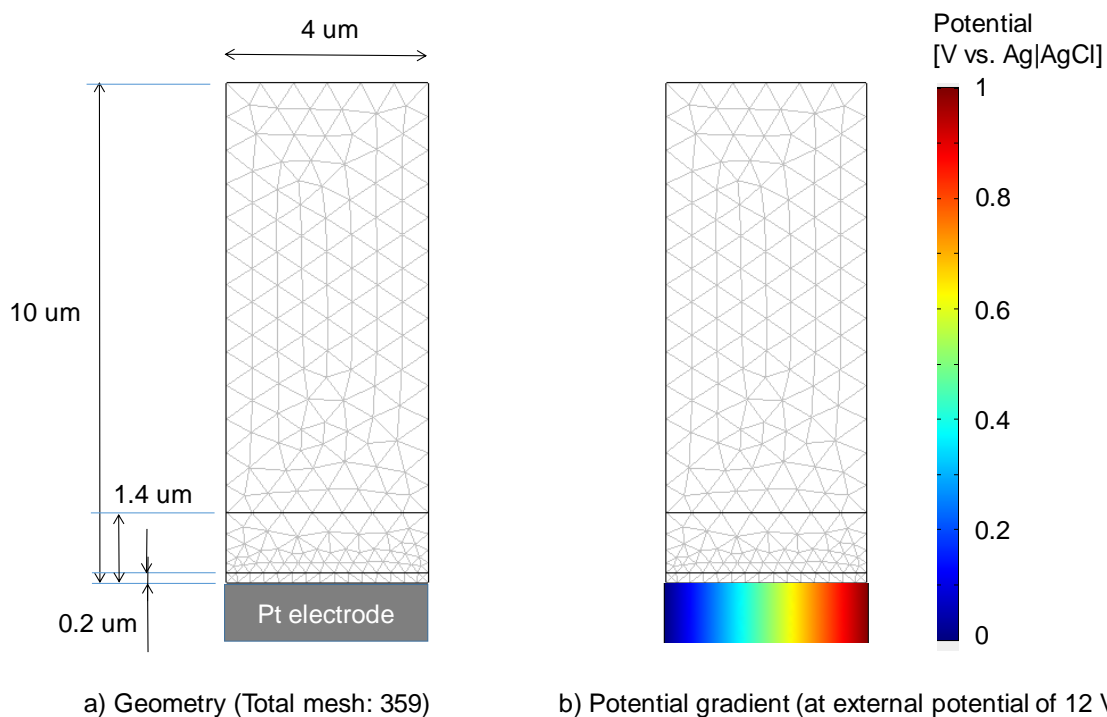


Figure 5.9 – Geometry and potential gradient used in the modeling of the spatially-resolved bipolar ECL system.

3) Results and discussion

Figure 5.10 shows calculated ECL intensity and electrical current as a function of applied potential for a Pt disk electrode (not BPE). Difference in ECL efficiency between

Ir(ppy)_3 and Ru(bpy)_3^{2+} was adjusted in the calculation considering the experimental data. When only Ir(ppy)_3 is used as a luminophore, ECL wave shows a peak at ~ 0.8 V and then ECL quenched at high potential. On the other hand, when Ru(bpy)_3^{2+} was added to the system, the second ECL wave due to the direct oxidation of Ru(bpy)_3^{2+} was observed at potentials of 0.8 V or higher, and the intensity of the second ECL wave was higher than the first ECL wave derived from Ir(ppy)_3 . These behaviors were very well in line with the experimental results (see Figure 5.8). Moreover, the behavior of calculated electrical current having its peak at ~ 0.9 V was also very similar to the experimental results. Analysis with the calculation results clarified that the electrical current behavior was mainly due to the oxidation current of TPA. These results indicated that appropriate parameters were determined for this system, and that the 2D calculation could be carried out using these parameters.

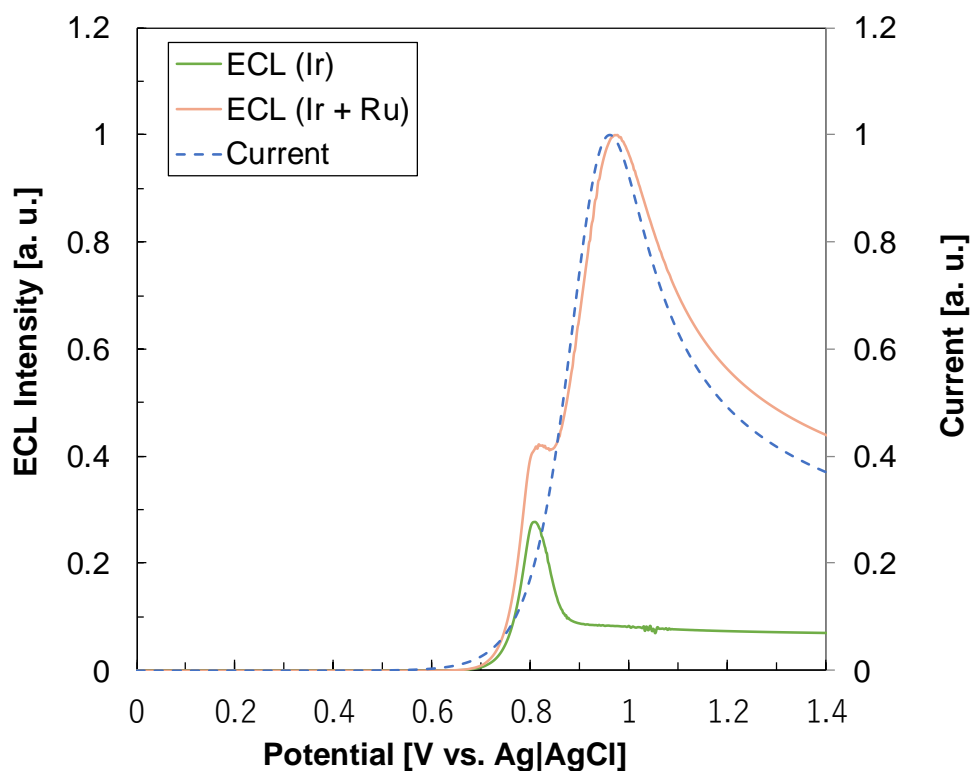


Figure 5.10 – Calculated ECL intensity and electrical current as a function of applied potential for a Pt disk electrode under CH_3CN solution containing 10 mM TPA and either 0.5 mM $\text{Ir}(\text{ppy})_3$ (green curve) or a mixture of 0.5 mM $\text{Ir}(\text{ppy})_3$ and 0.05 mM $\text{Ru}(\text{bpy})_3^{2+}$ (red curve). Blue dashed line shows electrical current. Scan rate: 0.5 V/s.

So, the 2D calculation to model the entire spatially-resolved multicolor ECL system was performed. Figure 5.11 shows calculated ECL intensity maps for $\text{Ir}(\text{ppy})_3$ and $\text{Ru}(\text{bpy})_3^{2+}$ at $t = 0.03$ second after potential application. ECL intensity becomes larger where the color becomes closer to red. For $\text{Ir}(\text{ppy})_3$, ECL was observed in the range of ~ 2 to 4 μm in the x-axis, and larger ECL intensity was observed at around $x = 3 \mu\text{m}$. The potential applied at $x = 3 \mu\text{m}$ is 0.75 V ($= 1 \text{ V} \times 3 \mu\text{m} / 4 \mu\text{m}$), and this is very well in line

with the fact that the ECL wave for Ir(ppy)₃ shows its peak at ~0.8 V. On the other hand, for Ru(bpy)₃²⁺, ECL was observed at around x = 4 μm, but not clearly observed at x = 3 μm or smaller. This is also in line with the fact that the ECL wave for Ru(bpy)₃²⁺ appears at ~0.8 V and the intensity increases up to ~1.0 V.

Moreover, the ECL intensity maps for Ir(ppy)₃ and Ru(bpy)₃²⁺ in this study showed that high ECL intensity area for Ir(ppy)₃ is more distant (y ≈ 1.4 μm) than that for Ru(bpy)₃²⁺ (y ≈ 0.2 μm). According to the calculation results in this study, this difference in the ECL behavior is derived from the rate constant for ECL emission from the excited state of a luminophore. The excited state of Ir(ppy)₃ has slower rate constant than Ru(bpy)₃²⁺. So, the excited state of Ir(ppy)₃ diffuses in longer distance before emitting ECL. These results indicated that numerical modeling can be also used for this kind of very detailed analysis. For example, more precise reaction parameter determination could be possible by numerical modeling with the combination of spatial ECL intensity analysis by optical observation.

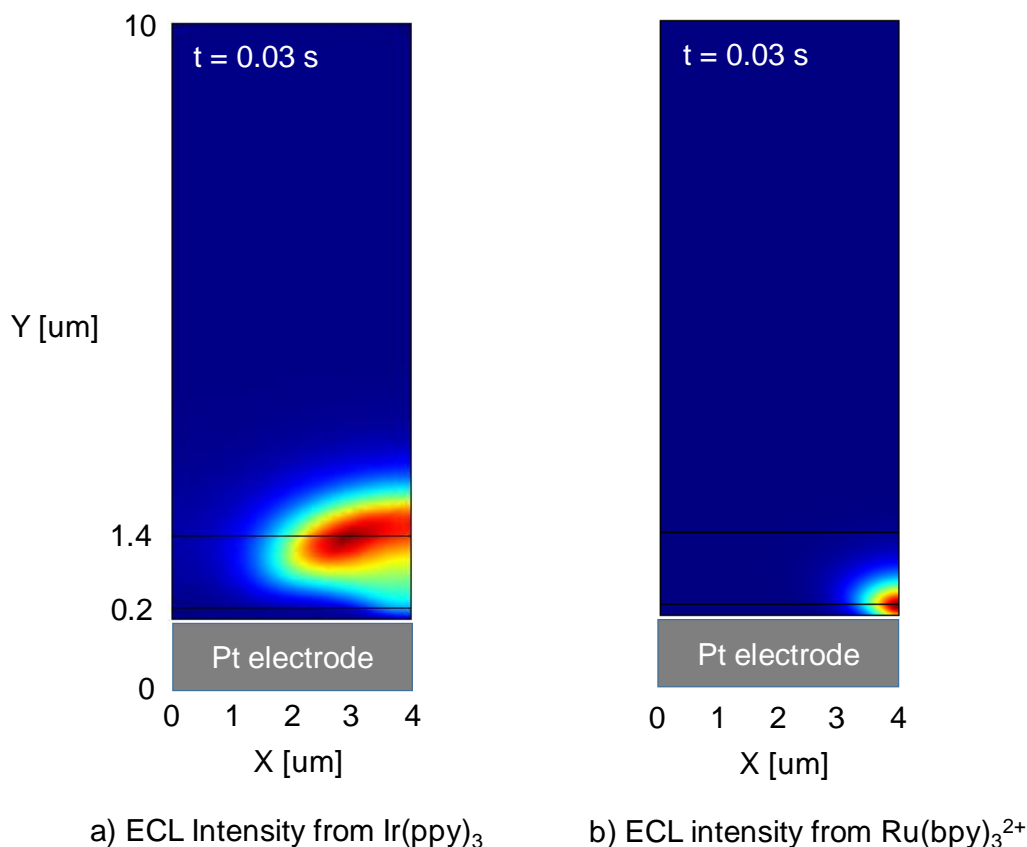


Figure 5.11 – Calculated ECL intensity maps for Ir(ppy)₃ and Ru(bpy)₃²⁺ at t = 0.03 second after potential application. ECL intensity becomes larger where the color is closer to red.

Finally, Figure 5.12 shows calculated normalized ECL intensity for Ir(ppy)₃ and Ru(bpy)₃²⁺ as a function of position at Pt wire surface (x direction). As discussed using the calculated ECL intensity maps (Figure 5.11), ECL intensity from Ir(ppy)₃ showed a peak at ~3 μm, corresponding to an applied potential of ~0.75 V. On the other hand, ECL intensity from Ru(bpy)₃²⁺ showed the maximum value at 4 μm, corresponding to an applied potential of 1.0 V. From these results, it is indicated that multicolor ECL that changes from green to orange is observed along the direction of the potential gradient,

and the numerical modeling in this study successfully reproduced the observation results in the experiment.

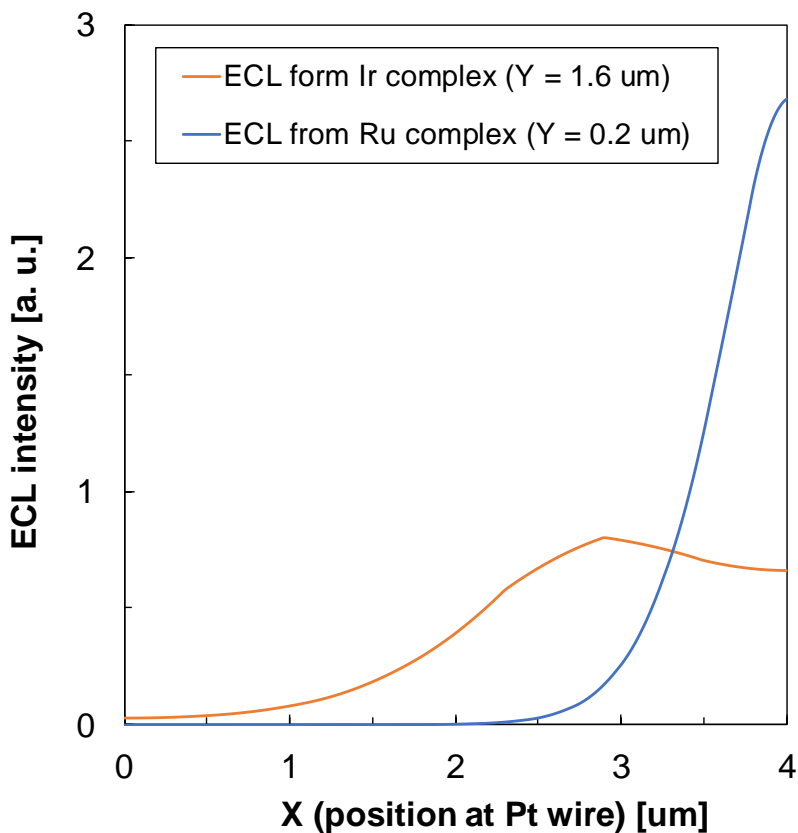


Figure 5.12 – Calculated normalized ECL intensity for $\text{Ir}(\text{ppy})_3$ and $\text{Ru}(\text{bpy})_3^{2+}$ as a function of position at Pt wire surface (x axis in the model). The highest intensity lines in y axis in the model, which can be seen in Figure 5.11, were used to analyze this ECL behavior ($y = 1.6 \text{ um}$ for $\text{Ir}(\text{ppy})_3$; $y = 0.2 \text{ um}$ for $\text{Ru}(\text{bpy})_3^{2+}$)

6. Conclusions

Three kinds of recently-proposed co-reactant ECL systems were numerically modeled in this study to analyze the reaction mechanism for ECL generation.

In Part A, a homogeneous ECL system based on solution containing Ir(ppy)₃ and tripropylamine (TPA), which shows interesting ECL quenching at high potential, was firstly analyzed. The numerical modeling in this study verified a mechanism that the excited state of Ir(ppy)₃ is quenched by its reaction with TPA radical cation, which is generated by the electrochemical oxidation of TPA. Moreover, a multicolor ECL system with the addition of another metal chelate was also modeled in this part, and then a 3D emission map on ECL intensity versus emission wavelength and applied potential was successfully reproduced.

In Part B, heterogeneous ECL from a Ru(bpy)₃²⁺-doped silica nanoparticle under solution containing TPA, which was reported as a very efficient ECL system, was analyzed. The numerical modeling in this study proposed that the surface state of the used working electrode changes during potential application, and then that causes the significant reduction of ECL intensity. Also, the numerical modeling verified a mechanism that the electron hopping inside the nanoparticle contributes to the efficient ECL for this system.

In Part C, a new ECL system based on bipolar electrochemistry was analyzed. The numerical modeling in this study successfully simulated the ECL behavior for this new ECL system, and then verified a mechanism that ECL quenches in specific area due to the

change in local pH during potential application. Moreover, a spatially-resolved bipolar ECL system, which was reported very recently, was also modeled in this part. The experimental results were well reproduced utilizing the findings from the other parts of this thesis.

In conclusion, the numerical modeling in this study contributed to the better understanding of the reaction mechanism, which can support further improvement of co-reactant ECL systems. Analysis for the reaction mechanism for ECL generation from theoretical viewpoint should be adequately considered in future experimental studies.

7. List of Publication

Papers:

- 1) K. Imai, G. Valenti, E. Villani, S. Rapino, E. Rampazzo, M. Marcaccio, L. Prodi and F. Paolucci, “Numerical Simulation of Doped Silica Nanoparticle Electrochemiluminescence”, *J. Phys. Chem. C*, vol. 119, no. 46, pp. 26111-8, 2015.
- 2) K. Imai, G. Valenti, E. Villani, A. Fiorani, M. Marcaccio, C. F. Hogan and F. Paolucci, “Numerical Modeling of Multicolor Co-Reactant ECL from Solution Containing Ir(III)-Based Luminophores”, under preparation.
- 3) K. Imai, G. Valenti, E. Villani, A. Fiorani, M. Marcaccio, N. Sojic and F. Paolucci, “Numerical modeling of Co-Reactant ECL Induced by Bipolar Electrochemistry”, under preparation.

Presentations:

- 1) K. Imai, G. Valenti, E. Villani, M. Marcaccio, L. Prodi and F. Paolucci, “ECL Simulation for a Ru-Doped Silica Nanoparticle Considering Electrode Surface Change during Potential Application”, a poster presentation in ECL’2014 - International Meeting on Electrogenerated Chemiluminescence, Poster P9 (September 2014 in Bertinoro, Italy).
- 2) K. Imai, G. Valenti, E. Villani, M. Marcaccio, L. Prodi and F. Paolucci, “Effect of Electrode Surface-State Change on Electrogenerated Chemiluminescence from a Ruthenium-Doped Silica Nanoparticle”, an oral presentation in the 66th Annual Meeting of the International Society of Electrochemistry, Symposium 14 (October 2015 in Taipei, Taiwan).

8. Supplemental Information: Models and Parameters

Representative numerical models and parameters used in this study are summarized in this chapter as supplemental information. All the values used in calculations are shown in SI units. Note that some parameters were adjusted during the study according to the purpose of the calculation.

8.1. Part A

1) Constants

Name	Value	Description
alpha	0.5	Transfer coefficient
F	96485	Faraday constant
R	8.314	Gas constant
T	298.15	Room temperature
n	1	Electron number
fa	38.94	F/RT
k0TPA	1e-3	Standard rate constant for TPA oxidation
E0TPA	0.50	Formal potential for TPA oxidation
kfrTPA	3500	Forward rate constant for deprotonation of TPA radical cation
kfI1	100000	Forward rate constant for P1 generation
kfI2	10 ^{9.2}	Forward rate constant for excited Ir quench
kfIECL	1e5	Forward rate constant for ECL generation
k0Ir0	1e-3	Standard rate constant for Ir oxidation
E0Ir0	0.35	Formal potential for Ir oxidation
cH	0	Hydrogen concentration
D	5e-10	General diffusion coefficient
DH	5e-9	Diffusion coefficient for H+
k0d	1e-3	Standard rate constant for TPA radical oxidation
E0d	-2.1	Formal potential for TPA radical oxidation
cIr0	0.11	Ir concentration
cTPA	25	TPA concentration

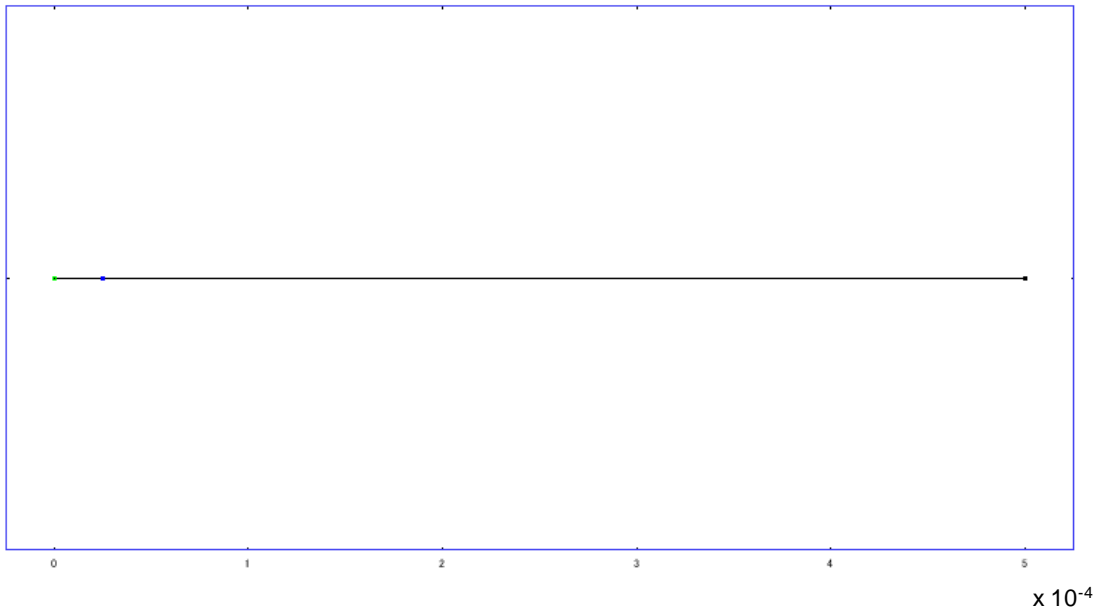
k0Ru2	1e-4	Standard rate constant for second luminophore oxidation
E0Ru2	0.7	Formal potential for second luminophore oxidation
kfR1	1e7	Forward rate constant for P1 generation for second luminophore
kfRECL	10 ⁵	Forward rate constant for ECL generation for second luminophore
cRu0	0.14	Second luminophore concentration

2) Global expressions

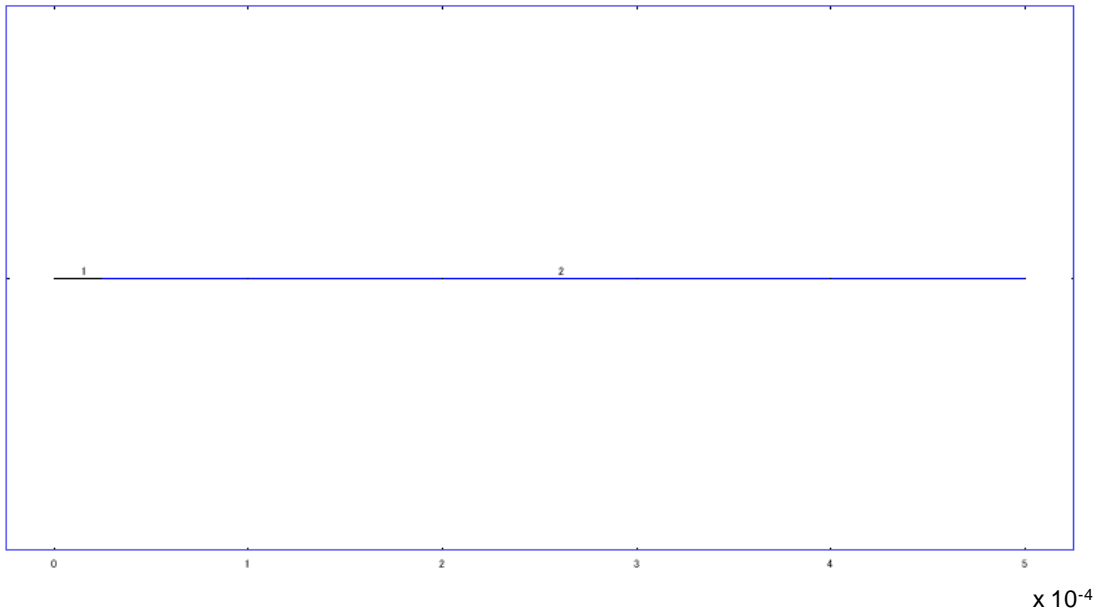
Name	Expression	Description
kfTPA	$k0TPA * \exp((1-\alpha) * n * fa * (E-E0TPA))$	forward rate constant for TPA oxidation
kbTPA	$k0TPA * \exp((-1 * \alpha) * n * fa * (E-E0TPA))$	backward rate constant for TPA oxidation
kfIr0	$k0Ir0 * \exp((1-\alpha) * n * fa * (E-E0Ir0))$	forward rate constant for Ir0 oxidation
kbIr0	$k0Ir0 * \exp((-1 * \alpha) * n * fa * (E-E0Ir0))$	backward rate constant for Ir0 oxidation
E	-0.5+t*0.5	applied voltage - scan
kfd	$k0d * \exp((1-\alpha) * n * fa * (E-E0d))$	forward rate constant for rTPA deprotonation
kbd	$k0d * \exp((-1 * \alpha) * n * fa * (E-E0d))$	backward rate constant for rTPA deprotonation
cd	$(ndflux_e_chdi + ndflux_P1_chdi) * F * -1$	current density
light	$kfIECL * Ire + kfRECL * P4 * 2$	ECL emission
kfRu2	$k0Ru2 * \exp((1-\alpha) * n * fa * (E-E0Ru2))$	forward rate constant for second luminophore oxidation
kbRu2	$k0Ru2 * \exp((-1 * \alpha) * n * fa * (E-E0Ru2))$	backward rate constant for second luminophore oxidation
light2	$kfRECL * P4$	ECL emission for second luminophore
light1	$kfIECL * Ire$	ECL emission for Ir0

3) Geometry

- Boundary mode



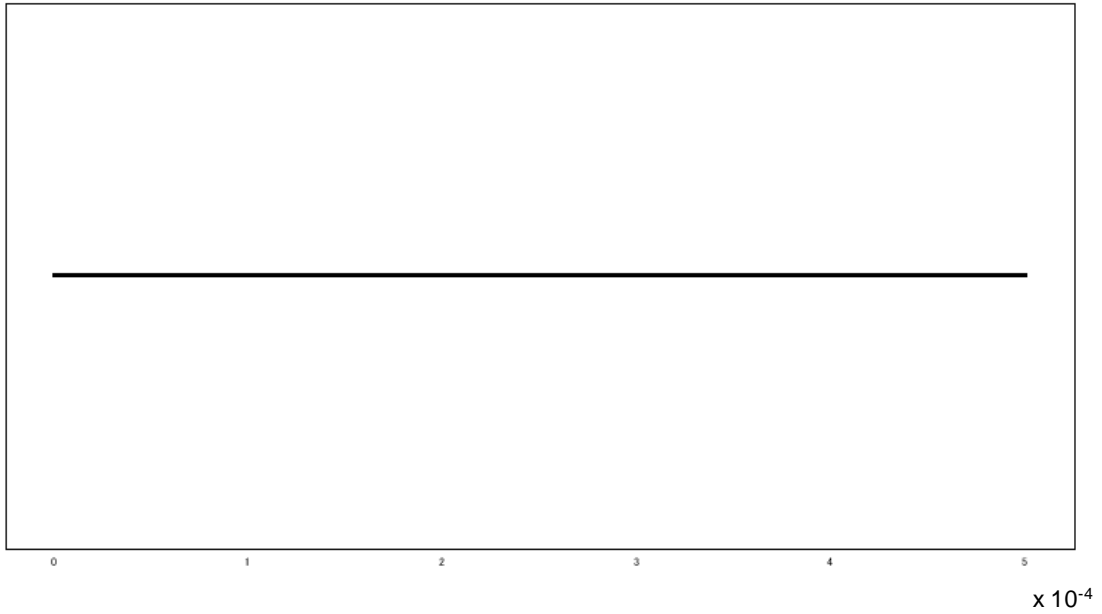
- Subdomain mode



4) Mesh statistics

Number of degrees of freedom	16400
Number of mesh points	513
Number of elements	512
Number of boundary elements	3

Element length ratio	0.776
----------------------	-------



5) Application mode properties

Application mode type: Diffusion (Chemical Engineering Module)

Application mode name: chdi

Property	Value
Default element type	Lagrange - Quadratic
Analysis type	Transient
Equilibrium assumption	Off
Frame	Frame (ref)
Weak constraints	Off
Constraint type	Ideal

6) Variables

Dependent variables: TPA, rcTPA, rTPA, e, H, P1, Ir0, Ir1, Ire, P2, ECL, P3, P4, Ru1, Ru2, Ru3

Shape functions: shlag(2,'TPA'), shlag(2,'rcTPA'), shlag(2,'rTPA'), shlag(2,'e'),
shlag(2,'H'), shlag(2,'P1'), shlag(2,'Ir0'), shlag(2,'Ir1'), shlag(2,'Ire'), shlag(2,'P2'),
shlag(2,'ECL'), shlag(2,'P3'), shlag(2,'P4'), shlag(2,'Ru1'), shlag(2,'Ru2'), shlag(2,'Ru3')

Interior boundaries not active

7) Boundary settings

Point	3
Inward flux (N)	{0;0;0;0;0;0;0;0;0;0;0;0;0;0;0}
type	{N0;N0;N0;N0;N0;N0;N0;N0;N0;N0;N0;N0;N0;N0;N0}
Point	2
Inward flux (N)	{0;0;0;0;0;0;0;0;0;0;0;0;0;0;0}
type	{cont;cont;cont;cont;cont;cont;cont;cont;cont;cont;cont;cont;cont;cont;cont;cont;cont;cont}
Point	1
Inward flux (N)	{-kfTPA*TPA;kfTPA*TPA;-kfd*rTPA;0;0;kfd*rTPA;-kfIr0*Ir0+kbIr0*Ir1;kfIr0*Ir0-kbIr0*Ir1;0;0;0;0;0;0;-kfRu2*Ru2+kbRu2*Ru3;kfRu2*Ru2-kbRu2*Ru3}
type	{N;N;N;N0;N0;N;N;N;N0;N0;N0;N0;N0;N;N;N}

8) Subdomain settings

Subdomain	1
Diffusion coefficient (D)	{D;D;D;D;DH;D;D;D;D;D;D;D;D;D;D;D}
Reaction rate (R)	{0;-kfrTPA*rcTPA-kfI2*Ire*rcTPA;kfrTPA*rcTPA-kfI1*Ir1*rTPA-kfR3*Ru3*rTPA;0;0;0;kfIECL*Ire;-kfI1*Ir1*rTPA+kfI2*Ire*rcTPA;kfI1*Ir1*rTPA-kfIECL*Ire-kfI2*Ire*rcTPA;kfI1*Ir1*rTPA;kfIECL*Ire+kfRECL*P4;kfI2*Ire*rcTPA;-kfRECL*P4+kfR3*Ru3*rTPA;0;kfRECL*P4;-kfR3*Ru3*rTPA}
Subdomain	2
Diffusion coefficient (D)	{D;D;D;D;DH;D;D;D;D;D;D;D;D;D;D;D}
Reaction rate (R)	{0;-kfrTPA*rcTPA;kfrTPA*rcTPA-kfI1*Ir1*rTPA-kfR3*Ru3*rTPA;0;0;0;kfIECL*Ire;-kfI1*Ir1*rTPA;kfI1*Ir1*rTPA-kfIECL*Ire-kfI2*Ire*rcTPA;kfI1*Ir1*rTPA;kfIECL*Ire+kfRECL*P4;kfI2*Ire*rcTPA;-kfRECL*P4+kfR3*Ru3*rTPA;0;kfRECL*P4;-kfR3*Ru3*rTPA}

Subdomain initial value	1	2
Concentration, TPA (TPA)	cTPA	cTPA
Concentration, Ir0 (Ir0)	cIr0	cIr0
Concentration, Ru2 (Ru2)	cRu0	cRu0

9) Solver settings

- General

Analysis type	Transient
Auto select solver	On
Solver	Time dependent
Solution form	Automatic
Symmetric	auto
Adaptive mesh refinement	Off
Optimization/Sensitivity	Off
Plot while solving	Off

- Direct (UMFPACK)

Solver type: Linear system solver

Parameter	Value
Pivot threshold	0.1
Memory allocation factor	0.7

- Time stepping

Parameter	Value
Times	range(0,0.01,3.2)
Relative tolerance	0.000001
Absolute tolerance	0.0000010
Times to store in output	Specified times
Time steps taken by solver	Free
Maximum BDF order	5
Singular mass matrix	Maybe
Consistent initialization of DAE systems	Backward Euler
Error estimation strategy	Include algebraic

Allow complex numbers	Off
-----------------------	-----

8.2. Part B

1) Constants

Name	Value	Description
alpha	0.5	Transfer coefficient
F	96485	Faraday constant
R	8.314	Gas constant
T	298.15	Room temperature
n	1	Electron number
fa	38.94	F/RT
Ka	10 ^{-10.4}	Acid dissociation constant for TPAH ⁺
k0TPA	1e-1	Standard rate constant for TPA oxidation
E0TPA	0.88	Formal potential for TPA oxidation
kbrTPA	1080	Backward rate constant for deprotonation of TPA radical cation
kf1	1e7	Forward rate constant for P1 generation
kf2	1e3	Forward rate constant for excited Ru2 generation from Ru ⁺
kfECL	10 ^(7.2)	Forward rate constant for ECL generation
k0Ru2	0.01	Standard rate constant for Ru2 ⁺ oxidation
E0Ru2	1.16	Formal potential for Ru2 ⁺ oxidation
k0Ru1	0.01	Standard rate constant for Ru ⁺ oxidation
E0Ru1	-1.48	Formal potential for Ru ⁺ oxidation
kf3	1e6	Forward rate constant for excited Ru2 generation from Ru ⁺³
khydrol	1e7	Rate constant for P2 generation
D	5e-10	General diffusion coefficient
DH	5e-9	Diffusion coefficient for H ⁺
DP	5e-10	Diffusion coefficient for P1 or P2
DB	5e-11	Diffusion coefficient inside bead
k0d	1e-1	Standard rate constant for TPA radical deprotonation
E0d	-1.7	Formal potential for TPA radical deprotonation
Deh	5e-11	Diffusion coefficient for electron hopping
cRu	353	Ru concentration in bead
cTPA	30	TPA concentration in solution
kfb	4e6	Forward rate constant for phosphate buffer
kbb	1e14	Backward rate constant for phosphate buffer

kf4	1e-3	Forward rate constant for reaction between Ru ³⁺ and TPA
-----	------	---

2) Global expressions

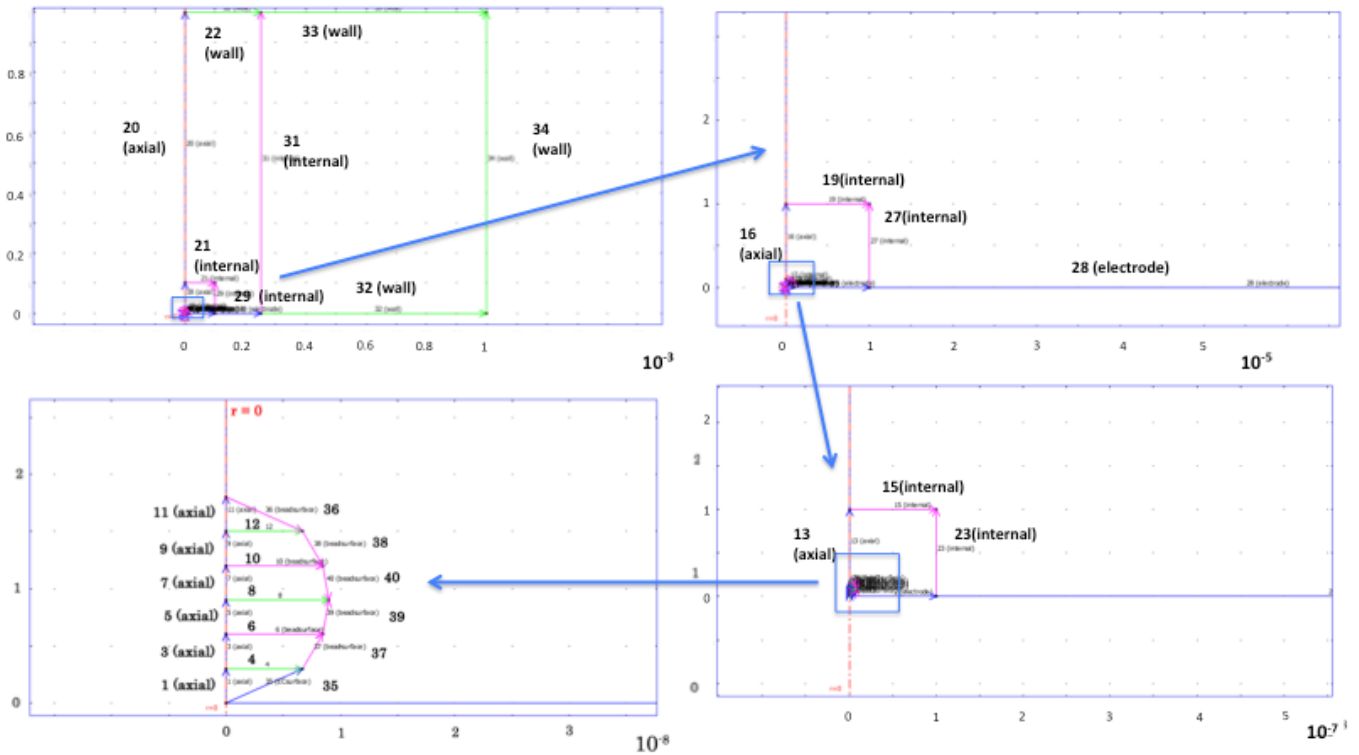
Name	Expression	Description
kfTPA	$k_0\text{TPA} \cdot \exp((1-\alpha) \cdot n \cdot f_a \cdot (E - E_0\text{TPA}))$	Forward rate constant for TPA oxidation
kbTPA	$k_0\text{TPA} \cdot \exp((-1 \cdot \alpha) \cdot n \cdot f_a \cdot (E - E_0\text{TPA}))$	Backward rate constant for TPA oxidation
kfRu2	$k_0\text{Ru2} \cdot \exp((1-\alpha) \cdot n \cdot f_a \cdot (E - E_0\text{Ru2}))$	Forward rate constant for Ru ²⁺ oxidation
kbRu2	$k_0\text{Ru2} \cdot \exp((-1 \cdot \alpha) \cdot n \cdot f_a \cdot (E - E_0\text{Ru2}))$	Backward rate constant for Ru ²⁺ oxidation
kfRu1	$k_0\text{Ru1} \cdot \exp((1-\alpha) \cdot n \cdot f_a \cdot (E - E_0\text{Ru1}))$	Forward rate constant for Ru ⁺ oxidation
kbRu1	$k_0\text{Ru1} \cdot \exp((-1 \cdot \alpha) \cdot n \cdot f_a \cdot (E - E_0\text{Ru1}))$	Backward rate constant for Ru ⁺ oxidation
E	$0 + t \cdot 0.5$	Applied potential
kfd	$k_0d \cdot \exp((1-\alpha) \cdot n \cdot f_a \cdot (E - E_0d))$	Forward rate constant for TPA radical deprotonation
kbd	$k_0d \cdot \exp((-1 \cdot \alpha) \cdot n \cdot f_a \cdot (E - E_0d))$	Backward rate constant for TPA radical deprotonation
cd	$(\text{ndflux_elec_chdi} + \text{ndflux_P1_chdi}) \cdot F^{-1}$	Current density
light	$k_f\text{ECL} \cdot \text{Ru2e}$	ECL emission
kfrTPA	$k_{\text{dep}}(t)$	Forward rate constant for TPA radical cation deprotonation

3) Geometry

- Boundary mode

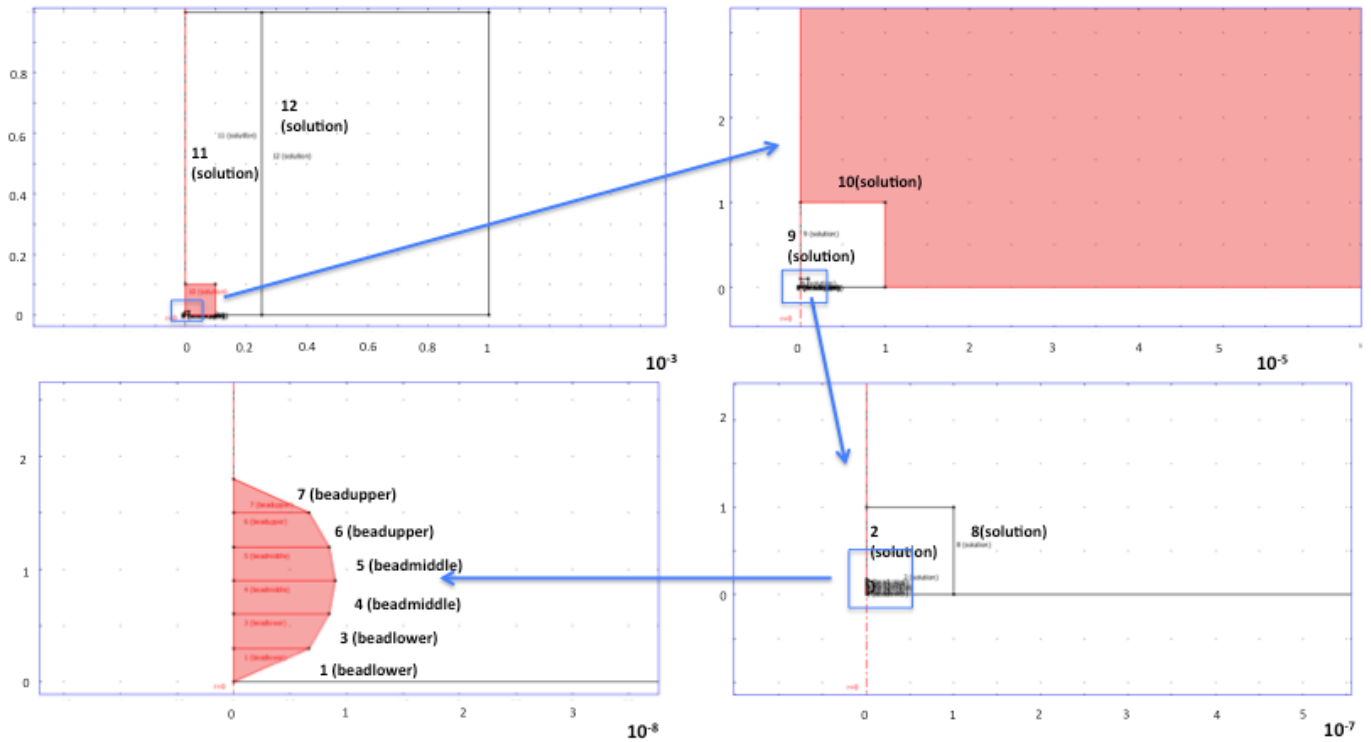
Calculations were performed considering only half of the electrode section, the other half being symmetric. Segments 2, 24, 26, 28, 30 identify the active regions (working Au electrode) of the electrode; segments 22, 32-34 represent the electrode insulating sheath respectively, and were all treated as insulating and unreactive. Segments 4, 8, 12, 6, 10, 36-40 represent the bead surface and segment 35 represent the surface where the direct Ru

oxidation can occur. Finally segments 1, 3, 5, 7, 9, 11, 13-14, 16, 18, 20 were treated as a symmetry element. The depletion of the reductant species (TPA or TPA^{*}) was treated as a flux towards the electrode (segments 2, 24, 26, 28, 30) while product generation was treated as a flux in the opposite direction.



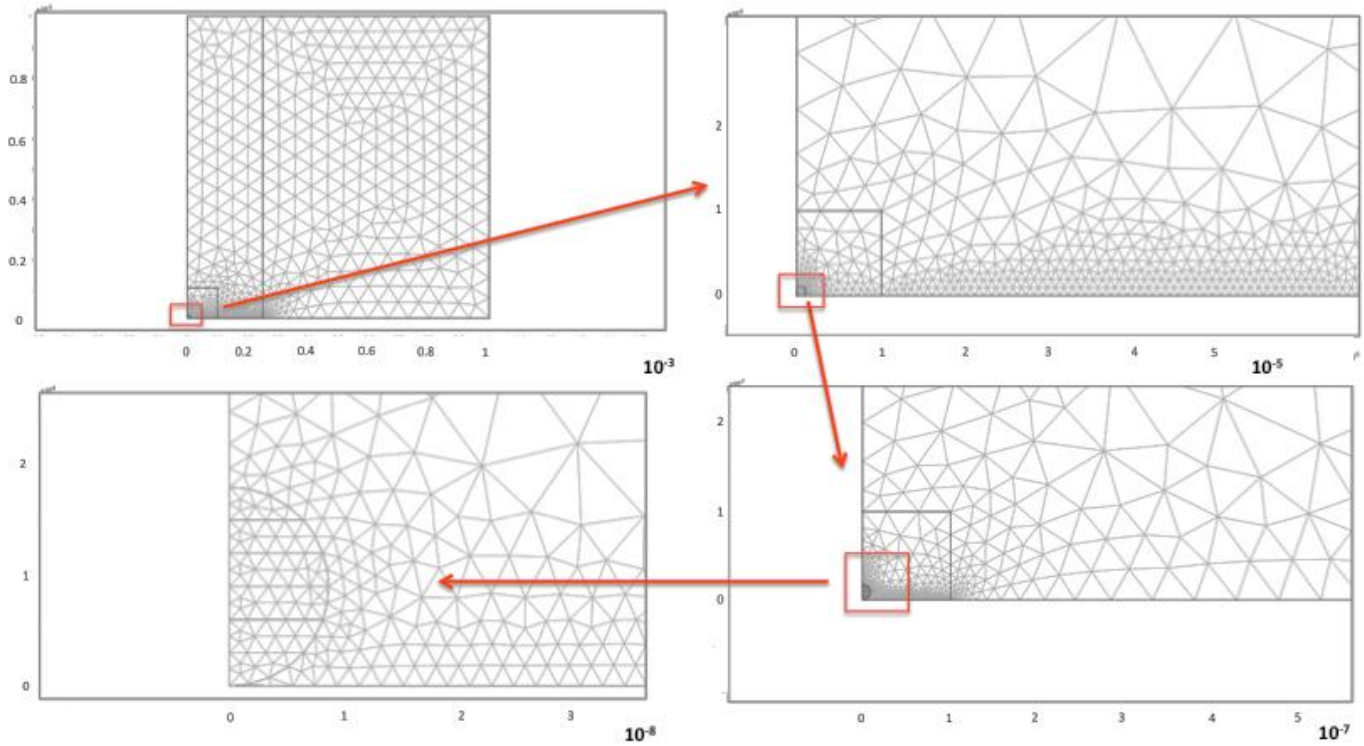
- Subdomain mode

Chemical reactions were introduced in the models in subdomain settings. Surfaces 1-7 identify the doped silica nanoparticles. This surface was divided in three different subdomains: 1,3 represent the lower part; 4, 5 represent the middle part and 6,7 the upper part of the DSNP. Finally subdomains 1,8-12 were treated as a bulk solution.



4) Mesh statistics

Number of degrees of freedom	139997
Number of mesh points	2807
Number of elements	5156
Triangular	5156
Quadrilateral	0
Number of boundary elements	567
Number of vertex elements	29
Minimum element quality	0.148
Element area ratio	0



5) Application mode properties

Application mode type: Diffusion (Chemical Engineering Module)

Application mode name: chdi

Property	Value
Default element type	Lagrange - Quadratic
Analysis type	Transient
Equilibrium assumption	Off
Frame	Frame (ref)
Weak constraints	Off
Constraint type	Ideal

6) Variables

Dependent variables: TPAH, TPA, H, elec, rcTPA, rTPA, Ru2, P1, Ru1, Ru2e, ECL, Ru3,

P2

Shape functions: shlag(2,'TPAH'), shlag(2,'TPA'), shlag(2,'H'), shlag(2,'elec'),
shlag(2,'rcTPA'), shlag(2,'rTPA'), shlag(2,'Ru2'), shlag(2,'P1'), shlag(2,'Ru1'),
shlag(2,'Ru2e'), shlag(2,'ECL'), shlag(2,'Ru3'), shlag(2,'P2')

Interior boundaries active

7) Boundary settings

Boundary	1, 3, 5, 7, 9, 11, 13-14, 16, 18, 20	2, 24, 26, 28, 30
Type	Axial symmetry	Insulation/Symmetry
Name	axial	electrode
Inward flux (N)	{0;0;0;0;0;0;0;0;0;0;0;0}	{0;-kfTPA*TPA;0;kfTPA*TPA;kfTPA*TPA;-kfd*rTPA;0;kfd*rTPA;0;0;0;0;0}

Boundary	4, 8, 12	6, 10, 36-40	15, 17, 19, 21, 23, 25, 27, 29, 31	22, 32-34
Type	Continuity	Continuity	Continuity	Insulation/Symmetry
Name		beadsurface	internal	wall
Inward flux (N)	{0;0;0;0;0;0;0;0;0;0;0;0}	{0;0;0;0;0;0;0;0;0;0;0;0}	{0;0;0;0;0;0;0;0;0;0;0;0}	{0;0;0;0;0;0;0;0;0;0;0;0}

Boundary	35
Type	Continuity
Name	ECsurface
Inward flux (N)	{0;0;0;0;0;0;kfRu1*Ru1-kbRu1*Ru2-kfRu2*Ru2+kbRu2*Ru3;0;-kfRu1*Ru1+kbRu1*Ru2;0;0;kfRu2*Ru2-kbRu2*Ru3;0}

8) Subdomain settings

Subdomain	1, 3
Name	beadlower
Diffusion coefficient (D)	{DB;DB;DH;DB;DB;DB;Deh;DB;Deh;0;0;Deh;DB}
Reaction rate (R)	{-kfb*TPAH+kbb*TPA*cH;kf2*rcTPA*Ru1+kfb*TPAH-kbb*TPA*cH;0;0;-kf2*rcTPA*Ru1-kfrTPA*rcTPA+kbrTPA*rTPA*cH;-kf1*rTPA*Ru2+kfrTPA*rcTPA-kbrTPA*rTPA*cH-kf3*rTPA*Ru3;-kf1}

	$*r_{TPA}Ru_2+kfECLRu_2e;kf1*r_{TPA}Ru_2+kf3*r_{TPA}Ru_3;kf1*r_{TPA}Ru_2-kf2*rc_{TPA}Ru_1;kf2*rc_{TPA}Ru_1-kfECLRu_2e+kf3*r_{TPA}Ru_3;kfECLRu_2e;-kf3*r_{TPA}Ru_3;0\}$
(relExpr)	$\{r_1 \text{ rxn}; 10000*rc_{TPA}-200000*r_{TPA}\}$

Subdomain	2, 8-12
Name	solution
Diffusion coefficient (D)	$\{DB;DB;DH;DB;DB;DB;0;DB;0;0;0;DB\}$
Reaction rate (R)	$\{-kfb*TPAH+kbb*TPA*cH;kfb*TPAH-kbb*TPA*cH;0;0;-kfr_{TPA}rc_{TPA}+kbr_{TPA}*r_{TPA}*cH;kfr_{TPA}*rc_{TPA}-kbr_{TPA}*r_{TPA}*cH;0;0;0;0;0\}$
(relExpr)	

Subdomain	4-5
Name	beadmiddle
Diffusion coefficient (D)	$\{D;D;DH;D;D;D;0;DP;0;0;0;DP\}$
Reaction rate (R)	$\{-kfb*TPAH+kbb*TPA*cH;kf2*rc_{TPA}Ru_1+kfb*TPAH-kbb*TPA*cH;0;0;-kf2*rc_{TPA}Ru_1-kfr_{TPA}rc_{TPA}+kbr_{TPA}*r_{TPA}*cH;-kf1*r_{TPA}Ru_2+kfr_{TPA}*rc_{TPA}-kbr_{TPA}*r_{TPA}*cH-kf3*r_{TPA}Ru_3;-kf1*r_{TPA}Ru_2+kfECLRu_2e;kf1*r_{TPA}Ru_2;kf1*r_{TPA}Ru_2-kf2*rc_{TPA}Ru_1;kf2*rc_{TPA}Ru_1-kfECLRu_2e+kf3*r_{TPA}Ru_3;kfECLRu_2e;-kf3*r_{TPA}Ru_3;0\}$
(relExpr)	$\{r_1 \text{ rxn}; 10000*rc_{TPA}-200000*r_{TPA}\}$

Subdomain	6-7
Name	beadupper
Diffusion coefficient (D)	$\{DB;DB;DH;DB;DB;DB;0;DB;0;0;0;DB\}$
Reaction rate (R)	$\{-kfb*TPAH+kbb*TPA*cH;kf2*rc_{TPA}Ru_1+kfb*TPAH-kbb*TPA*cH;0;0;-kf2*rc_{TPA}Ru_1-kfr_{TPA}rc_{TPA}+kbr_{TPA}*r_{TPA}*cH;-kf1*r_{TPA}Ru_2+kfr_{TPA}*rc_{TPA}-kbr_{TPA}*r_{TPA}*cH-kf3*r_{TPA}Ru_3;-kf1*r_{TPA}Ru_2+kfECLRu_2e;kf1*r_{TPA}Ru_2;kf1*r_{TPA}Ru_2-kf2*rc_{TPA}Ru_1;kf2*rc_{TPA}Ru_1-kfECLRu_2e+kf3*r_{TPA}Ru_3;kfECLRu_2e;-kf3*r_{TPA}Ru_3;0\}$
(relExpr)	$\{r_1 \text{ rxn}; 10000*rc_{TPA}-200000*r_{TPA}\}$

Subdomain initial value	1, 3	2, 8-12	4-5	6-7
Concentration, TPA (TPA)	cTPA	cTPA	cTPA	cTPA

Concentration, H (H)	cH	cH	cH	cH
Concentration, Ru2 (Ru2)	cRu	0	cRu	cRu

9) Interpolation functions

Interpolation Function: kdep

Interpolation method: Piecewise Cubic

Data source type: Table

x	f(x)
0	540
1.8	540
2.2	3500
3	3500

10) Solver settings

- General

Analysis type	Transient
Auto select solver	On
Solver	Time dependent
Solution form	Automatic
Symmetric	auto
Adaptive mesh refinement	Off
Optimization/Sensitivity	Off
Plot while solving	Off

- Direct (UMFPACK)

Solver type: Linear system solver

Parameter	Value
Pivot threshold	0.1
Memory allocation factor	0.7

- Time stepping

Parameter	Value
Times	range(0,0.01,3)
Relative tolerance	0.001
Absolute tolerance	0.0001
Times to store in output	Specified times
Time steps taken by solver	Free
Maximum BDF order	5
Singular mass matrix	Maybe
Consistent initialization of DAE systems	Backward Euler
Error estimation strategy	Include algebraic
Allow complex numbers	On

8.3. Part C (1D)

1) Constants

Name	Value	Description
alpha	0.5	Transfer coefficient
F	96485	Faraday constant
R	8.314	Gas constant
T	298.15	Room temperature
n	1	Electron number
fa	38.94	F/RT
k0NADH	1e-4	Standard rate constant for NADH oxidation
E0NADH	1.15	Formal potential for NADH oxidation
kfrNADH	1e4	Forward rate constant for deprotonation of NAD radical
kf1	1e7	Forward rate constant for P1 generation
kfECL	10 ^(7.2)	Forward rate constant for ECL generation
k0Ru2	1e-4	Standard rate constant for Ru2+ oxidation
E0Ru2	1.5	Formal potential for Ru2+ oxidation
k0d	1e-4	Standard rate constant for NAD radical deprotonation
E0d	-1.7	Formal potential for NAD radical deprotonation
k0H2O	1e-4	Standard rate constant for water oxidation
E0H2O	2.38	Formal potential for water oxidation
D	5e-10	general diffusion coefficient
DH	5e-9	diffusion coefficient for H+

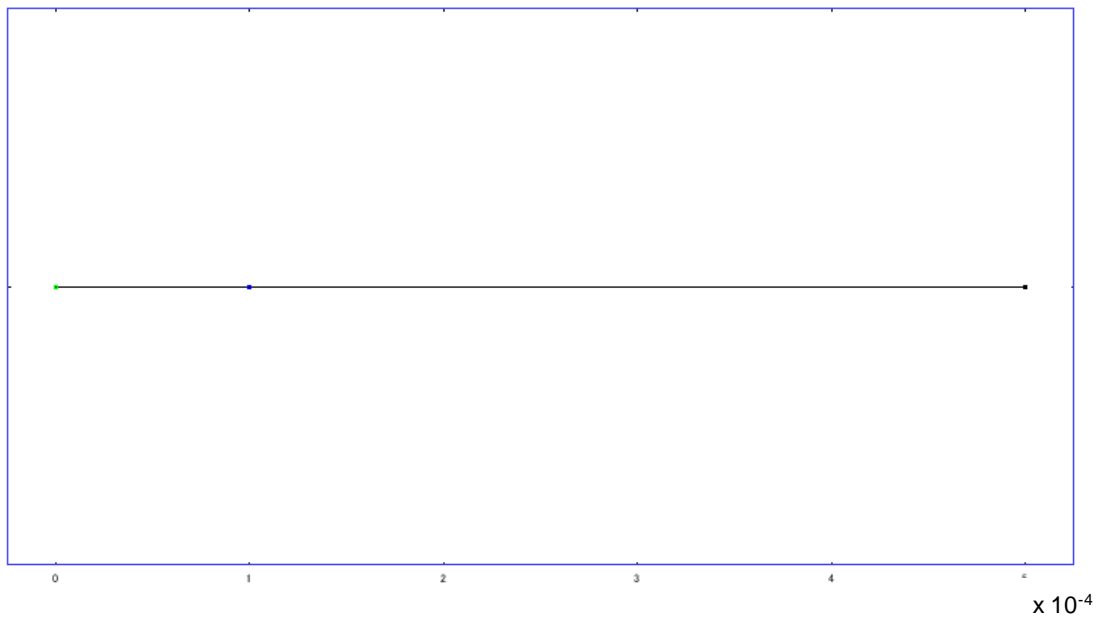
DP	5e-10	diffusion coefficient for P1 or P2
cRu	1.5	Ru concentration
cNADH	0.1	NADH concentration
kfb	4e6	Forward rate constant for phosphate buffer
kbb	1e11	Backward rate constant for phosphate buffer
cH2PO4	50	H2PO4 concentration
cH2O	55600	Water concentration
cHPO4	50	HPO4 concentration

2) Global expressions

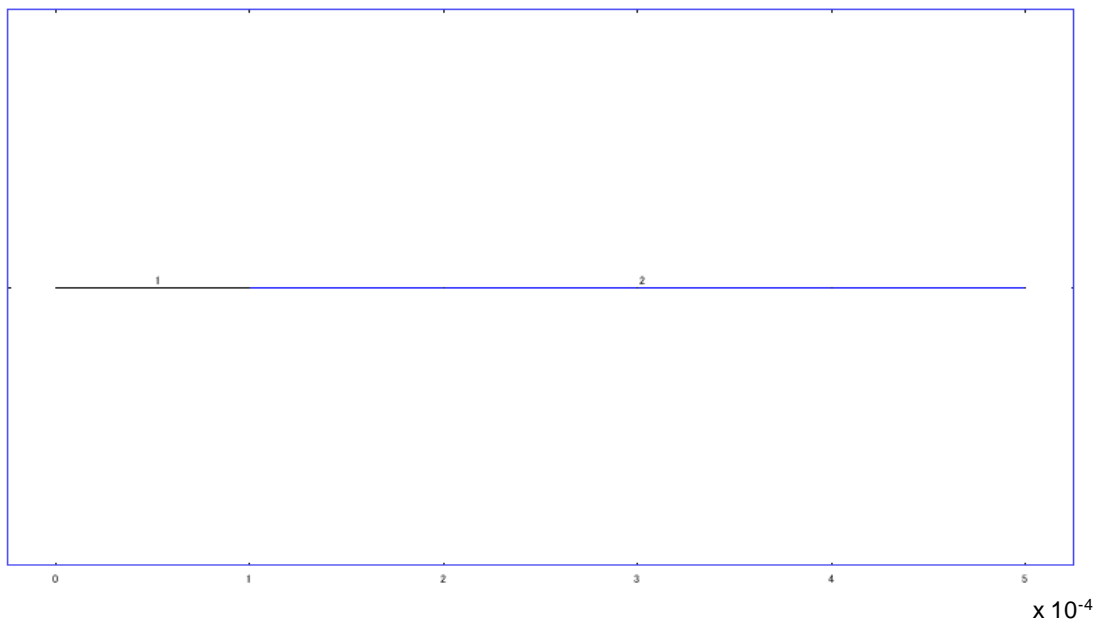
Name	Expression	Description
kfNADH	$k_0\text{NADH} \cdot \exp((1-\alpha) \cdot n \cdot f_a \cdot (E - E_0\text{NADH}))$	Forward rate constant for NADH oxidation
kbNADH	$k_0\text{NADH} \cdot \exp((-1 \cdot \alpha) \cdot n \cdot f_a \cdot (E - E_0\text{NADH}))$	Backward rate constant for NADH oxidation
kfRu2	$k_0\text{Ru2} \cdot \exp((1-\alpha) \cdot n \cdot f_a \cdot (E - E_0\text{Ru2}))$	Forward rate constant for Ru2+ oxidation
kbRu2	$k_0\text{Ru2} \cdot \exp((-1 \cdot \alpha) \cdot n \cdot f_a \cdot (E - E_0\text{Ru2}))$	Backward rate constant for Ru2+ oxidation
kfH2O	$k_0\text{H2O} \cdot \exp((1-\alpha) \cdot n \cdot f_a \cdot (E - E_0\text{H2O}))$	Forward rate constant for Ru+ oxidation
kbH2O	$k_0\text{H2O} \cdot \exp((-1 \cdot \alpha) \cdot n \cdot f_a \cdot (E - E_0\text{H2O}))$	Backward rate constant for Ru+ oxidation
E	$0 + t \cdot 1$	Applied potential
kfd	$k_0d \cdot \exp((1-\alpha) \cdot n \cdot f_a \cdot (E - E_0d))$	Forward rate constant for NAD radical deprotonation
kbd	$k_0d \cdot \exp((-1 \cdot \alpha) \cdot n \cdot f_a \cdot (E - E_0d))$	Backward rate constant for NAD radical deprotonation
cd	$(\text{ndflux_NADH_chdi} + \text{ndflux_Ru2_chdi} + \text{ndflux_H2O_chdi} \cdot 2) \cdot F$	Current density
light	$k_f\text{ECL} \cdot \text{Ru2e}$	ECL emission

3) Geometry

- Boundary mode



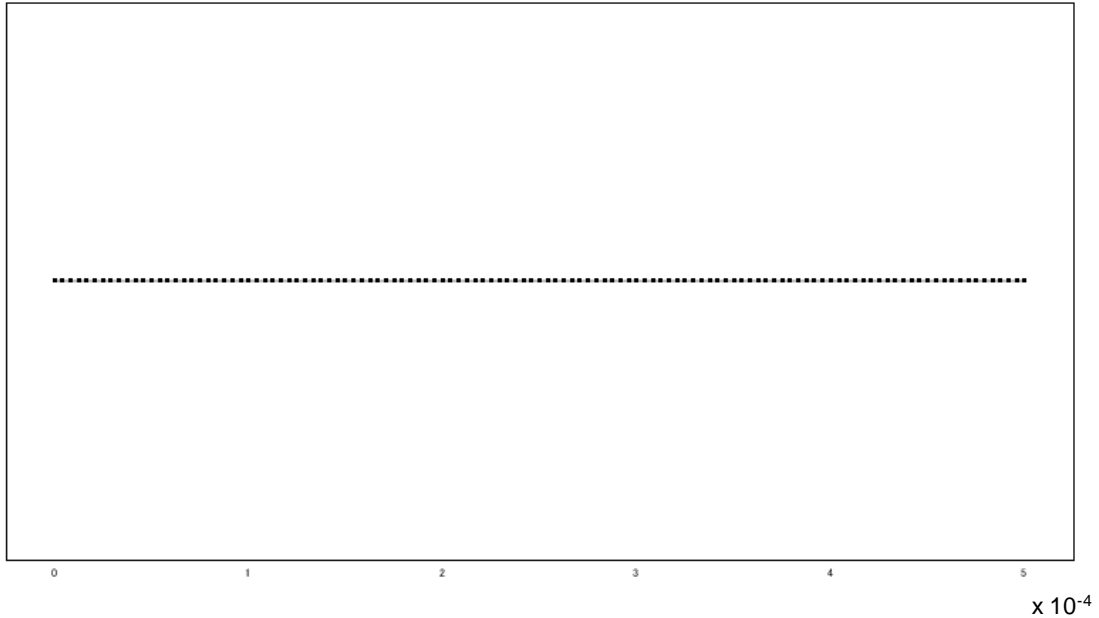
- Subdomain mode



4) Mesh statistics

Number of degrees of freedom	3856
------------------------------	------

Number of mesh points	121
Number of elements	120
Number of boundary elements	3
Element length ratio	1



5) Application mode properties

Application mode type: Diffusion (Chemical Engineering Module)

Application mode name: chdi

Property	Value
Default element type	Lagrange - Quadratic
Analysis type	Transient
Equilibrium assumption	Off
Frame	Frame (ref)
Weak constraints	Off
Constraint type	Ideal

6) Variables

	DH*rcNADH-kbrNADH*rNA D*H-kf3*Ru3*rNAD;kf3*Ru3 *rNAD;0;-kf3*Ru3*rNAD;kf3 *Ru3*rNAD-kfECL*Ru2e;kfE CL*Ru2e;0;0;0}	NADH-kbrNADH*rNAD*H;kf3 *Ru3*rNAD;0;0;0;0;0;0}
--	--	---

Subdomain initial value	1	2
Concentration, H2PO4 (H2PO4)	cH2PO4	cH2PO4
Concentration, HPO4 (HPO4)	cHPO4	cHPO4
Concentration, NADH (NADH)	cNADH	cNADH
Concentration, Ru2 (Ru2)	cRu	cRu
Concentration, H2O (H2O)	cH2O	cH2O

9) Solver settings

- General

Analysis type	Transient
Auto select solver	On
Solver	Time dependent
Solution form	Automatic
Symmetric	auto
Adaptive mesh refinement	Off
Optimization/Sensitivity	Off
Plot while solving	Off

- Direct (UMFPACK)

Solver type: Linear system solver

Parameter	Value
Pivot threshold	0.1
Memory allocation factor	0.7

- Time stepping

Parameter	Value
Times	range(0,0.01,2)
Relative tolerance	0.000001

Absolute tolerance	0.0000010
Times to store in output	Specified times
Time steps taken by solver	Free
Maximum BDF order	5
Singular mass matrix	Maybe
Consistent initialization of DAE systems	Backward Euler
Error estimation strategy	Include algebraic
Allow complex numbers	On

8.4. Part C (2D)

1) Constants

Name	Value	Description
alpha	0.5	Transfer coefficient
F	96485	Faraday constant
R	8.314	Gas constant
T	298.15	Room temperature
n	1	Electron number
fa	38.94	F/RT
k0NADH	1e-5	Standard rate constant for NADH oxidation
E0NADH	1.05	Formal potential for NADH oxidation
kfrNADH	1e4	Forward rate constant for deprotonation of NAD radical
kf1	1e7	Forward rate constant for P1 generation
kfECL	10 ^(7.2)	Forward rate constant for ECL generation
k0Ru2	0.01	Standard rate constant for Ru2+ oxidation
E0Ru2	1.55	Formal potential for Ru2+ oxidation
k0d	1e-4	Standard rate constant for NAD radical deprotonation
E0d	-1.7	Formal potential for NAD radical deprotonation
k0H2O	10 ⁽⁻¹¹⁾	Standard rate constant for water oxidation
E0H2O	1.55	Formal potential for water oxidation
D	5e-10	general diffusion coefficient
DH	5e-9	diffusion coefficient for H+
DP	5e-10	diffusion coefficient for P1 or P2
cRu	1.5	Ru concentration

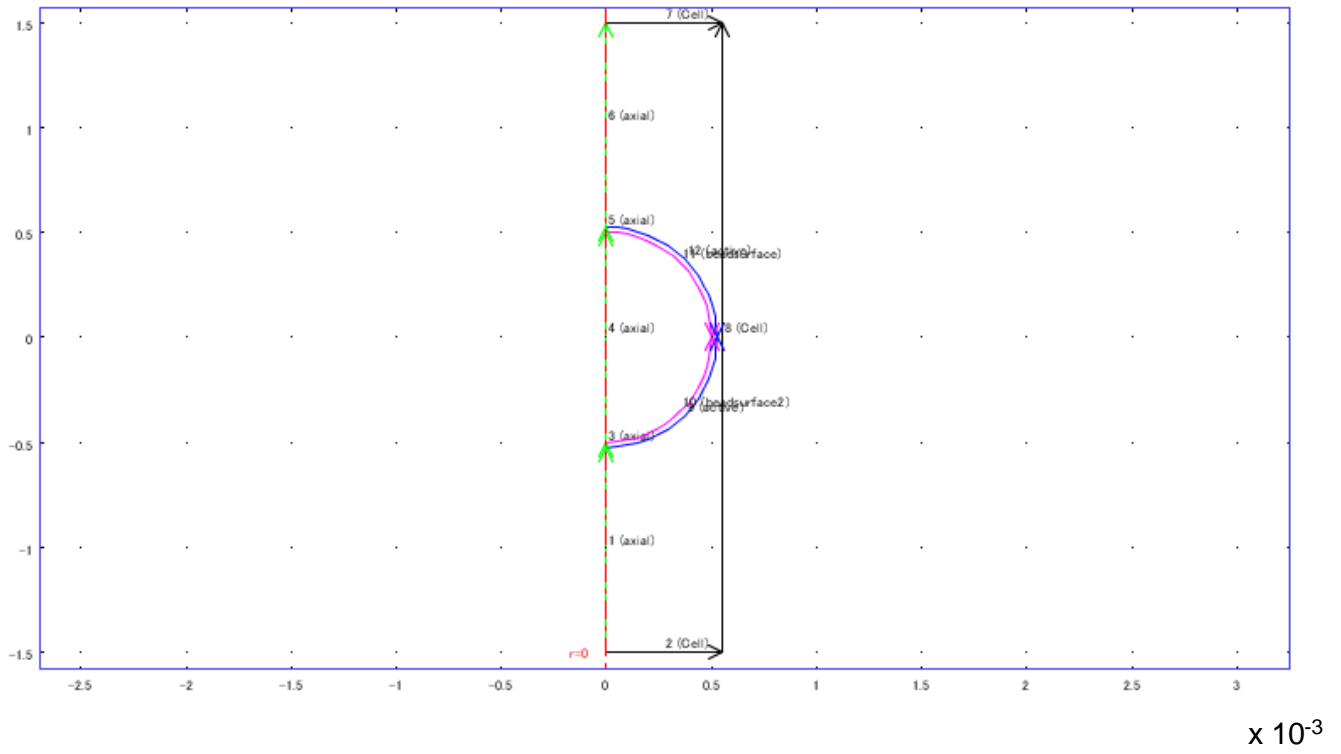
cNADH	0.2	NADH concentration
kfb	4e6	Forward rate constant for phosphate buffer
kbb	1e11	Backward rate constant for phosphate buffer
cH2PO4	50	H2PO4 concentration
cH2O	55600	Water concentration
cHPO4	50	HPO4 concentration

2) Global expressions

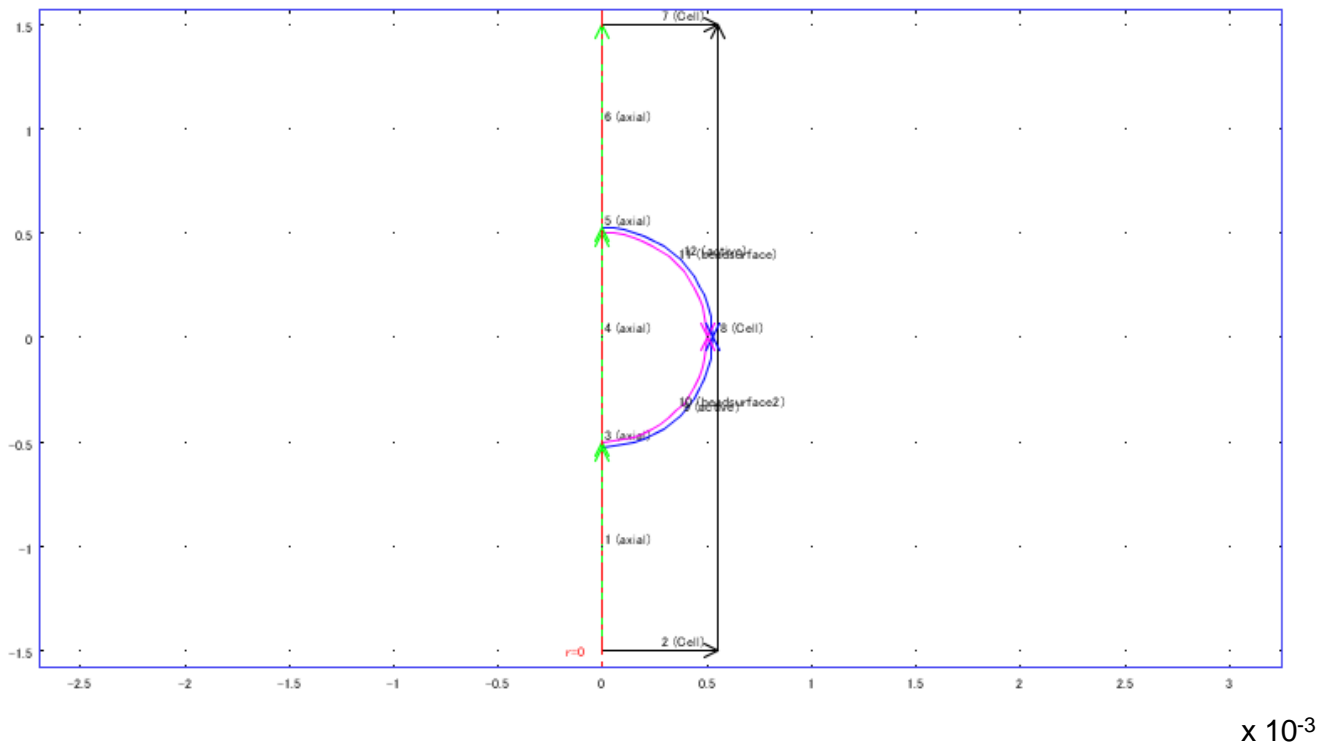
Name	Expression	Description
kfNADH	$k_0\text{NADH} \cdot \exp((1-\alpha) \cdot n \cdot f_a \cdot (E - E_0\text{NADH}))$	Forward rate constant for NADH oxidation
kbNADH	$k_0\text{NADH} \cdot \exp((-1 \cdot \alpha) \cdot n \cdot f_a \cdot (E - E_0\text{NADH}))$	Backward rate constant for NADH oxidation
kfRu2	$k_0\text{Ru2} \cdot \exp((1-\alpha) \cdot n \cdot f_a \cdot (E - E_0\text{Ru2}))$	Forward rate constant for Ru2+ oxidation
kbRu2	$k_0\text{Ru2} \cdot \exp((-1 \cdot \alpha) \cdot n \cdot f_a \cdot (E - E_0\text{Ru2}))$	Backward rate constant for Ru2+ oxidation
kfH2O	$k_0\text{H2O} \cdot \exp((1-\alpha) \cdot n \cdot f_a \cdot (E - E_0\text{H2O}))$	Forward rate constant for water oxidation
kbH2O	$k_0\text{H2O} \cdot \exp((-1 \cdot \alpha) \cdot n \cdot f_a \cdot (E - E_0\text{H2O}))$	Backward rate constant for water oxidation
kfd	$k_0d \cdot \exp((1-\alpha) \cdot n \cdot f_a \cdot (E - E_0d))$	forward rate constant for NADH radical deprotonation
kbd	$k_0d \cdot \exp((-1 \cdot \alpha) \cdot n \cdot f_a \cdot (E - E_0d))$	backward rate constant for NADH radical deprotonation
cd	$(\text{ndflux_NADH_chdi} + \text{ndflux_Ru2_chdi} + \text{ndflux_H2O_chdi} \cdot 2) \cdot F$	Current density
light	$k_f\text{ECL} \cdot \text{Ru2e}$	ECL emission
E	$\text{SC2}(t) \cdot \text{EF}(z)$	Applied potential
kda	$1e4 \cdot (\text{EF}(z) > 1.9)$	Forward rate constant for degradation of NADH at low pH

3) Geometry

- Boundary mode

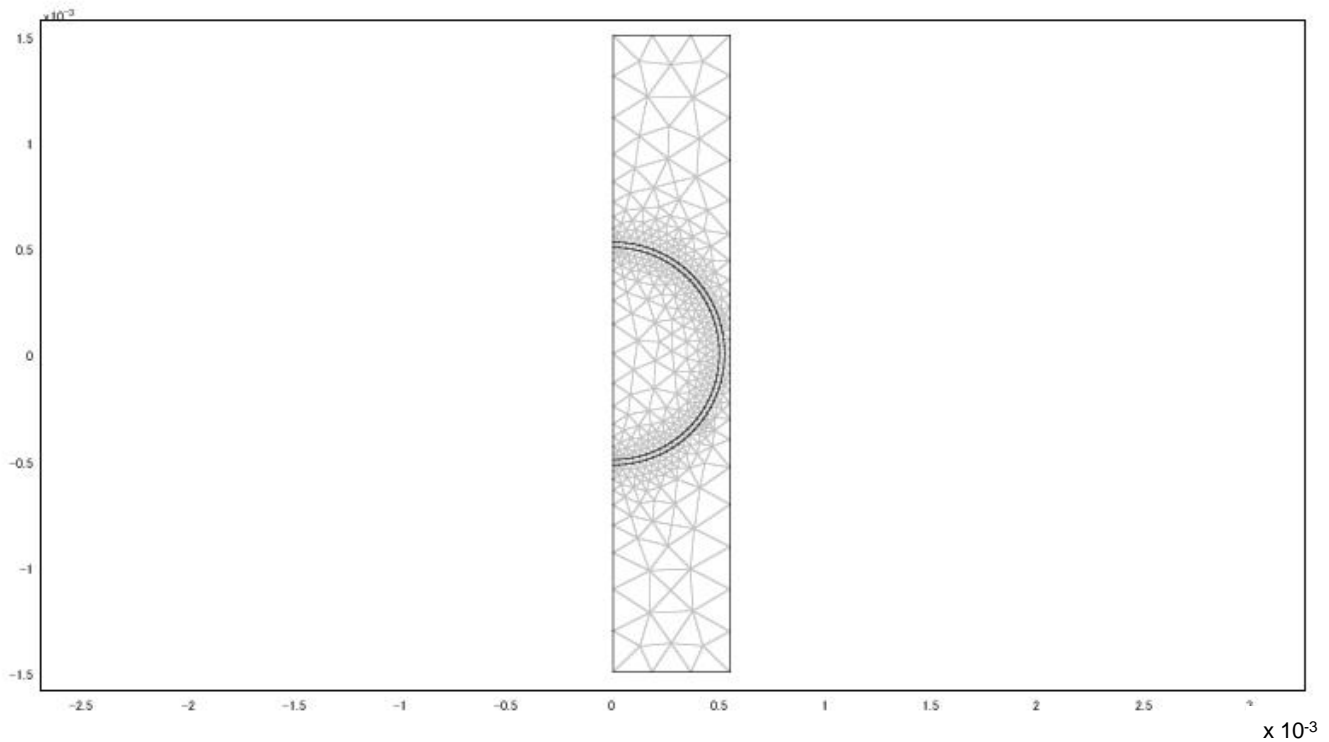


- Subdomain mode



4) Mesh statistics

Number of degrees of freedom	29024
Number of mesh points	471
Number of elements	873
Triangular	873
Quadrilateral	0
Number of boundary elements	164
Number of vertex elements	10
Minimum element quality	0.726
Element area ratio	0.009



5) Application mode properties

Application mode type: Convection and Diffusion (Chemical Engineering Module)

Application mode name: chcd

Property	Value
Default element type	Lagrange - Quadratic
Analysis type	Transient

Equation form	Non-conservative
Equilibrium assumption	Off
Frame	Frame (ref)
Weak constraints	Off
Constraint type	Ideal

6) Variables

Dependent variables: H2PO4, HPO4, H, NADH, e, rcNADH, rNAD, cNAD, Ru2, Ru3, Ru2e, ECL, H2O, O2, P1, P2

Shape functions: shlag(2,'H2PO4'), shlag(2,'HPO4'), shlag(2,'H'), shlag(2,'NADH'), shlag(2,'e'), shlag(2,'rcNADH'), shlag(2,'rNAD'), shlag(2,'cNAD'), shlag(2,'Ru2'), shlag(2,'Ru3'), shlag(2,'Ru2e'), shlag(2,'ECL'), shlag(2,'H2O'), shlag(2,'O2'), shlag(2,'P1'), shlag(2,'P2')

Interior boundaries active

7) Boundary settings

Boundary	1, 3-6	2, 7-8	9, 12
Type	Axial symmetry	Insulation/Symmetry	Continuity
name	axial	Cell	active
Inward flux (N)	{0;0;0;0;0;0;0;0;0;0;0;0;0}	{0;0;0;0;0;0;0;0;0;0;0;0;0;0;0;0}	{0;0;0;0;0;0;0;0;0;0;0;0;0;0;0;0;0;0;0}

Boundary	10	11
Type	Continuity	Continuity
name	beadsurface2	beadsurface
Inward flux (N)	{0;0;kfH2O*H2O*2;-kfNADH*NADH;0;kfNADH*NADH;0;0;-kfRu2*Ru2+kbRu2*Ru3;kfRu2*Ru2-kbRu2*Ru3;0;0;-kfH2O*H2O;kfH2O*H2O*0.5;0;0}	{0;0;kfH2O*H2O*2;-kfNADH*NADH;0;kfNADH*NADH;0;0;-kfRu2*Ru2+kbRu2*Ru3;kfRu2*Ru2-kbRu2*Ru3;0;0;-kfH2O*H2O;kfH2O*H2O*0.5;0;0}

8) Subdomain settings

Subdomain	1
name	solution
Diffusion coefficient (D)	{ D;D;DH;D;D;D;D;D;D;D;D;D;D;D;D }
Reaction rate (R)	{ -kfb*H2PO4+kbb*HPO4*H;kfb*H2PO4-kbb*HPO4*H;kfb*H2PO4-kbb*HPO4*H+kfrNADH*rcNADH-kbrNADH*rNAD*H;-kda*NADH;0;-kfrNADH*rcNADH+kbrNADH*rNAD*H;kfrNADH*rcNADH-kbrNADH*rNAD*H;0;0;0;0;0;0;0;0;0 }
Subdomain	2
name	active
Diffusion coefficient (D)	{ D;D;DH;D;D;D;D;D;D;D;D;D;D;D;D }
Reaction rate (R)	{ -kfb*H2PO4+kbb*HPO4*H;kfb*H2PO4-kbb*HPO4*H;kfb*H2PO4-kbb*HPO4*H+kfrNADH*rcNADH-kbrNADH*rNAD*H;-kda*NADH;0;-kfrNADH*rcNADH+kbrNADH*rNAD*H;kfrNADH*rcNADH-kbrNADH*rNAD*H-kf3*Ru3*rNAD;kf3*Ru3*rNAD;0;-kf3*Ru3*rNAD;kf3*Ru3*rNAD-kfECL*Ru2e;kfECL*Ru2e;0;0;0;0 }
Subdomain	3
name	bead
Diffusion coefficient (D)	{ 0;0;0;0;0;0;0;0;0;0;0;0;0;0;0 }
Reaction rate (R)	{ 0;0;0;0;0;0;0;0;0;0;0;0;0;0;0 }

Subdomain initial value		1	2	3
Concentration, H2PO4 (H2PO4)	mol/m ³	cH2PO4	cH2PO4	0
Concentration, HPO4 (HPO4)	mol/m ³	cHPO4	cHPO4	0
Concentration, NADH (NADH)	mol/m ³	cNADH	cNADH	0
Concentration, Ru2 (Ru2)	mol/m ³	cRu	cRu	0
Concentration, H2O (H2O)	mol/m ³	cH2O	cH2O	0

9) Functions

Function	Expression	Derivatives	Complex output
EF(a)	a*3000+0.5	d(a*3000+0.5,a)	false
SC2(b)	b*(b<1)+1*(b>=1)	d(b*(b<1)+1*(b>=1),b)	false

10) Solver settings

- General

Analysis type	Transient
Auto select solver	On
Solver	Time dependent
Solution form	Automatic
Symmetric	auto
Adaptive mesh refinement	Off
Optimization/Sensitivity	Off
Plot while solving	Off

- Direct (UMFPACK)

Solver type: Linear system solver

Parameter	Value
Pivot threshold	0.1
Memory allocation factor	0.7

- Time stepping

Parameter	Value
Times	range(0,0.01,4)
Relative tolerance	0.0000001
Absolute tolerance	0.0000001
Times to store in output	Specified times
Time steps taken by solver	Free
Maximum BDF order	5
Singular mass matrix	Maybe
Consistent initialization of DAE systems	Backward Euler
Error estimation strategy	Include algebraic
Allow complex numbers	On

8.5. Part C (Spatially-resolved bipolar ECL, 2D)

The 1D modeling for spatially-resolved bipolar ECL was carried out using the model for Ir(ppy)₃ (Part A) and parameters that are same for the 2D modeling. Only the model and parameters for the 2D modeling are shown this section.

1) Constants

Name	Value	Description
alpha	0.5	Transfer coefficient
F	96485	Faraday constant
R	8.314	Gas constant
T	298.15	Room temperature
n	1	Electron number
fa	38.94	F/RT
k0TPA	1e-3	Standard rate constant for TPA oxidation
E0TPA	1.1	Formal potential for TPA oxidation
kfrTPA	3500	Forward rate constant for deprotonation of TPA radical cation
kfI1	100000	Forward rate constant for P1 generation
kfI2	10 ⁹	Forward rate constant for excited Ir quench
kfIECL	1e5	Forward rate constant for ECL generation
k0Ir0	1e-3	Standard rate constant for Ir oxidation
E0Ir0	0.9	Formal potential for Ir oxidation
cH	0	Hydrogen concentration
D	5e-10	General diffusion coefficient
DH	5e-9	Diffusion coefficient for H ⁺
k0d	1e-3	Standard rate constant for TPA radical oxidation
E0d	-2.1	Formal potential for TPA radical oxidation
cIr0	0.5	Ir concentration
cTPA	10	TPA concentration
k0Ru2	1e-4	Standard rate constant for second luminophore oxidation
E0Ru2	0.85	Formal potential for second luminophore oxidation
kfR1	1e7	Forward rate constant for P1 generation for second luminophore
kfRECL	10 ⁵	Forward rate constant for ECL generation for second luminophore
cRu0	0.05	Second luminophore concentraion

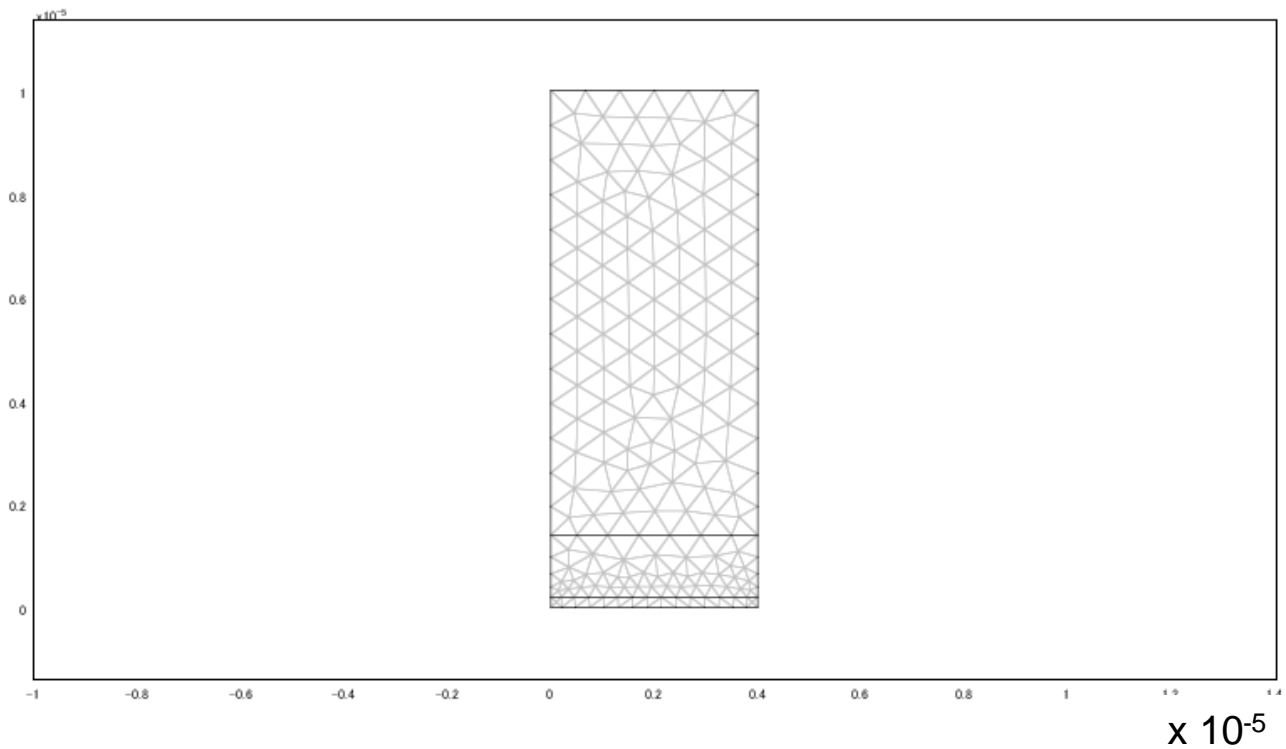
2) Global expressions

Name	Expression	Description
kfTPA	$k0TPA * \exp((1-\alpha) * n * fa * (E-E0TPA))$	forward rate constant for TPA oxidation
kbTPA	$k0TPA * \exp((-1 * \alpha) * n * fa * (E-E0TPA))$	backward rate constant for TPA oxidation
kfIr0	$k0Ir0 * \exp((1-\alpha) * n * fa * (E-E0Ir0))$	forward rate constant for Ir0 oxidation
kbIr0	$k0Ir0 * \exp((-1 * \alpha) * n * fa * (E-E0Ir0))$	backward rate constant for Ir0 oxidation
E	$0.5 * t * x / (4 * 10^{-6}) * SC(t)$	applied voltage - scan
kfd	$k0d * \exp((1-\alpha) * n * fa * (E-E0d))$	forward rate constant for rTPA deprotonation
kbd	$k0d * \exp((-1 * \alpha) * n * fa * (E-E0d))$	backward rate constant for rTPA deprotonation
cd	$(ndflux_e_chdi + ndflux_P1_chdi) * F * -1$	current density
light	$kfIECL * Ire + kfRECL * Ru2e * 5$	ECL emission
kfRu2	$k0Ru2 * \exp((1-\alpha) * n * fa * (E-E0Ru2))$	forward rate constant for second luminophore oxidation
kbRu2	$k0Ru2 * \exp((-1 * \alpha) * n * fa * (E-E0Ru2))$	backward rate constant for second luminophore oxidation
light2	$kfRECL * Ru2e$	ECL emission for second luminophore
light1	$kfIECL * Ire$	ECL emission for Ir0

3) Geometry

- Boundary mode

Number of degrees of freedom	13968
Number of mesh points	209
Number of elements	359
Triangular	359
Quadrilateral	0
Number of boundary elements	79
Number of vertex elements	8
Minimum element quality	0.818
Element area ratio	0.046



5) Application mode properties

Application mode type: Convection and Diffusion (Chemical Engineering Module)

Application mode name: chcd

Property	Value
Default element type	Lagrange - Quadratic
Analysis type	Transient
Equation form	Non-conservative
Equilibrium assumption	Off

Frame	Frame (ref)
Weak constraints	Off
Constraint type	Ideal

6) Variables

Dependent variables: TPA, rcTPA, rTPA, e, H, Ir0, Ir1, Ire, Ru1, Ru2, Ru3, Ru2e, IECL, RECL, P1, P2, P3, P4

Shape functions: shlag(2,'TPA'), shlag(2,'rcTPA'), shlag(2,'rTPA'), shlag(2,'e'), shlag(2,'H'), shlag(2,'Ir0'), shlag(2,'Ir1'), shlag(2,'Ire'), shlag(2,'Ru1'), shlag(2,'Ru2'), shlag(2,'Ru3'), shlag(2,'Ru2e'), shlag(2,'IECL'), shlag(2,'RECL'), shlag(2,'P1'), shlag(2,'P2'), shlag(2,'P3'), shlag(2,'P4')

Interior boundaries inactive

7) Boundary settings

Boundary	1, 3, 5, 7-10	2, 7-8
Type	Insulation/Axial symmetry	Flux
name	Cell	Electrode
Inward flux (N)	{0;0;0;0;0;0;0;0;0;0;0;0;0;0;0}	{-kfTPA*TPA;kfTPA*TPA;-kfd*rTPA;0;0;-kfIr0*Ir0+kbIr0*Ir1;kfIr0*Ir0-kbIr0*Ir1;0;0;-kfRu2*Ru2+kbRu2*Ru3;kfRu2*Ru2-kbRu2*Ru3;0;0;0;0;0;0}

8) Subdomain settings

Subdomain	1-3
name	EC
Diffusion coefficient (D)	{D;D;D;D;DH;D;D;D;D;D;D;D;D;D;D}
Reaction rate (R)	{0;-kfrTPA*rcTPA-kfI2*Ire*rcTPA;kfrTPA*rcTPA-kfI1*Ir1*rTPA-kfR3*Ru3*rTPA;0;0;kfIECL*Ire;-kfI1*Ir1*rTPA+kfI2*Ire*rcTPA;kfI1*Ir1*rTPA-kfIECL*Ire-kfI2*Ire*rcTPA;0;kfRECL

*Ru2e;-kfR3*Ru3*rTPA;kfR3*Ru3*rTPA-kfRECL*Ru2e;kfIE CL*Ire;kfRECL*Ru2e;0;0;0}
--

Subdomain initial value		1-3
Concentration, TPA (TPA)	mol/m ³	cTPA
Concentration, Ir0 (Ir0)	mol/m ³	cIr0
Concentration, Ru2 (Ru2)	mol/m ³	cRu0

9) Functions

Function: SC

Data source type: table

x	f(x)
0	0
0.01	0.01
10	10

10) Solver settings

- General

Analysis type	Transient
Auto select solver	On
Solver	Time dependent
Solution form	Automatic
Symmetric	auto
Adaptive mesh refinement	Off
Optimization/Sensitivity	Off
Plot while solving	Off

- Direct (UMFPACK)

Solver type: Linear system solver

Parameter	Value
Pivot threshold	0.1
Memory allocation factor	0.7

- Time stepping

Parameter	Value
Times	range(0,0.01,5)
Relative tolerance	0.0000001
Absolute tolerance	0.0000001
Times to store in output	Specified times
Time steps taken by solver	Free
Maximum BDF order	5
Singular mass matrix	Maybe
Consistent initialization of DAE systems	Backward Euler
Error estimation strategy	Include algebraic
Allow complex numbers	On

9. References

- [1] A. J. Bard, Ed., *Electrogenerated Chemiluminescence*. Marcel Dekker: New York, 2004.
- [2] D. M. Hercules, "Chemiluminescence Resulting from Electrochemically Generated Species.," *Science*, vol. 145, pp. 808–809, 1964.
- [3] R. Visco and E. Chandross, "Electroluminescence in Solutions of Aromatic Hydrocarbons," *J. Am. Chem. Soc.*, vol. 87, no. 11, pp. 139–40, 1964.
- [4] K. Santhanam and A. Bard, "Chemiluminescence of Electrogenerated 9,10-Diphenylanthracene Anion Radical," *J. Am. Chem. Soc.*, vol. 2243, pp. 139–140, 1965.
- [5] L. R. Faulkner and A. J. Bard, "Electrogenerated chemiluminescence. IV. Magnetic field effects on the electrogenerated chemiluminescence of some anthracenes," *J. Am. Chem. Soc.*, vol. 91, no. 2, pp. 209–210, 1969.
- [6] R. A. Marcus, "On the Theory of Chemiluminescent Electron-Transfer Reactions," *J. Chem. Phys.*, vol. 43, no. 8, pp. 2654–2657, 1965.
- [7] S. W. Feldberg, "A Possible Method for Distinguishing between Triplet-Triplet Annihilation and Direct Singlet Formation in Electrogenerated Chemiluminescence," *J. Phys. Chem.*, vol. 70, no. 12, pp. 3928–3930, 1966.
- [8] S. W. Feldberg, "Theory of Controlled Potential Electrogeneration of Chemiluminescence¹," *J. Am. Chem. Soc.*, vol. 88, no. 3, pp. 390–393, Feb. 1966.
- [9] J. T. Maloy, K. B. Prater, and A. J. Bard, "Electrogenerated Chemiluminescence. V. The Rotating-Ring-Disk Electrode. Digital Simulation and Experimental Evaluation," *J. Am. Chem. Soc.*, vol. 93, no. 23, pp. 5959–5968, 1971.
- [10] J. T. Maloy and A. J. Bard, "Electrogenerated Chemiluminescence. VI. Studies of The Efficiency and Mechanisms of 9,10-Diphenylanthracene, Rubrene, and Pyrene Systems at a Rotating-Ring-Disk Electrode," *J. Am. Chem. Soc.*, vol. 93, no. 23, pp. 5968–5981, Nov. 1971.
- [11] N. E. Tokel and A. J. Bard, "Electrogenerated Chemiluminescence. IX. Electrochemistry and Emission from Systems Containing

- Tris(2,2'-bipyridine)ruthenium(II) Dichloride," *J. Am. Chem. Soc.*, vol. 94, no. 8, pp. 2862–2863, 1972.
- [12] M. Chang, T. Saji, and A. J. Bard, "Electrogenerated Chemiluminescence. 30. Electrochemical Oxidation of Oxalate Ion in the Presence of Luminescers in Acetonitrile Solutions," *J. Am. Chem. Soc.*, vol. 99, no. 16, pp. 5399–5403, 1977.
- [13] J. B. Noffsinger and N. D. Danielson, "Generation of Chemiluminescence upon Reaction of Aliphatic Amines with Tris(2,2'-Bipyridine)Ruthenium(III)," *Anal. Chem.*, vol. 59, pp. 865–868, 1987.
- [14] J. Butler and A. Henglein, "Elementary Reactions of The Reduction of Tl^+ in Aqueous Solution," *Radiat.Phys.Chem.*, vol. 15, pp. 603–612, 1980.
- [15] J. K. Leland and M. Powell, "Electrogenerated Chemiluminescence: An Oxidative-Reduction Type ECL Reaction Sequence Using Tripropyl Amine," *J. Electrochem. Soc.*, vol. 137, no. 10, pp. 3127–3131, 1990.
- [16] F. Kanoufi, Y. Zu, and A. J. Bard, "Homogeneous Oxidation of Trialkylamines by Metal Complexes and its Impact on Electrogenerated Chemiluminescence in the Trialkylamine / $Ru(bpy)_3^{2+}$ System," *J. Phys. Chem. B*, vol. 105, pp. 210–216, 2001.
- [17] Y. Zu and A. J. Bard, "Role of Direct Coreactant Oxidation in the Ruthenium Tris(2,2')bipyridyl / Tripropylamine System and the Effect of Halide Ions on the Emission Intensity," *Anal. Chem.*, vol. 72, no. 14, pp. 3223–3232, 2000.
- [18] D. Bruce, J. McCall, and M. M. Richter, "Effects of Electron Withdrawing and Donating Groups on the Efficiency of Tris(2,2'-bipyridyl)ruthenium(II)/Tri-n-propylamine Electrochemiluminescence.," *Analyst*, vol. 127, no. 1, pp. 125–128, 2002.
- [19] B. Factor, B. Muegge, S. Workman, E. Bolton, J. Bos, and M. M. Richter, "Surfactant Chain Length Effects on the Light Emission of Tris(2,2'-bipyridyl)ruthenium(II)/Tripropylamine Electrogenerated Chemiluminescence," *Anal. Chem.*, vol. 73, no. 19, pp. 4621–4624, 2001.
- [20] S. Workman and M. M. Richter, "The Effects of Nonionic Surfactants on the Tris (2,2'-bipyridyl) ruthenium (II) -Tripropylamine Electrochemiluminescence System," *Anal. Chem.*, vol. 72, no. 22, pp. 5556–5561, 2000.

- [21] M. Richter, "Electrochemiluminescence (ECL)," *Chem. Rev.*, vol. 108, pp. 2506–2553, 2004.
- [22] T. E. Forster, R. J., Bertocello, P., & Keyes, "Electrogenerated Chemiluminescence," *Annu. Rev. Anal. Chem.*, vol. 2, no. 1970, pp. 359–385, Jul. 2009.
- [23] Z. Liu *et al.*, "Recent Advances in Electrochemiluminescence," *Chem. Soc. Rev.*, vol. 44, no. 10, pp. 3117–3142, 2015.
- [24] R. M. Wightman, S. P. Forry, R. Maus, D. Badocco, and P. Pastore, "Rate-Determining Step in the Electrogenerated Chemiluminescence from Tertiary Amines with Tris(2,2'-bipyridyl)ruthenium(II)," *J. Phys. Chem. B*, vol. 108, no. 51, pp. 19119–19125, 2004.
- [25] R. Y. Lai and A. J. Bard, "Electrogenerated Chemiluminescence 71. Photophysical, Electrochemical, and Electrogenerated Chemiluminescent Properties of Selected Dipyrromethene-BF₂ Dyes," *J. Phys. Chem. B*, vol. 107, pp. 5036–5042, 2003.
- [26] Z. Chen and Y. Zu, "Electrogenerated Chemiluminescence of the Tris(2,2'-bipyridine)ruthenium (II) / Tertiary Amine Systems : Effects of Electrode Surface Hydrophobicity on the Low-Oxidation-Potential Emission," *J. Phys. Chem. B*, no. 11, pp. 21877–21882, 2009.
- [27] Y. Zu and F. Li, "Characterization of the Low-Oxidation Potential Electrogenerated Chemiluminescence of Tris(2,2'-bipyridine)ruthenium(II) with Tri-n-propylamine as Coreactant," *Anal. Chim. Acta*, vol. 550, pp. 47–52, 2005.
- [28] H. Zheng and Y. Zu, "Emission of Tris(2,2'-bipyridine)ruthenium(II) by Coreactant Electrogenerated Chemiluminescence: From O₂-Insensitive to Highly O₂-Sensitive," *J. Phys. Chem. B*, vol. 109, pp. 12049–12053, 2005.
- [29] X.-B. Yin, B.-B. Sha, X.-H. Zhang, X.-W. He, and H. Xie, "The Factors Affecting the Electrochemiluminescence of Tris(2,2'-bipyridyl)ruthenium(II)/Tertiary Amines," *Electroanalysis*, vol. 20, no. 10, pp. 1085–1091, 2008.
- [30] P. Pastore, F. Magno, M. Collinson, and R. M. Wightman, "Simulation of Electrochemiluminescence Produced by a High-Frequency Square-Wave Potential Waveform. Effects of Ohmic Drop and Cell Time Constant on Electrode Potential, Current and Light Emission," *J. Electroanal. Chem.*, vol. 397, pp. 19–26, 1995.

- [31] F. Li and Y. Zu, "Effect of Nonionic Fluorosurfactant on the Electrogenerated Chemiluminescence of the Tris(2,2'-bipyridine)ruthenium(II)/Tri-n-propylamine System: Lower Oxidation Potential and Higher Emission Intensity," *Anal. Chem.*, vol. 76, no. 6, pp. 1768–1772, 2004.
- [32] W. Miao, J.-P. Choi, and A. J. Bard, "Electrogenerated Chemiluminescence 69: The Tris(2,2'-bipyridine)ruthenium(II), (Ru(bpy)₃²⁺)/Tri-n-propylamine (TPrA) System Revisited - A New Route Involving TPrA^{•+} Cation Radicals," *J. Am. Chem. Soc.*, vol. 124, no. 48, pp. 14478–14485, 2002.
- [33] P. McCord and A. J. Bard, "Electrogenerated Chemiluminescence: Part 54. Electrogenerated Chemiluminescence of Ruthenium (II) 4,4'-diphenyl-2,2'-bipyridine and Ruthenium (II) 4,7-diphenyl-1, 10-phenanthroline Systems in Aqueous and Acetonitrile Solutions," *J. Electroanal. Chem. Interfacial Electrochem.*, vol. 318, no. 1, pp. 91–99, 1991.
- [34] R. Lai, M. Chiba, N. Kitamura, and A. Bard, "Electrogenerated Chemiluminescence. 68. Detection of Sodium Ion with a Ruthenium(II) Complex with Crown Ether Moiety at the 3, 3'-positions on the 2, 2'-bipyridine," *Anal. Chem.*, vol. 74, pp. 551–553, 2002.
- [35] B. D. Muegge and M. M. Richter, "Electrochemiluminescent Detection of Metal Cations Using a Ruthenium(II) Bipyridyl Complex Containing a Crown Ether Moiety," *Anal. Chem.*, vol. 74, no. 3, pp. 547–550, 2002.
- [36] F. Kanoufi and A. Bard, "Electrogenerated Chemiluminescence. 65. An Investigation of the Oxidation of Oxalate by Tris(polypyridine)ruthenium Complexes and the Effect of the Electrochemical Steps on the Emission Intensity," *J. Phys. Chem. B*, vol. 103, no. 47, pp. 10469–10480, 1999.
- [37] W. Leng, Y. Zhou, Q. Xu, and J. Liu, "Synthesis and Characterization of Nonlinear Optical Side-Chain Polyimides Containing the Benzothiazole Chromophores," *Macromolecules*, vol. 34, pp. 244–252, 2001.
- [38] X. Zhang and A. J. Bard, "Electrogenerated Chemiluminescent Emission from an Organized (L-B) Monolayer of a Tris(2,2'-bipyridine)ruthenium(2+)-Based Surfactant on Semiconductor and Metal Electrodes," *J. Phys. Chem.*, vol. 92, no. 20, pp. 5566–5569, 1988.

- [39] M. M. Richter, A. J. Bard, W. Kim, and R. H. Schmehl, "Electrogenerated Chemiluminescence. 62. Enhanced ECL in Bimetallic Assemblies with Ligands That Bridge Isolated Chromophores," *Anal. Chem.*, vol. 70, no. 2, pp. 310–318, 1998.
- [40] D. Bruce and M. M. Richter, "Green electrochemiluminescence from ortho-metalated tris(2-phenylpyridine)iridium(III)," *Anal. Chem.*, vol. 74, no. 6, pp. 1340–1342, 2002.
- [41] A. Kapturkiewicz and G. Angulo, "Extremely Efficient Electrochemiluminescence Systems Based on Tris(2-phenylpyridine)iridium(III)," *Dalt. Trans.*, pp. 3907–3913, 2003.
- [42] J. Il Kim, I. Shin, H. Kim, and J. Lee, "Efficient Electrogenerated Chemiluminescence from Cyclometalated Iridium(III) Complexes," *J. Am. Chem. Soc.*, vol. 127, no. 6, pp. 1614–1615, 2005.
- [43] L. Flamigni, A. Barbieri, C. Sabatini, B. Ventura, and F. Barigelletti, "Photochemistry and Photophysics of Coordination Compounds: Iridium Photochemistry and Photophysics of Coordination Compounds II," *Photochem. Photophysics Coord. Compd. I*, vol. 281, pp. 143–203, 2007.
- [44] S. Zanarini, M. Felici, and G. Valenti, "Green and Blue Electrochemically Generated Chemiluminescence from Click Chemistry—Customizable Iridium Complexes," *A Eur. J.*, vol. 17, no. 16, pp. 4640–4647, 2011.
- [45] C. Li, J. Lin, X. Yang, and J. Wan, "Efficient Electrochemiluminescent Cyclometalated Iridium(III) Complexes: Synthesis, Photophysical and Electrochemiluminescent Properties," *J. Organomet. Chem.*, vol. 696, no. 11–12, pp. 2445–2450, 2011.
- [46] K. N. Swanick, S. Ladouceur, E. Zysman-Colman, and Z. Ding, "Bright Electrochemiluminescence of Iridium(III) Complexes," *Chem. Commun.*, vol. 48, no. 26, pp. 3179–3181, 2012.
- [47] T.-H. Kwon, Y. H. Oh, I.-S. Shin, and J.-I. Hong, "New Approach Toward Fast Response Light-Emitting Electrochemical Cells Based on Neutral Iridium Complexes via Cation Transport," *Adv. Funct. Mater.*, vol. 19, no. 5, pp. 711–717, 2009.

- [48] S. Zandarini *et al.*, “Iridium Doped Silica-PEG Nanoparticles: Enabling Electrochemiluminescence of Neutral Complexes in Aqueous Media,” *J. Am. Chem. Soc.*, vol. 131, no. 40, pp. 14208–14209, 2009.
- [49] C. X. Li, J. A. Lin, Y. S. Guo, and S. S. Zhang, “A Novel Electrochemiluminescent Reagent of Cyclometalated Iridium Complex-Based DNA Biosensor and Its Application in Cancer Cell Detection,” *Chem. Commun.*, vol. 47, no. 15, pp. 4442–4444, 2011.
- [50] M.-J. Li, P. Jiao, M. Lin, W. He, G.-N. Chen, and X. Chen, “High Electrochemiluminescence of a New Water-Soluble Iridium(III) Complex for Determination of Antibiotics,” *Analyst*, vol. 136, pp. 205–210, 2011.
- [51] I. S. Shin, S. Yoon, J. Il Kim, J. K. Lee, T. H. Kim, and H. Kim, “Efficient Green-colored Electrochemiluminescence from Cyclometalated Iridium(III) Complex,” *Electrochim. Acta*, vol. 56, no. 17, pp. 6219–6223, 2011.
- [52] K. N. Swanick, S. Ladouceur, E. Zysman-colman, and Z. Ding, “Self-Enhanced Electrochemiluminescence of an Iridium (III) Complex : Mechanistic Insight,” *Angew. Chemie*, vol. 51, no. 44, pp. 11079–11082, 2012.
- [53] D. A. Walsh, T. E. Keyes, C. F. Hogan, and R. J. Forster, “Protonation Effects on Superexchange across Gold/Osmium Bis(bipyridyl) Tetrazine Chloride Monolayer Interfaces,” *J. Phys. Chem. B*, vol. 105, no. 14, pp. 2792–2799, 2001.
- [54] E. H. Doeven, E. M. Zammit, G. J. Barbante, P. S. Francis, N. W. Barnett, and C. F. Hogan, “A Potential-Controlled Switch On/Off Mechanism for Selective Excitation in Mixed Electrochemiluminescent Systems,” *Chem. Sci.*, vol. 4, pp. 977–982, 2013.
- [55] E. Doeven, G. Barbante, E. Kerr, and C. Hogan, “Red–Green–Blue Electrogenated Chemiluminescence Utilizing a Digital Camera as Detector,” *Anal Chem*, vol. 86, no. 5, pp. 2727–2732, 2014.
- [56] D. Bruce and M. M. Richter, “Green Electrochemiluminescence from Ortho-Metalated Tris(2-phenylpyridine)iridium(III),” *Anal. Chem.*, vol. 74, no. 6, pp. 1340–1342, 2002.

- [57] J. Ouyang, T. C. Zietlow, M. D. Hopkins, F.-R. F. Fan, H. B. Gray, and A. J. Bard, "Electrochemistry and Electrogenerated Chemiluminescence of $\text{Mo}_2\text{Cl}_4(\text{PMe}_3)_4$," *J. Phys. Chem.*, vol. 90, no. 16, pp. 3841–3844, 1986.
- [58] S. Bonafede, M. Ciano, F. Bolletta, and V. Balzani, "Electrogenerated Chemiluminescence of an Ortho-Metalated Platinum(II) Complex," *J. Phys. Chem.*, vol. 90, no. 16, pp. 3836–3841, 1986.
- [59] M. M. Richter, J. D. Debad, D. R. Striplin, G. A. Crosby, and A. J. Bard, "Electrogenerated Chemiluminescence. 59. Rhenium Complexes," *Anal. Chem.*, vol. 68, no. 24, pp. 4370–4376, 1996.
- [60] F. Bolletta, M. Ciano, V. Balzani, and N. Serpone, "Polypyridine Transition Metal Complexes as Light Emission Sensitizers in the Electrochemical Reduction of the Persulfate Ion," *Inorganica Chim. Acta*, vol. 62, pp. 207–213, 1982.
- [61] H. S. White and A. J. Bard, "Electrogenerated Chemiluminescence and Chemiluminescence of the $\text{Ru}(\text{bpy})_3^{2+}$ -Peroxydisulfate System in Acetonitrile-Water Solutions," *J. Am. Chem. Soc.*, vol. 104, pp. 6891–6895, 1982.
- [62] E. F. Fabrizio, I. Prieto, and A. J. Bard, "Hydrocarbon Cation Radical Formation by Reduction of Peroxydisulfate," *Journal of the American Chemical Society*, vol. 122, no. 20, pp. 4996–4997, 2000.
- [63] K. Sung Chul, O. Sooil, and K. Kang-Jin, "Enhanced Electrogenerated Chemiluminescence of Tris(2,2'-bipyridyl)ruthenium (II)- $\text{S}_2\text{O}_8^{2-}$ System by Sodium Dodecyl Sulfate," *Bull. Korean Chem. Soc.*, vol. 11, no. 6, pp. 505–508, 1990.
- [64] G. Xu and S. Dong, "Electrochemiluminescence of the $\text{Ru}(\text{bpy})_3^{2+}/\text{S}_2\text{O}_8^{2-}$ System in Purely Aqueous Solution at Carbon Paste Electrode," *Electroanalysis*, vol. 12, no. 8, pp. 583–587, 2000.
- [65] G. Xu and S. Dong, "Electrochemiluminescent Determination of Peroxydisulfate with $\text{Cr}(\text{bpy})_3^{3+}$ in Purely Aqueous Solution," *Anal. Chim. Acta*, vol. 412, no. 1–2, pp. 235–240, 2000.
- [66] M. M. Richter and A. J. Bard, "Electrogenerated Chemiluminescence. 58. Ligand-Sensitized Electrogenerated Chemiluminescence in Europium Labels," *Anal. Chem.*, vol. 68, no. 15, pp. 2641–2650, 1996.

- [67] H. Wang, G. Xu, and S. Dong, "Electrochemiluminescence of Dichlorotris(1,10-phenanthroline)ruthenium(II) with Peroxydisulfate in Purely Aqueous Solution at Carbon Paste Electrode," *Microchem. J.*, vol. 72, pp. 43–48, 2002.
- [68] I. Rubinstein and A. J. Bard, "Electrogenerated Chemiluminescence. 37. Aqueous ECL Systems Based on Tris(2,2'-bipyridine)ruthenium(2+) and Oxalate or Organic Acids," *J. Am. Chem. Soc.*, vol. 103, no. 3, pp. 512–516, 1981.
- [69] X. Liu, L. Shi, W. Niu, H. Li, and G. Xu, "Environmentally Friendly and Highly Sensitive Ruthenium(II) tris(2,2'-bipyridyl) Electrochemiluminescent System Using 2-(dibutylamino)ethanol as Co-Reactant," *Angew. Chemie - Int. Ed.*, vol. 46, no. 3, pp. 421–424, Jan. 2007.
- [70] T. M. Downey and T. A. Nieman, "Chemiluminescence Detection Using Regenerable Tris(2,2'-bipyridyl)ruthenium(II) Immobilized in Nafion," *Anal. Chem.*, vol. 64, pp. 261–268, 1992.
- [71] A. F. Martin and T. A. Nieman, "Glucose Quantitation Using an Immobilized Glucose Dehydrogenase Enzyme Reactor and a Tris(2,2'-bipyridyl)ruthenium(II) Chemiluminescent Sensor," *Anal. Chim. Acta*, vol. 281, no. 3, pp. 475–481, 1993.
- [72] F. Jameison, R. I. Sanchez, L. Dong, J. K. Leland, D. Yost, and M. T. Martin, "Electrochemiluminescence-Based Quantitation of Classical Clinical Chemistry Analytes," *Anal Chem*, vol. 68, no. 8, pp. 1298–1302, 1996.
- [73] M. Milutinovic, S. Sallard, D. Manojlovic, N. Mano, and N. Sojic, "Glucose Sensing by Electrogenerated Chemiluminescence of Glucose-Dehydrogenase Produced NADH on Electrodeposited Redox Hydrogel," *Bioelectrochemistry*, vol. 82, no. 1, pp. 63–68, 2011.
- [74] X. M. Chen, B. Y. Su, X. H. Song, Q. A. Chen, X. Chen, and X. R. Wang, "Recent Advances in Electrochemiluminescent Enzyme Biosensors," *TrAC - Trends in Analytical Chemistry*, vol. 30, no. 5, pp. 665–676, 2011.
- [75] D. Ege, W. Becker, and A. Bard, "Electrogenerated Chemiluminescent Determination of Tris(2,2'-bipyridine)ruthenium Ion ($\text{Ru}(\text{bpy})_3^{2+}$) at Low Levels," *Anal. Chem.*, vol. 56, no. 13, pp. 2413–2417, 1984.
- [76] A. J. Bard and G. M. Whitesides, "US Patent 5,221,605," 1993.

- [77] G. F. Blackburn *et al.*, “Electrochemiluminescence Detection for Development of Immunoassays and DNA Probe Assays for Clinical Diagnostics,” *Clin. Chem.*, vol. 37, no. 9, pp. 1534–1539, 1991.
- [78] M. C. Kibbey, D. Macallan, and J. W. Karaszkiwicz, “Novel Electrochemiluminescent Assays For Drug Discovery,” *J. Assoc. Lab. Autom.*, vol. 5, pp. 45–48, 2000.
- [79] Y. Hsueh, S. D. Collins, and R. L. Smith, “DNA Quantification with an Electrochemiluminescence Microcell,” *Sensors Actuators, B Chem.*, vol. 49, no. 1–2, pp. 1–4, 1998.
- [80] M. T. Carter and A. J. Bard, “Electrochemical Investigations of the Interaction of Metal Chelates with DNA. 3. Electrogenated Chemiluminescent Investigation of the Interaction of Tris(1,10-phenanthroline)ruthenium(II) with DNA,” *Bioconjugate Chem.*, vol. 1, no. 4, pp. 257–263, 1990.
- [81] M. Rodriguez and A. J. Bard, “Electrochemical Studies of the Interaction of Metal Chelates with DNA. 4. Voltammetric and Electrogenated Chemiluminescent Studies of the Interaction of Tris (2, 2'-bipyridine) Osmium(II) with DNA,” *Anal. Chem.*, vol. 62, no. 24, pp. 2658–2662, 1990.
- [82] J. H. Kenten *et al.*, “Improved Electrochemiluminescent Label for DNA Probe Assays: Rapid Quantitative Assays of HIV-1 Polymerase Chain Reaction Products,” *Clin. Chem.*, vol. 38, no. 6, pp. 873–879, 1992.
- [83] D. R. Deaver, “A New Non-Isotopic Detection System for Immunoassays,” *Nature*, vol. 377, no. 6551, pp. 758–60, 1995.
- [84] J. H. Kenten *et al.*, “Rapid electrochemiluminescence assays of polymerase chain reaction products,” *Clin. Chem.*, vol. 37, no. 9, pp. 1626–1632, 1991.
- [85] M. Shen, J. Rodríguez-López, and J. Huang, “Electrochemistry and Electrogenated Chemiluminescence of Dithienylbenzothiadiazole Derivative. Differential Reactivity of Donor and Acceptor Groups and,” *J. Am. Chem. Soc.*, vol. 132, pp. 13453–12461, 2010.
- [86] G. Valenti, A. Fiorani, and S. Di Motta, “Molecular Size and Electronic Structure Combined Effects on the Electrogenated Chemiluminescence of Sulfurated Pyrene-Cored Dendrimers,” *A Eur. J.*, vol. 21, pp. 2936–2947, 2015.

- [87] O. V. Klymenko, I. Svir, and C. Amatore, "A New Approach for the Simulation of Electrochemiluminescence (ECL)," *ChemPhysChem*, vol. 14, no. 10, pp. 2237–2250, 2013.
- [88] I. Svir, A. Oleinick, O. V. Klymenko, and C. Amatore, "Strong and Unexpected Effects of Diffusion Rates on the Generation of Electrochemiluminescence by Amine/Transition-Metal(II) Systems," *ChemElectroChem*, vol. 2, no. 6, pp. 811–818, 2015.
- [89] M. Sentic, M. Milutinovic, F. Kanoufi, D. Manojlovic, S. Arbault, and N. Sojic, "Mapping Electrogenenerated Chemiluminescence Reactivity in Space: Mechanistic Insight into Model Systems Used in Immunoassays," *Chem. Sci.*, vol. 5, no. 6, pp. 2568–2572, 2014.
- [90] E. J. F. Dickinson, H. Ekström, and E. Fontes, "Electrochemistry Communications Mini Review COMSOL Multiphysics® : Finite Element Software for Electrochemical Analysis . A Mini-review," *Electrochem. commun.*, vol. 40, pp. 71–74, 2014.
- [91] A. Lavacchi, U. Bardi, C. Borri, and S. Caporali, "Cyclic Voltammetry Simulation at Microelectrode Arrays with COMSOL Multiphysics®," *J. Appl. Electrochem.*, vol. 39, no. 11, pp. 2159–2163, 2009.
- [92] G. Valenti, L. Bardini, D. Bonazzi, S. Rapino, M. Marcaccio, and F. Paolucci, "Creation of Reactive Micro Patterns on Silicon by Scanning Electrochemical Microscopy," *J. Phys. Chem. C*, vol. 114, no. 50, pp. 22165–22170, 2010.
- [93] P. Kissinger and W. Heineman, "Cyclic Voltammetry," *J. Chem. Educ.*, vol. 60, no. 9, pp. 702–706, 1983.
- [94] E. H. Doeven, E. M. Zammit, G. J. Barbante, C. F. Hogan, N. W. Barnett, and P. S. Francis, "Selective Excitation of Concomitant Electrochemiluminophores: Tuning Emission Color by Electrode Potential," *Angew. Chemie - Int. Ed.*, vol. 51, no. 18, pp. 4354–4357, 2012.
- [95] G. J. Barbante *et al.*, "Control of Excitation and Quenching in Multi-Colour Electrogenenerated Chemiluminescence Systems through Choice of Co-Reactant," *Chem. - A Eur. J.*, vol. 20, no. 43, pp. 14026–14031, 2014.

- [96] T. Sajoto, P. I. Djurovich, A. B. Tamayo, J. Oxgaard, W. A. Goddard, and M. E. Thompson, "Temperature Dependence of Blue Phosphorescent Cyclometalated Ir(III) Complexes," *J. Am. Chem. Soc.*, vol. 131, no. 28, pp. 9813–9822, 2009.
- [97] K. Imai *et al.*, "Numerical Simulation of Doped Silica Nanoparticle Electrochemiluminescence," *J. Phys. Chem. C*, vol. 119, pp. 26111–26118, 2015.
- [98] X. Zhao, R. Tapeç-Dytioco, and W. Tan, "Ultrasensitive DNA Detection Using Highly Fluorescent Bioconjugated Nanoparticles," *J. Am. Chem. Soc.*, vol. 125, no. 38, pp. 11474–11475, 2003.
- [99] S. Santra, P. Zhang, K. Wang, R. Tapeç, and W. Tan, "Conjugation of Biomolecules with Luminophore-Doped Silica Nanoparticles for Photostable Biomarkers," *Anal. Chem.*, vol. 73, no. 20, pp. 4988–4993, 2001.
- [100] L. Zhang and S. Dong, "Electrogenerated Chemiluminescence Sensors Using Ru(bpy)₃²⁺ Doped in Silica Nanoparticles," *Anal. Chem.*, vol. 78, no. 14, pp. 5119–23, 2006.
- [101] L. Zhang and S. Dong, "Electrogenerated Chemiluminescence Sensing Platform using Ru(bpy)₃²⁺ Doped Silica Nanoparticles and Carbon Nanotubes," *Electrochem. commun.*, vol. 8, no. 10, pp. 1687–1691, 2006.
- [102] L. Qian and X. Yang, "One-step Synthesis of Ru(2,2'-Bipyridine)₃Cl₂-Immobilized Silica Nanoparticles for Use in Electrogenerated Chemiluminescence Detection," *Adv. Funct. Mater.*, vol. 17, no. 8, pp. 1353–1358, 2007.
- [103] S. Guo and E. Wang, "A Novel Sensitive Solid-State Electrochemiluminescence Sensor Material: Doped SiO₂@MWNTs Coaxial Nanocable," *Electrochem. commun.*, vol. 9, pp. 1252–1257, 2007.
- [104] L. Zhang, B. Liu, and S. Dong, "Bifunctional Nanostructure of Magnetic Core Luminescent Shell and Its Application as Solid-State Electrochemiluminescence Sensor Material," *J. Phys. Chem. B*, vol. 111, no. 35, pp. 10448–10452, 2007.
- [105] X. Hun and Z. Zhang, "Electrogenerated Chemiluminescence Sensor for Itopride with Ru(bpy)₃²⁺-Doped Silica Nanoparticles/Chitosan Composite Films Modified Electrode," *Sensors And Actuators B-Chemical*, vol. 131, no. 2, pp. 403–410, 2008.

- [106] S. Zanarini *et al.*, “Ru(bpy) Covalently Doped Silica Nanoparticles as Multicenter Tunable Structures for Electrochemiluminescence Amplification,” *J. Am. Chem. Soc.*, vol. 131, no. 6, pp. 2260–2267, 2009.
- [107] G. Valenti *et al.*, “Transparent Carbon Nanotube Network for Efficient Electrochemiluminescence Devices,” *Chem. - A Eur. J.*, vol. 21, no. 36, pp. 12640–12645, 2015.
- [108] G. Liang, S. Liu, G. Zou, and X. Zhang, “Ultrasensitive Immunoassay Based on Anodic Near-Infrared Electrochemiluminescence from Dual-Stabilizer-Capped CdTe Nanocrystals,” *Anal. Chem.*, vol. 84, no. 24, pp. 10645–10649, 2012.
- [109] Y. Zu and A. J. Bard, “Dependence of Light Emission of the Tris (2,2') bipyridylruthenium(II)/ Tripropylamine System on Electrode Surface Hydrophobicity,” *Society*, vol. 73, no. 16, pp. 3960–3964, 2001.
- [110] L. Wang, L. Zhang, and C. Lu, “Applications in Analytical Chemistry Using the Attractive Properties of Non-Ionic Fluorosurfactants,” *TrAC - Trends in Analytical Chemistry*, vol. 54, pp. 45–55, 2014.
- [111] C. Amatore, Y. Bouret, E. Maisonhaute, J. I. Goldsmith, and H. D. Abruna, “Precise Adjustment of Nanometric-Scale Diffusion Layers within a Redox Dendrimer Molecule by Ultrafast Cyclic Voltammetry: An Electrochemical Nanometric Microtome,” *Chem. Eur. J.*, vol. 7, no. 10, pp. 2206–2226, 2001.
- [112] S. E. Fosdick, K. N. Knust, K. Scida, and R. M. Crooks, “Bipolar Electrochemistry,” *Angew. Chemie - Int. Ed.*, vol. 52, no. 40, pp. 10438–10456, 2013.
- [113] G. Loget, D. Zigah, L. Bouffier, N. Sojic, and A. Kuhn, “Bipolar electrochemistry: from materials science to motion and beyond,” *Acc. Chem. Res.*, vol. 46, no. 11, pp. 2513–2523, 2013.
- [114] A. Arora, J. C. T. Eijkel, W. E. Morf, and A. Manz, “A Wireless Electrochemiluminescence Detector Applied to Direct and Indirect Detection for Electrophoresis on a Microfabricated Glass Device,” *Anal. Chem.*, vol. 73, no. 22, pp. 3282–3288, 2001.
- [115] W. Zhan, J. Alvarez, and R. M. Crooks, “Electrochemical Sensing in Microfluidic Systems Using Electrogenerated Chemiluminescence as a Photonic Reporter of Redox Reactions,” *J. Am. Chem. Soc.*, vol. 124, no. 44, pp. 13265–13270, 2002.

- [116] M. S. Wu, Z. Liu, H. W. Shi, H. Y. Chen, and J. J. Xu, “Visual Electrochemiluminescence Detection of Cancer Biomarkers on a Closed Bipolar Electrode Array Chip,” *Anal. Chem.*, vol. 87, no. 1, pp. 530–537, 2015.
- [117] M.-S. Wu, D.-J. Yuan, J.-J. Xu, and H.-Y. Chen, “Electrochemiluminescence on Bipolar Electrodes for Visual Bioanalysis,” *Chem. Sci.*, vol. 4, no. 3, pp. 1182–1188, 2013.
- [118] M.-S. Wu, B.-Y. Xu, H.-W. Shi, J.-J. Xu, and H.-Y. Chen, “Electrochemiluminescence Analysis of Folate Receptors on Cell Membrane with On-Chip Bipolar Electrode,” *Lab Chip*, vol. 11, no. 16, pp. 2720–4, 2011.
- [119] Q.-M. Feng, J.-B. Pan, H.-R. Zhang, J.-J. Xu, and H.-Y. Chen, “Disposable Paper-Based Bipolar Electrode for Sensitive Electrochemiluminescence Detection of a Cancer Biomarker,” *Chem. Commun. (Camb)*, vol. 50, pp. 2–4, 2014.
- [120] M. Sentic, S. Arbault, L. Bouffier, D. Manojlovic, A. Kuhn, and N. Sojic, “3D electrogenerated chemiluminescence: from surface-confined reactions to bulk emission,” *Chem. Sci.*, vol. 6, no. 8, pp. 4433–4437, 2015.
- [121] M. Sentic, G. Loget, and D. Manojlovic, “Light-Emitting Electrochemical ‘Swimmers,’” *Angew. Chemie*, vol. 51, no. 45, pp. 11284–11288, 2012.
- [122] M. Sentic *et al.*, “Electrochemiluminescent Swimmers for Dynamic Enzymatic Sensing,” *Chem. Commun.*, vol. 50, no. 71, pp. 10202–10205, 2014.
- [123] H. Li, L. Bouf, S. Arbault, A. Kuhn, C. F. Hogan, and N. Sojic, “Spatially-resolved multicolor bipolar electrochemiluminescence,” vol. 77, pp. 10–13, 2017.

10. Acknowledgment

I would like to express my deepest gratitude to everyone who kindly helped me carry out this study as a PhD student. I really appreciate their assistance, suggestions, encouragement, and friendship.

Supervisors:

Prof. Francesco Paolucci

Dr. Giovanni Valenti

Ms. Kyoko Imai

People in Italy:

Prof. Luca Prodi, Prof. Massimo Marcaccio, Dr. Stefania Rapino, Dr. Enrico Rampazzo,

Dr. Andrea Fiorani, and Ms. Elena Villani

People in Japan:

Dr. Takeshi Sakamoto, Mr. Atsushi Takane, Mr. Taku Sakazume, Mr. Shigeki Matsubara,

Mr. Yoshihiro Yamashita, Mr. Yoshinori Negishi, Mr. Shunichiro Nobuki, Ms. Mami

Fukumura, Dr. Hiroya Umeki, and Mr. Akihiro Endo

Family:

Nobuyuki Imai, Yoko Imai, Takao Fujiwara, and Keiko Fujiwara

Shiori Imai, Yuna Imai, and Toya Imai